Mechanical Characterization and Modelling of Hybrid Fibre Architectures of Randomly Oriented Strand Composites

Swaroop Bylahally Visweswaraiah
March 2018

Department of Mechanical Engineering
McGill University, Montreal

A thesis submitted to McGill University
in partial fulfillment of the requirements for the degree of
Doctor of Philosophy

©Copyright
2018, S.B. Visweswaraiah

Never has it been more evident that 'I' stands for 'Insignificant'.

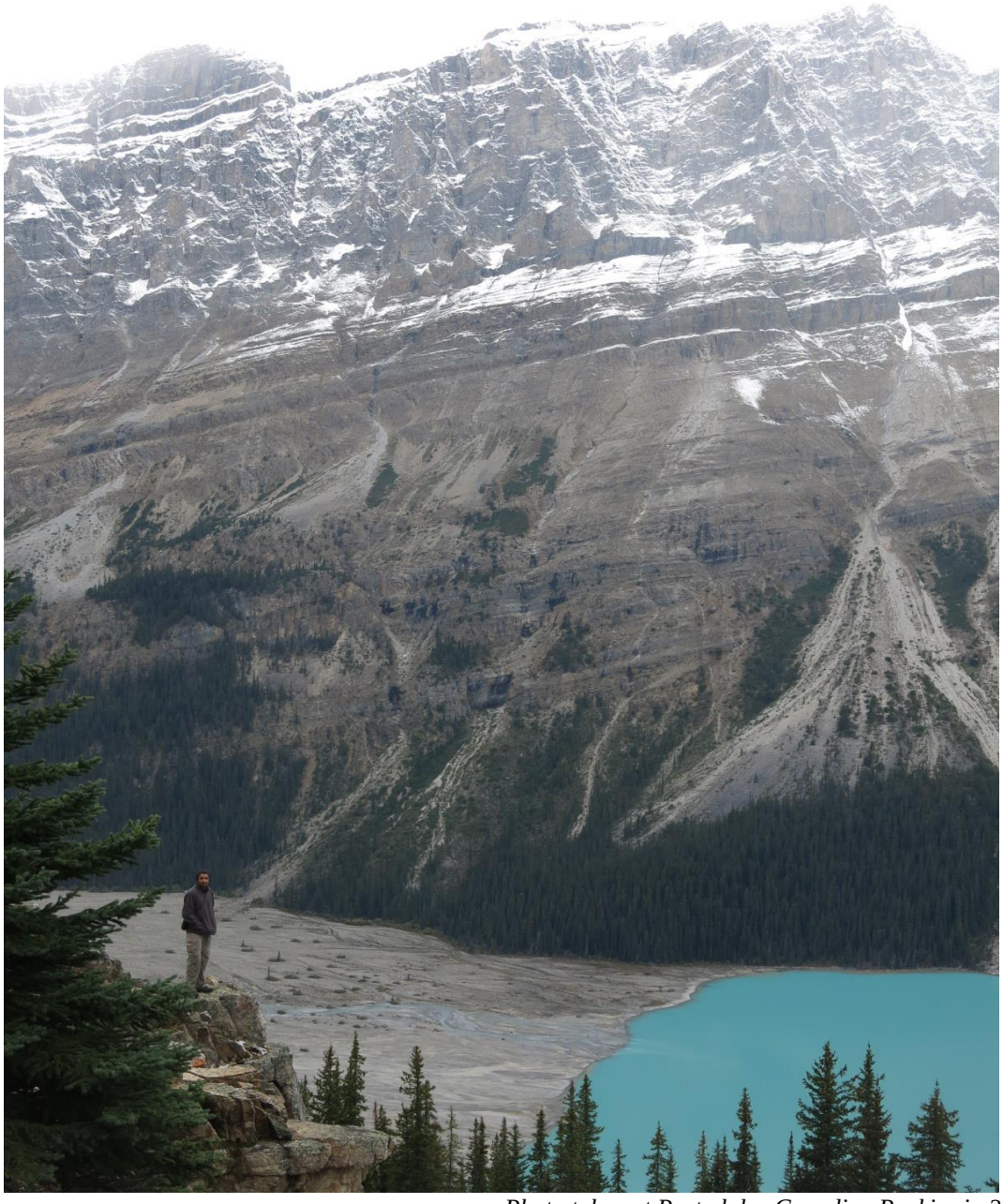

Photo taken at Peyto lake, Canadian Rockies in 2015

Abstract

Continuous fibre (CF) aerospace composites exhibiting excellent mechanical performance possesses low formability characteristics and are confined to simple shell-like geometries with minimal curvatures. On the other hand, long discontinuous fibre composites such as randomly oriented strands (ROS) offer high formability but exhibit low mechanical performance. The overall research objective of this work is to explore trade-off solutions that integrate the formability of carbon/PEEK ROS and the performance of CF carbon/PEEK tapes. Hybrid composites of ROS carbon/PEEK and CF carbon/PEEK architectures are manufactured by the rapid and low-cost compression moulding process.

The mechanical characteristics of the hybrid fibre architectures are investigated at the coupon and part levels. Owing to the low properties of ROS composites under tensile and interlaminar shear loads, the mechanical characterization at the coupon level involves understanding the effects of hybridization of laminate groups with ROS through experiments. Three kinds of laminate groups (cross-ply, quasi-isotropic and angle-ply) that differ in stiffness, strength and strain characteristics from ROS are chosen. Four relative thickness ratios and three stacking configurations of the architectures are chosen for hybridization. The positive and negative synergistic relations because of hybridization are reported and explained. Using flow-control and hybridization strategies at the part level, significant pull-out strength improvements are demonstrated on T-stiffened panels of ROS based composites. This is achieved by addressing two critical manufacturing issues namely the strand waviness and the swirling of strands.

A stochastic finite element model for predicting the tensile behaviour is proposed. The model is characterized by a random strand placement procedure, intralaminar progressive failure analysis using Hashin failure criteria for damage initiation, fracture energy based linear softening law for damage propagation, and the use of traction-separation cohesive element laws to model the interlaminar progressive analysis or interface behaviour. To understand the interlaminar shear behaviour, a semi-empirical model that utilizes a stochastic strand placement procedure and an adaptation of the analytical formulas for the interlaminar shear and bending stress distributions have been proposed to explain the load-sharing induced synergies, on a comparative basis. Both the models explain the mechanical characteristics of hybrid fibre architectures accurately at the coupon level.

Significant improvements in the mechanical characteristics and processing quality of ROS are observed with small proportions of CF laminate groups in the specimen. Through specific-stiffness and specific-strength comparisons, the research demonstrates the structural performance potential of ROS/Continuous fibre hybrids to serve as effective and low-cost replacements for intricate metallic aerospace parts.

Résumé

Les pièces aéronautiques fabriquées de plastique renforcé de fibres continues ont d'excellentes propriétés mécaniques. Par contre, leur mise en forme peut être difficile ce qui restreint leur application à des coques de géométrie simple à faible courbure. En revanche, les renforts de fibres courtes discontinues ou 'Randomly Oriented Strands' (ROS) améliorent la mise en forme au détriment d'une réduction des propriétés mécaniques. Ainsi, l'objectif de cette recherche est d'étudier des solutions pour arriver au meilleur compromis entre la formabilité des ROS carbone/PEEK et la performance mécanique des bandes de carbone/PEEK unidirectionnelles. Les solutions hybrides ROS et fibres continues sont fabriquées par le procédé de moulage par compression qui est à la fois rapide et peu coûteux.

Les propriétés mécaniques des composites hybrides sont étudiées au moyen d'essais sur des échantillons et sur des pièces. Les essais sur échantillons ont été utilisés pour caractériser l'effet de l'hybridation avec des laminés pour améliorer les propriétés en traction et en cisaillement interlaminaire des composites ROS. Trois types de laminés ont été étudiés pour l'hybridation soit les empilements croisés, à angles et quasi-isotropes. Chaque laminé présente des différences uniques comparativement aux ROS tel la rigidité, la résistance et les mécanismes de déformation. Quatre rapports d'épaisseurs relatives et trois configurations d'empilements des différentes architectures ont été considérés pour l'hybridation. La synergie positive et négative résultant de chaque configuration est quantifiée et analysée. Cette thèse présente aussi les résultats des échantillons troués avec entaille hybrides ROS sollicités en traction. Les stratégies de contrôle d'écoulement et d'hybridation à l'échelle d'une plaque avec raidisseur en « T » ont montré une amélioration significative de la résistance à l'arrachement. Ces avantages sont le résultat d'une réduction des phénomènes d'ondulation et d'entortillement des lamelles lors de la mise en forme.

Un modèle stochastique par éléments finis pour prédire le comportement en traction est proposé. Le modèle est caractérisé par le développement d'une procédure d'étalement des lamelles et de paramètres empiriques afin de répliquer le procédé de mise en forme. La défaillance

interlaminaire progressive est prédite par le critère de rupture de Hashin pour l'initiation des dommages. La propagation des dommages est modélisée au moyen de l'énergie de rupture obtenue par une loi linéaire d'adoucissement. Finalement, des lois sont appliquées aux éléments cohésifs pour le détachement induit par traction permettant l'analyse inter laminaire progressive et des comportements des interfaces. Un modèle semi-empirique incluant une distribution stochastique des lamelles et une adaptation des relations analytiques pour la distribution des contraintes de cisaillement interlaminaire et de flexion est proposé pour expliquer la synergie résultante de la répartition des charges dans la structure hybride. Les deux modèles permettent d'expliquer les caractéristiques mécaniques des hybrides ROS et fibres continues à l'échelle des échantillons.

Des améliorations significatives au niveau des propriétés mécaniques et de mise en forme sont obtenues en combinant une faible proportion de fibres continues aux pièces ROS. L'amélioration des performances structurales démontrée par une comparaison de la rigidité-spécifique et de la résistance-spécifique illustre le potentiel des hybrides ROS/CF pour le remplacement de pièces aéronautiques métalliques à géométrie complexe.

Dedicated to the 3 important women in my life:

My mother, my wife, and my sister.

Acknowledgements

I would like to express my sincere thanks to my supervisors Prof. Larry Lessard and Prof. Pascal Hubert, for their invaluable guidance, continued support and encouragement during this research.

Special thanks to the members of the thesis advisory committee (Prof. Damiano Pasini and Prof. Francois Barthelat) and to Prof. Remko Akkerman for accepting to be the External examiner.

I would like to express my very great appreciation to Pierre Beaulieu, Michel Dion, Pierre Doyon, Erin Quinlan and the Materials Laboratory at Bell Helicopter Textron Canada Limited for their technical support and overall guidance. I wish to acknowledge the research funding provided by Bell Helicopter Textron Canada Limited, Industrial Innovation Scholarships (from NSERC and FQRNT) and MITACS accelerate internship program. I am particularly grateful for the legal assistance provided by Arlette Assayag, Agnes Wong, Ester Di Cori and Chérif Aidara.

Thanks to all the students of the Composite Materials and Structures laboratory at McGill University specifically: Marina Selezneva, Rémi Maggio, Nicolas Prégre, Nicolas Ohlmann, Vincent Cadran, John Kyungmin Jung, Yixue Zhang, Nicolas Krumenacker, Valentin Romanov, Adam Smith, Derek Harvey and Lucie Riffard.

I wish to express my endless gratitude to my family. Without any doubt, their relentless support in every step of my life have encouraged me, and I can never be thankful enough.

Finally, I am grateful to all the people who have contributed directly or indirectly to my 'insignificant' learning journey during my graduate studies.

Table of Contents

List of Figures

List of Tables

Chapter 1

Introduction

The choice of the material system (resin system and the fibre architecture), the manufacturing method and the process parameters collaboratively govern the structural characteristics of fibre reinforced composites. Continuous fibre (CF) aerospace preforms usually manufactured as unidirectional (UD) tapes and fabrics (e.g. woven, braided, non-crimp and knitted) [1], offer optimum reinforcement efficiency in the longitudinal direction due to high fibre strength and stiffness but offers high resistance to forming [2, 3]. The poor formability of CF confines their use to simple shell-like geometries requiring high stiffness/strength. The mechanical characteristics of CF preforms have been extensively studied and characterized at both macroscopic and microscopic levels [4].

The load transfer efficiency between a fibre and the surrounding matrix is a function of the interfacial bonding, fibre and matrix mechanical properties and the fibre dimensions. The variation of the strength of composites as a function of fibre length is illustrated in Figure 1-1.a. Fibre preforms are broadly classified into CF and discontinuous fibre architectures based on the critical fibre length (L_c); the fibre length over which ultimate tensile strength (σ_f) can be reached

in the middle of the fibre (Figure 1-1.b). Highest performance of the composite is achieved if the average stress in the fibre computed over its entire length equals the ultimate fibre strength. The critical fibre length is given by the Kelly-Tyson model [5] as shown in Equation 1-1. As noted by Chang et al. [6], maximum fibre efficiency is achieved when fibre length $L_f >> 50\ L_c$. The performance of a composite material increases with fibre length and eventually plateaus reaching the CF properties. If d is the fibre diameter and τ is the matrix shear strength,

$$L_c = \frac{d\ \sigma_f}{2\ \tau} \qquad \text{Equation 1-1}$$

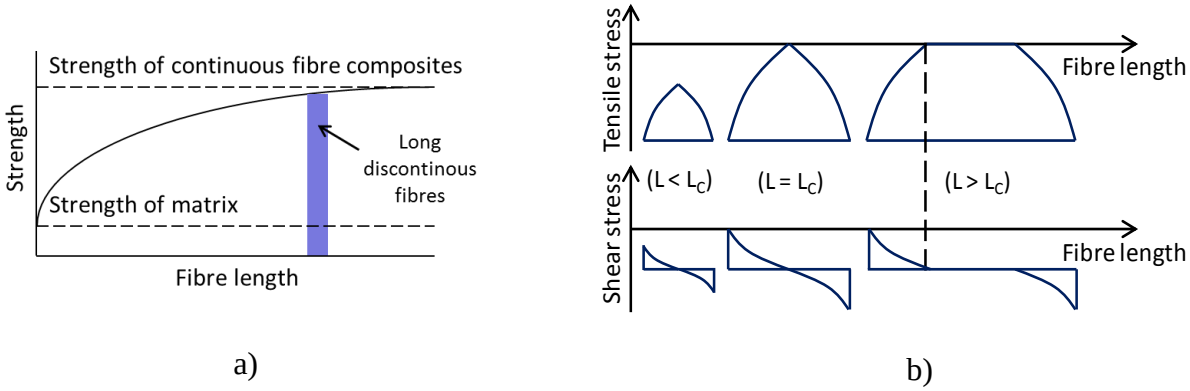

Figure 1-1: Illustration of a) relationship between fibre length and strength of discontinuous fibre composites(adapted from [7]); b) the effect of fibre length on stress distribution in the fibre

Discontinuous fibre architectures can be broadly categorized into long discontinuous fibre architecture (LDF) [6] or high fibre volume fraction systems and short discontinuous fibre architecture or low-fibre volume fraction systems (Figure 1-2), based on the attainable fibre volume fraction (V_f) and the fibre length. Short discontinuous fibre systems could be preferentially aligned or randomly oriented based on the manufacturing process employed. The maximum fibre volume fraction attainable in case of a randomly oriented fibre (ROF) system is

in the order of 37% due to fibre entanglements [8] and the fibre lengths (L_f) are < 50L_c. ROF architecture is widely studied in literature [9].

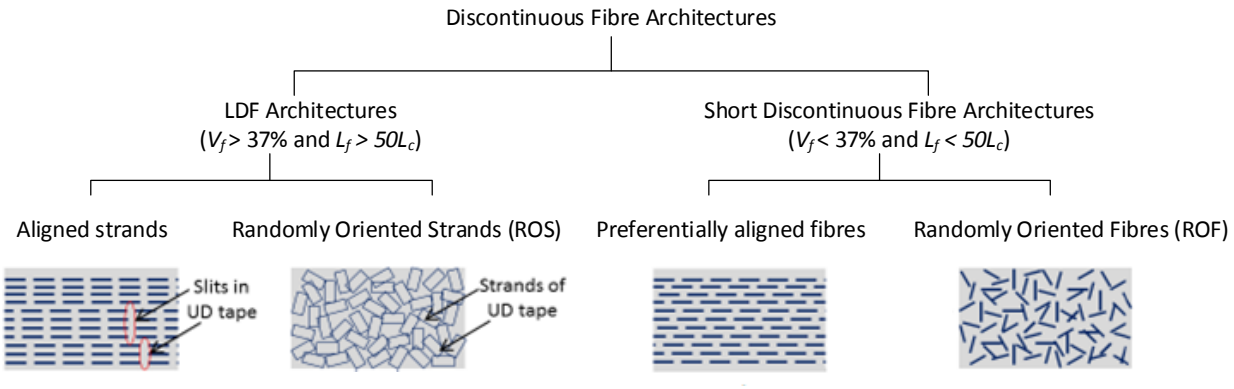

Figure 1-2: Broad classification of discontinuous fibre architectures

A classification representing a trade-off of processability and performance is the LDF architecture [6]. LDF is characterized by the presence of strands or chips representing a parallel system of fibres with fibre lengths > 50L_c and significantly high fibre volume fractions can be attained with LDF composites (up to 60%), due to close packing of fibres within a strand, resulting in adequate mechanical performance. Further, a literature survey showed that preforms with long discontinuous carbon fibres are appealing for structural applications as they bridge the gap between the formability of short fibre composites and performance of continuous fibre composites (Figure 1-3). LDF materials that were developed and studied over the years can be categorized based on fibre orientation (aligned vs. random). Such et al. [10] presented a historical overview of works on aligned discontinuous fibre composites. Randomly oriented strands (ROS) are a class of LDF architecture (Figure 1-2) comprising of prepreg based discontinuous strands of unidirectional tapes or woven fabrics. Researchers use different names for the same material architecture that include discontinuous long fibre (DLF), direct carbon

fibre preforming (DCFP), discontinuous fibre composites (DCF), flake-based composites, ribbon-based composites, platelets and ultra-thin chopped carbon fibre tape-reinforced thermoplastics (UT-CTT). Investigation of mechanical properties of ROS composites (both thermoset and thermoplastic matrices) [11, 12] fabricated from low-flow compression moulding showed that ROS composites exhibit stiffness or modulus comparable to that of quasi-isotropic (QI) laminates, hence are well suited for stiffness-driven designs. Industrial potential of such materials was exemplified by the development of complex net-shape parts (Figure 1-4) that were competitive with metal parts due to their corrosion resistance, light weight and cost-effective manufacturing [6].

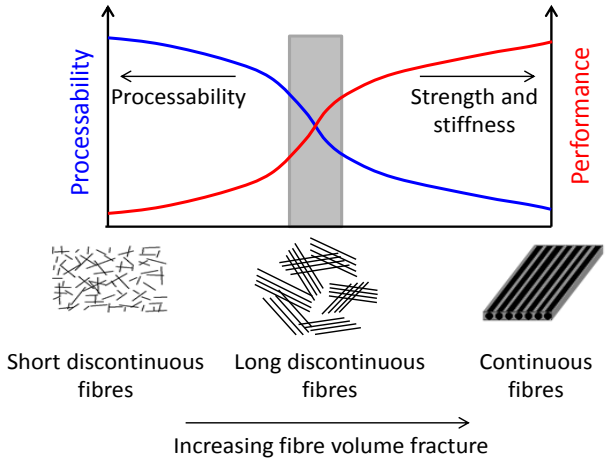

Figure 1-3: Processing and performance of various composite material systems [12, 13]

Despite attractive benefits, ROS composites possess low mechanical strength, demonstrate high variability and notch insensitive behaviour that inhibit their extensive use in load-bearing aerospace parts. Thus, a trade-off solution, as suggested by various authors [14-21], is to use a 'hybrid fibre architecture' that integrates the formability of ROS and performance of continuous fibres. In the literature on hybridization, most researchers typically have considered a high-elongation/low-strength material with low-elongation/high-strength material at the inter-ply and

intra-ply levels to improve the ductility response of the low elongation material [22]. The behaviour of hybrid systems seldom followed simple rule of mixtures (RoM) approach and usually exhibited synergistic relationships called the 'hybrid effect'. Further, this effect is described as either positive or a negative deviation from the theoretical RoM [23]. The review article [22] summarizes the works on hybridization and attributes the synergistic behaviour to the damage development, residual stresses and stress concentrations in hybrids.

a) b) c)

Figure 1-4: Complex net-moulded industrial ROS parts: a) bracket made by Greene, Tweed [24, 25]; b) Bracket made by TenCate [26]; c) Helicopter tailboom frame [27]

The current thesis focuses on 'hybrid fibre architectures' comprising of various fibre preforms/phases such as ROS, unidirectional tapes and woven fabrics with varying proportions and geometric configurations co-existing within a specific region of a component. By controlling the contents, position and arrangement of ROS and CF, both formability and better mechanical performance can be achieved. Benefits of hybridization include: improved and tailored modulus properties, reduction in the variability, and better control on the failure initiation, damage and propagation [13, 28-33]. In addition, hybrid fibre architectures allow for better predictability of failure and strength in notched specimens [30], increase in the interlaminar properties, and reduction in warpage and reduction of swirling of strands [29]. Although the main goal of hybrid

fibre architectures is to obtain reinforcing effects, the use of such systems could lead to synergistic behaviour [13, 28, 34].

1.1 Research Objectives

The overall research objective of this thesis is to characterise and model hybrid fibre architectures of randomly oriented strands of carbon/PEEK and CF tapes of carbon/PEEK, to understand their stiffness, strength, and failure characteristics under mechanical loading. Hybrid composites made of ROS and CF are manufactured by compression moulding process that demonstrates potential for low-cost and short manufacturing cycles. Three sub-objectives are recognized: a) to investigate the mechanical characteristics of hybrid fibre architectures of ROS and CF at the coupon level, when subjected to tension, and interlaminar shear loading; b) to propose predictive modelling techniques for ROS and hybrids for the calculation of strength and stiffness while accounting for the main failure mechanisms and progressive failure; c) to study the feasibility of using hybrid fibre architectures at part level, minimize variability and improve performance and processing aspects.

1.2 Thesis Outline

The manuscript-based dissertation is a condensed form of four manuscripts and additional chapters. Repetitive text (for example: introduction to the subject, manufacturing process, test configurations, etc) from the manuscripts is removed for brevity. References of all the manuscripts are synchronized to form the global reference list. In addition, global Appendices are defined for the thesis. Connecting text is included for coherence.

Chapter 2.0: Following this introduction, a relevant literature review on the mechanical characterization and numerical modelling of ROS and ROS-hybrid composites are presented

from Manuscript 1. Connections are drawn between the current state of knowledge in the open literature and literature gaps are identified.

The thesis is then categorized into Coupon level studies and Part level studies. Chapters 3.0-4.0 deal with experimental and modelling studies at the coupon level (tensile behaviour and interlaminar shear), while chapter 5.0 deals with the part level studies.

Chapter 3.0: This chapter discusses the work on the tensile behaviour studies at the coupon level. Sub-chapter 3.1 deals with the experimental work and is based on Manuscript 2. Sub-chapter 3.2 is a stand-alone chapter (non-manuscript based) dealing with the modelling of the tensile behaviour.

Chapter 4.0: This chapter discusses both experimental and modelling efforts on the interlaminar shear behaviour of ROS-hybrids through Manuscript 3.

Chapter 5.0: Through Manuscript 4, the chapter discusses the experimental work on stiffened panels of ROS-hybrids.

Chapter 6.0: This thesis ends with the summary of main results and contributions, as well as recommendations for future work. Supplementary material is included in the Appendices.

1.3 Manuscripts and Contributions of authors

Manuscript 1 (Chapter 2.0)

Visweswaraiah, S.B., M. Selezneva, L. Lessard, and P. Hubert, *Mechanical Characterization and Modelling of Randomly Oriented Strand Architecture and their Hybrids – A General Review.* Journal of Reinforced Plastics and Composites, 2018. **Published Online**.

Authors	Contributions
Swaroop B Visweswaraiah	- Identified the need for the review article - Categorized relevant literature, identified trends and challenges - Wrote the manuscript
Marina Selezneva	- Reviewed manuscript/ Provided latest articles/ Assisted in condensing the 'Review article'
Larry Lessard, Pascal Hubert	- Provided guidance, general direction to the research, and reviewed the manuscript

Manuscript 2 (Chapter 3.1)

Visweswaraiah, S.B., L. Lessard, and P. Hubert, *Tensile Behaviour of Hybrid Fibre Architectures of Randomly Oriented Strands combined with Laminate groups.* Journal of Composite Materials, 2018. **Accepted**.

Authors	Contributions
Swaroop B Visweswaraiah	- Conceptualized the idea, Studied the tensile behaviour - Fabricated and conducted experiments, Post-processed the results - Wrote the manuscript
Larry Lessard, Pascal Hubert	- Provided guidance, general direction to the research and reviewed the manuscript

Manuscript 3 (Chapter 4.1)

Visweswaraiah, S.B., L. Lessard, and P. Hubert, *Interlaminar shear behaviour of hybrid fibre architectures of randomly oriented strands combined with laminate groups.* Composite Structures, 2017. 176: p. 823-832. **Published.**

Authors	Contributions
Swaroop B Visweswaraiah	- Conceptualized the idea, Studied the interlaminar behaviour - Fabricated and conducted experiments, Post-processed the results - Developed the modelling work - Wrote the manuscript
Larry Lessard, Pascal Hubert	- Provided guidance, general direction to the research and reviewed the manuscript

Manuscript 4 (Chapter 5.0)

Visweswaraiah, S.B., N.Ohlmann, L. Lessard, and P. Hubert, *Flow-control and hybridization strategies for thermoplastic stiffened panels of long discontinuous fibers.* Journal of Reinforced Plastics and Composites, 2017. **36**(18): p. 1327-1342. **Published.**

Authors	Contributions
Swaroop B Visweswaraiah	- Conceptualized the idea, Studied the interlaminar behaviour - Fabricated and conducted experiments, Post-processed the results - Wrote the manuscript
Nicolas Ohlmann	- Assisted with the thermal simulations and experimental work
Larry Lessard, Pascal Hubert	- Provided guidance, general direction to the research and reviewed the manuscript

Chapter 2

Literature Review

Changes to Manuscript 1:

a) The manuscript summarizes the research studies on ROS architecture and their hybrids. Since the primary subject of this thesis is hybrid fibre architectures of ROS and continuous fibres, only a brief review of the ROS architecture is presented.

b) References and citations to the articles that are a part of current thesis are excluded from the manuscript.

c) Introduction section of the manuscript is removed to avoid repetition.

Manuscript 1

Mechanical Characterization and Modelling of Randomly Oriented Strand Architecture and their Hybrids – A General Review

Abstract

A comprehensive review of the mechanical characterization and modelling of randomly oriented strands (ROS) material architecture and their hybrids with laminates is presented. ROS composites are long discontinuous fibre preforms that exhibit excellent formability characteristics and stiffness properties comparable to Quasi-isotropic laminates, allowing their use in the manufacture of intricate geometric parts for automotive and aerospace industries. ROS architecture complements out-of-autoclave methods such as compression moulding, thermostamping and resin-transfer moulding leading to cost-reduction. Their applicability is limited to non-structural and low-load bearing applications due to their low strength properties. Continuous fibre (CF) aerospace preforms exhibiting excellent mechanical performance possess low formability characteristics and are confined to simple shell-like geometries with minimal curvatures, while incurring high-costs and long manufacturing times. Hybrid solutions of ROS and other material architectures represent a trade-off solution of formability and performance characteristics often yielding synergistic effects. Seemingly simple, ROS is a complex material system that poses several structural and process challenges. This work categorizes the pertinent research work from the literature on the mechanical characterization into the framework of a formal characterization environment of composite structures that includes the coupon, the part and structural levels. The manufacturing, dispersion methods and measurement techniques are qualitatively assessed with reference to the mechanical properties. The discussion on modelling

involves the identification of crucial characteristics of significant analytical and numerical modelling techniques devised for the prediction of the mechanical behaviour of ROS and their hybrids. Emphasis is on the methods of stiffness and strength prediction. Our perspectives on the effective use of ROS and their hybrids are discussed. Process characterization and process modelling of ROS and their hybrids are beyond the scope of this article.

Keywords: Randomly oriented fibres, Randomly oriented strands, Hybrid fibre architectures

2.1 Introduction

Randomly oriented strand composites and their hybrids are attractive material architectures but pose several structural and process challenges needing systematic categorization of the works in the literature. The characterization of ROS architecture and their hybrids can be broadly categorized into Mechanical and Process characterizations (Figure 2-1). The first part of the general review summarizes the literature on mechanical characterization of ROS and ROS-hybrids. Traditionally, the aerospace industry uses a multi-level building block approach for the substantiation of composite structures, due to the sensitivity of composites to out-of-plane loads, the multiplicity of composite failure modes and the lack of standard analytical methods [35]. The suitability of the building block approach is still in question for ROS based composites. Nevertheless, for the review, such a formal characterization defined by the coupon, the part and structural levels can provide a clear mapping of the literature on ROS/ROS-hybrid architectures. The second part of the article involves the identification of crucial characteristics of significant analytical techniques and numerical models devised for the prediction of the mechanical behaviour of ROS and their hybrids.

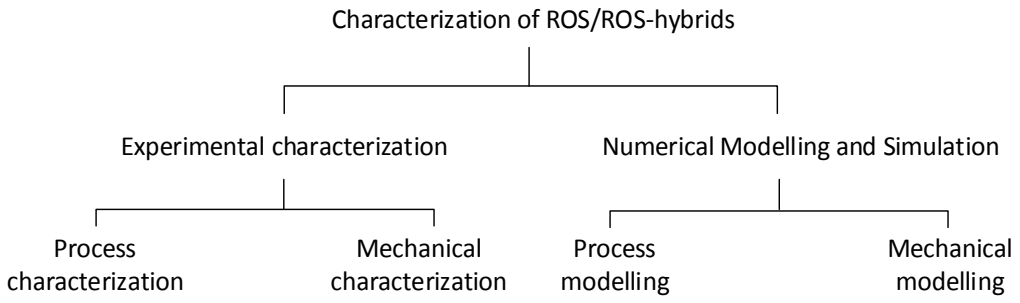

Figure 2-1: Sub-categories of the characterization of ROS/ROS-hybrids

2.1.1 ROS architecture

ROS composites have a three-dimensional (3D) microstructure, which is schematically illustrated in Figure 2-2. Several parameters cumulatively add from the micro to the structural levels and govern the performance. Parameters on the micro-scale are directly related to the properties of the fibres and the matrix. On the meso and macro-scale, however, properties are dependent on the strand parameters such as size, shape, overlap, orientation, dispersion and waviness. The manufacturing and dispersion methods drive many of these governing parameters. The effects of processing conditions on strand architecture are briefly discussed where relevant, as process characterization is not the main subject of the article.

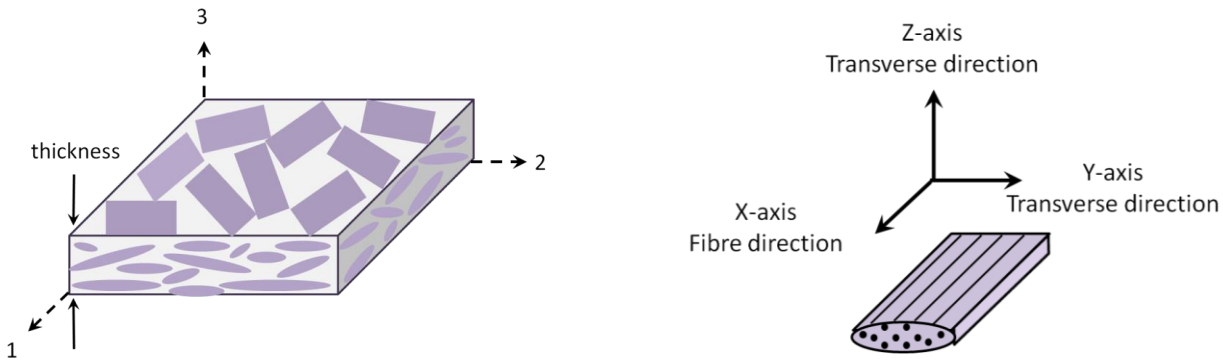

a) b)

Figure 2-2: Schematic representation of a) ROS composite and b) strand microstructure [12]

2.1.2 Manufacturing techniques and dispersion methods

Compression moulding [12, 36-38] (Figure 2-3) and thermostamping [3, 39] are the frequently-used manufacturing methods for forming of ROS composites since strands are typically pre-impregnated with either a thermoset or a thermoplastic matrix system. Alternatively, dry fibres bundles can be used to create a preform, which is then impregnated and consolidated via resin transfer moulding [40-42]. Among these manufacturing methods, researchers use two forms of raw material for preimpregnated strands: Sheet moulding compounds (SMC) and bulk moulding compounds (BMC). SMCs are produced by creating sheets with randomly oriented strands. Random deposition is achieved by dropping the strands onto a conveyor belt (with release backing) [43] or via a wet-type paper making process from BMC into an SMC [37, 44]. The sheets are then cut to the desired shape, stacked into the mould and compression moulded. With the BMC, the strands are shuffled, bulkily placed into the mould and compression moulded. This is a one step process, which makes it attractive from the industrial viewpoint. However, it leads to more variability of the strand placement and architecture. Researchers have adopted mainly three dispersion or stack methods for the initial placement of strands with BMCs: manual distribution (sequential/visual randomization) [12, 36-38], water/air dispersion [37, 44], and mat-layup methods [45]. Direct fibre preforming (DCFP) method, a suitable method for dry fibres, involves cutting the tows by a revolving chopper head and deposition onto a mould through a robotically controlled process. At the end of the process, a near net-shape preform is produced and is then impregnated and consolidated using resin transfer moulding (RTM) [40-42]. Inherent variability of ROS composites presents various challenges associated with material characterization and quality control and will be a recurring topic of these papers.

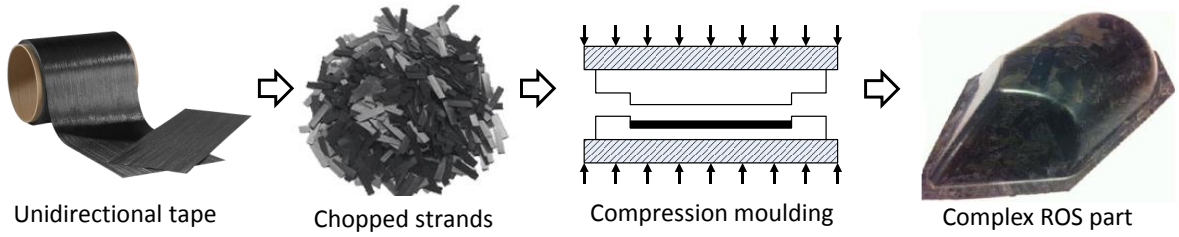

Figure 2-3: Compression moulding of an ROS part [46]

2.1.3 Strain measurement methods

Feraboli et al. [47] addressed the issue of variability in the modulus data by evaluating different measurement techniques which include an extensometer, strain gauges of various lengths and the digital image correlation (DIC) technique. Data obtained with the DIC technique depicted large strain variation on the surface of the specimen which makes extensometers and strain gauges, even large ones, inadequate for global strain measurement. Additionally, Johanson et al. [48] reported a noticeable difference between strain fields captured with DIC from the different sides of the specimen. Hence there was a gradient of local through-the-thickness strains and important failures could be missed with one-side strain monitoring. Overall, the DIC technique was found to yield the most accurate and repeatable measurement of modulus by averaging the full-field strain values [36] and has become the standard technique for ROS [12, 13, 38, 41, 49].

2.2 Mechanical Characterization

2.2.1 ROS architecture

The Coupon and Part levels on ROS architecture are listed in Table 2-2. It is, however, important to note that the behaviour of ROS is reported to be a function of mainly strand size (strand length, strand width) and specimen geometry (specimen thickness, specimen width). In general, the effect of strand length is more pronounced on strength than modulus, with mostly an

increasing trend with strand length but accompanied by increased variability [11, 44]. The modulus of ROS with most of the strand sizes were comparable with that of quasi-isotropic (QI) laminates while the strength showed a range of values between 15–70% [11, 12, 37, 44, 45] of the strength of QI laminates. The material properties are highly variable on the meso-scale due to the heterogeneous structure. The failure modes reported are mostly matrix dominated (transverse strand cracking, strand debonding and longitudinal strand splitting) in addition to secondary fibre failures. The failure modes were spread through the weakest path of resistance and were frequently redirected in the longitudinal and transverse directions in a staggered pattern. Due to similar magnitudes of tensile, compressive and shear strengths, Selezneva [12] used tensile properties as an approximation for other two strengths, thus, reducing the preliminary tests needed to evaluate the performance of new ROS materials. Analogously, tensile and compressive moduli were similar, and in-plane shear modulus was approximated (<5% error) based on the assumption of transverse isotropy. Overall, the knockdown of shear strength from CF to ROS was not as drastic as in the case of tension or compression loading. The authors recommended the use of ROS for applications where shear was the dominant load. Further, Selezneva et al. [12] measured the out-of-plane shear strength by double-notch shear (DNS) and the short-beam shear (SBS) tests, for a range of strand sizes and aspect ratios of ROS material. DNS tests led to proper shear fracture between the notches, whereas SBS resulted in multi-mode failures and lower values than those measured for DNS. It was noted that determining the out-of-plane shear properties was crucial as stress gradients in the interlaminar directions could cause delaminations in intricate parts of ROS architecture.

Authors	Strand material [Fibre/Matrix (Type)], Parent material)	Raw material form	Dispersion method	Manufacturing method	Coupon level: Tension (T) , Compression (C), In-plane shear (S), Interlaminar shear (SBS/DNS), Flexural (3P/4P), Fracture toughness (Mode I/II/III), Fatigue (T-T, T-C), Open-hole tests (OHT/OHC), Bearing strength, Others	Part level: Structure, Test
Feraboli et al. [11]	[Carbon/Epoxy (T700/2510)], UD tape	BMC	Manual and visual randomization	CM	T, C, 3P, OHT, OHC	
Eguémann et al. [38]	[Carbon /PEEK], UD tape		Manual		T	Hinge, Structural
Selezneva et al. [12], Landry et al. [50], Leblanc et al. [51, 52]	[Carbon /PEEK], UD tape		Sequential manual		T, C, S, SBS, DNS, T-T	T-shapes, Pull-out strength
Yamashita et al. [37], Nakashima et al. [53], Wan et al. [44, 54], Lyu et al. [55], Guo et al. [56], Meng et al. [57], Yamashita et al. [58], Fujita et al. [59], Toyoda et al. [60]	[Carbon /PA6], ultra-thin UD tape	SMC	Water, air dispersion		T, C, 3P, 4P, Mode I, Out-of-plane shear modulus using vibrations, Bearing strength, Lightning strike damage	S-shapes and Hat-shapes, Flexure
Jin et al. [45]	[Carbon /Epoxy (T40/800B with Cytec CYCOM 5320-1 Epoxy)], UD tape	BMC	Mat layup, Mechanical agitation		T	
Han et al. [61]	[Carbon /Polyetherimide], UD tape		Manual		T, C, S	L-angles, ILTS
Boursier et al. [62]	[Carbon /Epoxy (HexMC)], UD tape	SMC	Manual		T-T, Compression after Impact (ETW)	
Qian et al. [41]	[3 K HTA/5631 polyurethane], UD tape	SMC	DCFP	RTM	OHT	
Jacob et al. [63]	[P4, CCS-100, HexMC], UD tapes	SMC, BMC	Manual	CM	Crash worthiness	
Rasheed et al. [64]	[5HS carbon/PPS] - Fabrics	BMC			T	
Tencate [65]	[Cetex] (multiple variants)	SMC			T, C, 3P, OHC	
Hexcel [43]	[HexMC] (multiple variants)	BMC			T, C, SBS, Flexure	
Fortin et al. [39]	[Carbon /PEEK], UD tape			Thermoforming		L-angles, ILTS
Kravchenko [66]	[AS4/PEKK, AS4/PEEK], UD Tapes		Manual	CM	T	

3P and 4P signify three-point bending and four-point bending tests
ETW – Elevated Temperature Wet conditions. Unless stated all tests were carried out at room temperature (RT); OHT and OHC signify Open-hole tension and Open-hole compression tests
T-T and T-C signify Tension-Tension and Tension-Compression fatigue tests; ILTS signifies Interlaminar tensile strength

Table 2-1: Summary of the coupon level and part level testing efforts on ROS from literature

2.2.2 Hybrid fibre architectures

Research work on hybrid fibre architectures can be grouped into two categories: a) processing studies demonstrating the feasibility of integrated processing/co-moulding of complex hybrid structures with an emphasis on the improvement of the interfacial behaviour; b) studies to improve specific mechanical characteristics or studying the extent of the reinforcement effect.

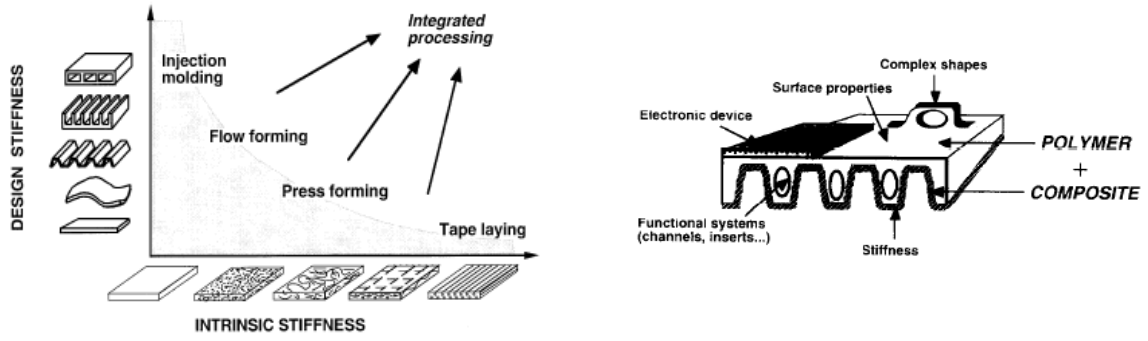

a) b)

Figure 2-4: a) Design and intrinsic stiffness of polymer composites for different processing techniques [16]; b) Schematic illustration of an example hybrid part [16]

Processing studies

The literature on the processing of hybrid fibre architecture of ROS and CF laminates is scarce. Thus, studies that share similarities with hybrids are discussed briefly. Bourban et al. [16] presented the concept of integrated processing (Figure 2-4.a) of ROF-hybrids (Figure 2-4.b) of CF and Glass Mat Thermoplastic (GMT) through a sequential process. Luo et al. [67] derived a relationship between the compression pressure and V_f of a multimat, which consisted of a layer of glass weft knit fabric sandwiched between two layers of random glass mat (Figure 2-5.a). Fibre relaxation was explained in terms fabric stiffness and volumetric dissipation energy. Wakeman et al. [68] explored the co-moulding of random-reinforced GMTs with commingled E-glass and polypropylene fabrics. High charge and mould temperatures were suggested for

superior impregnation. Maintaining consolidation pressure for a minimum period was critical to eliminate mid-plane voids. Wakeman et al. [15] demonstrated significant stiffness improvements and feasibility of processing carbon fibre reinforced polyamide materials with ribbed structures in short times using three steps: plate impregnation, stamping, and over-moulding (Figure 2-5.b). Wakeman et al. [69] investigated the effect of forming conditions (e.g. preheat cycle, UD tow placement rate and pressure) on the structural integrity (e.g. void content, tensile properties) of a compression moulded beam with UD tow inserts.

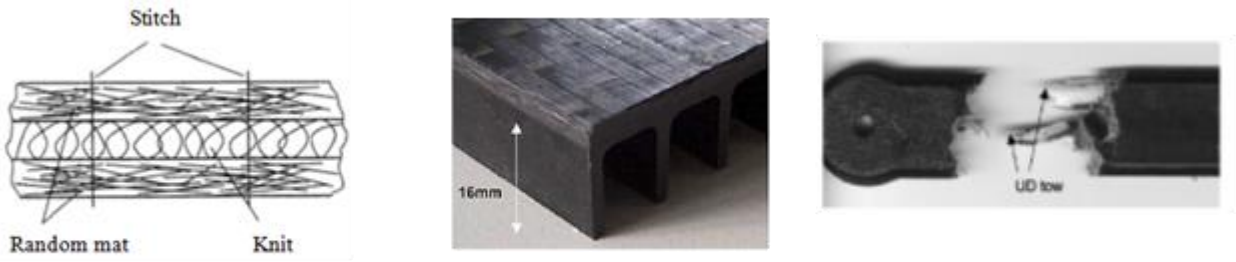

a) b) c)

Figure 2-5: a) Hybrid multimat [67]; b) Sandwich structures to integrate material and shape stiffness [15]; c) Compression moulded beam element with UD tow inserts [69]

In a study focused on the flow and mechanical properties of ROS-hybrids, Corbridge et al. [32] used HexMC with 50 mm fibre length, and UD prepregs under high flow compression moulding. Using a grid strain method, quantitative analysis of the distortion of the UD fibres in terms of translations and rotations were determined. Flow of the ROS material caused shearing of the ply when the fibres were aligned transversely to the flow direction, causing local changes in V_f and fibre waviness. Further, ply migration occurred when the UD fibres were aligned with the flow direction. Staging the resin to 50% cure reduced ply distortion during moulding whilst maintaining interlaminar performance. Adding an interfacial ply of 90-degree orientation between the reinforcing UD fibres and the ROS successfully prevented distortion to the UD

fibres by avoiding shear thinning and fibre migration. The addition of the 90-degree ply resulted in a negligible impact (<8%) to the flexural stiffness of the hybrid (Figure 2-6.a).

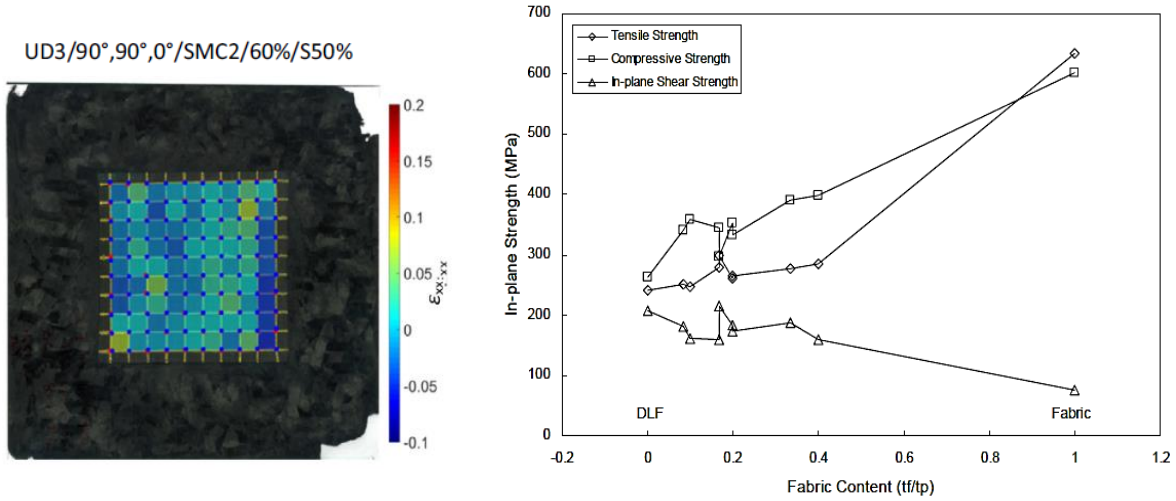

a) b)

Figure 2-6: a) Ply distortions in hybrid specimens with and without interfacial ply between SMC and UD plies [32]; b) In-plane strength with ROS-fabric hybrids as a function of fabric content [33]

Reinforcement effect

Coupon level

Some significant studies on ROF hybrids share commonalities with ROS-hybrids. Lee et al. [70] worked with CF-short random fibre mat hybrids, and classified hybrids into mixed, interlayer and sandwich types. Selmy et al. [71-73] studied the tensile, interlaminar and bending properties of glass/epoxy hybrids of unidirectional (U) and discontinuous-random (R) fibres. Relative proportions and stacking sequences within a hybrid were examined. Cabrera-Rios et al. [74] employed the per-ply method to fabricate hybrid configurations of carbon and glass fibre SMCs and measured their tensile and flexural strength. Glass-carbon-glass hybrid stacking configuration yielded the best tensile strength-to-weight ratio compared to carbon-glass-carbon. Jens et al. [75] combined SMC called HUP27 and fabric/UD prepregs in one-shot compression

moulding process to create load bearing out-of-autoclave parts. Mallick [76] studied the extent of fibre misorientation due to resin cross-flow and its effect on the tensile strength of a compression moulded hybrid of UD and SMC. Numerous studies on ROF hybrids show significant increase the interlaminar fracture toughness and consequently energy absorbing capability of composite structures and crash resistance [77-79].

Han et al. [33] studied the bearing failure behaviour of bolted joints in ROS composites co-moulded with fabric layers at various lay-up locations and proportions. The tensile and compressive strengths were improved with an increase in the fabric content, while the in-plane shear strength is reduced by increasing the fabric content except for the range of (10-20%) fabric content (Figure 2-6.b). The effect of geometrical parameters of bolted joint specimens, the edge distance ratio (*e/D*) and width to diameter ratio (*w/D*), on the bearing response and failure mode were investigated. The addition of one fabric layer at the middle of a ROS panel provided 5~12% and 5~20% increase in bearing strength and stiffness, respectively. Both ROS/fabric and ROS only specimens demonstrated a combination of bearing and cleavage (tension with shear-out), while a combination of bearing, shear-out, and wedge-split failure modes occurred for the fabric only laminates.

Structural level

Leblanc et al. [80] co-moulded ROS and UD plies in T-shaped parts using compression moulding. Addition of the tapes induced high ply waviness at the junction of the flanges and the web, caused by the strand flow. Nevertheless, the use of hybrid configuration reportedly increased the pull-out strength of the T-shaped parts by about 45%. Evans et al. [34] investigated co-compression moulding of hybrid fibre architectures of DFC and UD plies. The effect of ply layups in the transition zone from the CF plies to the DFC material were studied using flexural

performance and Mode-I fracture toughness. T700 12K carbon fibre tows were chopped to a fibre length of 25 mm and epoxy resin was added. The target fibre volume fraction for the charge was 50%. The UD ply was a carbon non-crimp fabric (NCF) with multiaxial E-glass stitching, at 90° and ±45°. The percentage volume content of UD was 0% (DFC only), hybrids between 20-80%, and 100% (UD only) in a constant thickness (3 mm) specimen. The UD plies were positioned at the upper and lower tool surface (UD/DFC/UD) to minimize the out-of-plane ply waviness. The experimental data demonstrated slight positive synergies from the RoM behaviour (Figure 2-7.a) with strength with lower % of UD in the hybrid similar to [13]. The baseline tensile strength for DFC was improved by 110% with 20% UD content, with about 25% decrease in the transverse strength. Continuous-discontinuous joint design was suggested to incorporate tapering of the continuous fibre plies to achieve an interface angle of <7° to minimize peel stresses. Fracture toughness of the system was improved by ~23-37% with the use of DFC, due to its ability to resist crack development by 'fibre bridging' (Figure 2-7.b). Fette et al. [81, 82] studied the level of automation of single-stage compression moulding of ROS-hybrids or hybrid SMC in an aerospace production environment. Lightweight designs of ROS-hybrids were proposed by load path optimisation achieved by tailored continuous fibre placement patches within a complex SMC based ROS part. Hybrid-SMC of aircraft fairings were manufactured and impregnation investigations on them showed that the continuous fibre rovings were well impregnated by the SMC resin system. Hybrid-SMCs demonstrated short curing cycle times in the range of 120-180 seconds.

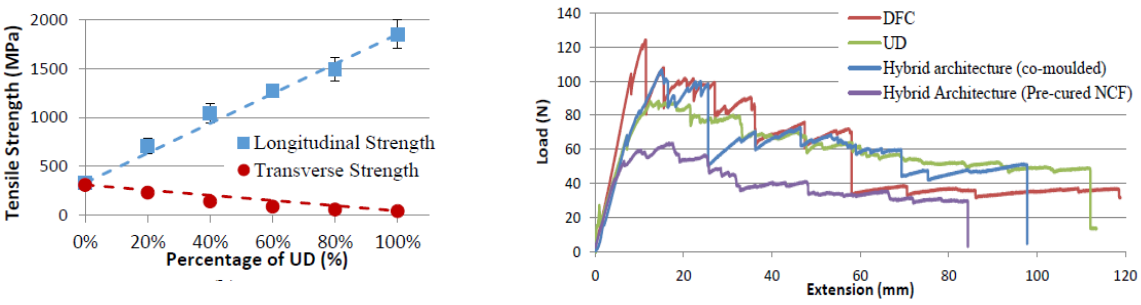

Figure 2-7: a) Longitudinal and transverse strengths if ROS-UD hybrids as a function of %UD [34]; b) Load-displacement curves for double cantilever specimens representing fracture toughness

Researchers have sought for the statistical lower bounds or the basis allowables to quantify the design allowables [12, 29, 83-85] and for certification of ROS based composites. Due to the complexities and gamut of design possibilities with ROS, Harban and Tuttle [84] proposed the use of stochastic based modelling accompanied by selective testing efforts.

Authors	[Strand material] + Ply/laminate	Raw material form	Dispersion method	Manufacturing method	Coupon level	Part level
					Tension (T) , Compression (C), Interlaminar shear (SBS/DNS), Flexural (3P/4P), Fracture toughness (Mode I/II/III), Fatigue (T-T, T-C), Open-hole tests (OHT/OHC), Bearing strength	Structure, Test
Han et al. [33]	[12k AS4/PEEK UD tapes] + 3K HS fibres 5H Satin	SMC	Manual	CM	T, C, S, Bearing strength	
Corbridge et al. [32]	[HexMC] + UD tapes and CP	BMC	Manual		4P	
Leblanc et al. [52]	[CF/PEEK UD tape] + UD tapes		Sequential manual			T-shapes, Pull-out strength
Evans et al. [34]	[T700 12K/epoxy UD tapes] + NCF UD tapes		Manual		T, Mode I	Continuous-discontinuous joints, Flexure

Table 2-2: Summary of the coupon level and part level testing efforts on ROS-hybrids from literature

2.3 Modelling of ROS and ROS-hybrids

2.3.1 Analytical modelling

The earlier modelling efforts were aimed at adapting existing models for discontinuous and continuous fibre composites to ROS with varying success. ROS can be regarded as a system of high-volume fraction ROF. A thorough review and evaluation of ROF models can be found [9, 86-88]. Although the models for ROF are relevant to ROS, two aspects inhibit the direct use of these theoretical models: a) the matrix dominated failure mechanisms involved in the ROS architecture, b) definition of certain model parameters specific to that of ROS such as the aspect ratio. For fibres, the aspect ratio is *l/d*, which defines material attributes. For ROS, different opinions exist for the definition of the 'diameter' of the strand and the range of magnitudes spans multiple geometric scales: fibre diameter (7 µm), strand thickness (50-150 µm), strand width (3-15 mm), etc. Three categories of analytical models have been recognized based on the modelling principles into: a) models coupled with homogenization schemes, b) analytical models coupled with laminate theories c) Phenomenological models.

Models coupled with homogenization schemes

Kirupanantham [89] defined an effective tow diameter, which gives a circle with the same cross-sectional area as the fibre bundle. The Kelly-Tyson model [5] was used to predict the strength and shear-lag model to predict stiffness. A Krenchel orientation efficiency factor [90] of 0.375 was used to account for the random orientations. Another commonly used modelling strategy for short fibre composites is the Mori-Tanaka model [91]. The calculation of the strain concentration tensor for a strand is uncertain as the original expressions derived by Eshelby are for ellipsoidal inclusions. To avoid this dilemma, Jain et al. [92] proposed the extraction of dilute strain

concentration tensors from FE analyses in conjunction with analytic mean field homogenization techniques to predict the stiffness characteristics of ROS of arbitrary size and orientation. However, Jain also discusses a particular issue of applying the Mori-Tanaka formulation to anisotropic inclusions [93], as it is known to give a non-symmetric stiffness matrix. This is non-physical. They showed that for non-ellipsoidal inclusions the percentage of non-symmetry is between 5 and 8, which is not negligible. Lielens et al [94] also showed that M-T gives non-physical results when applied to two-phase composites containing inclusions of different shapes and orientations. Wan et al. [44] proposed to use a 3D strand aspect ratio (K_{CTT}) (Equation 2-1) in terms of tape length (*a)*, width *(b)* and thickness *(c)* instead of *l/d* ratio. MicroCT data was used to define the 3D orientation matrix. For the tape lengths of 12-30 mm in length, the equivalent aspect ratios were between 100-1000. Analytical mean-field homogenization based on the Mori-Tanaka model [95] gave accurate estimations when the aspect ratio ranged from 200-500 and fibre volume fraction (V_f) was higher than 50%.

$$K_{CTT} = \frac{\sqrt{a^2+b^2+c^2}*\left(ab + a\sqrt{b^2+c^2} + b\sqrt{c^2+a^2} + \sqrt{a^2b^2+b^2c^2+c^2a^2}\right)}{2\sqrt{6}abc} \qquad \text{Equation 2-1}$$

Analytical models coupled with laminate theories

At the meso-level, ROS composites have a layered structure and resembles that of a laminate. This observation has motivated several researchers to adopt a laminate analogy with a strand placement procedure [96, 97]. Specimens were discretized into regions with different randomly generated layups. First, the equivalent properties of each partition were calculated, and then a second homogenization step was performed to determine the equivalent properties of the entire specimen. Sato [96] used this methodology to predict the in-plane modulus and its variability of a tensile ROS specimen while Nakashima et al. [97] investigated the statistical characteristics of

flexural modulus of UT-CTT using for both 3-point and 4-point bending test conditions. Equivalent square plies representing the area and orientation of the strand were stacked within the specimen area and laminate analogy was applied. Equivalent modulus of each layer in the laminate was calculated using Equation 2-2, and a compounding process was adopted to obtain the global properties of the model (Figure 2-8).

$$\frac{E_1}{E(\theta)} = cos^4\theta + \frac{E_1}{E_2}sin^4\theta + \left(\frac{E_2}{G_{12}} - 2\nu_{12}\right)cos^2\theta sin^2\theta \qquad \text{Equation 2-2}$$

where E_1 is the longitudinal stiffness, θ is the ply orientation, E_2 is the transverse stiffness, υ_{12} is the Poisson's ratio, G_{12} is the in-plane shear stiffness.

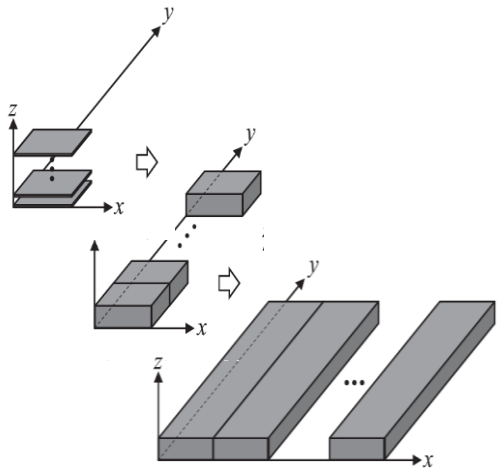

Figure 2-8: Square ply and compounding process [97]

Phenomenological models

Simplified phenomenological strength models were proposed by Selezneva et al. [98] for strands of UD tapes and Rasheed et al. [64] for strands of woven fabrics. Typical characteristics of these models are: a) the resemblance to the brick-and-mortar microstructure (Figure 2-9.a) of the ROS composites that enabled them to capture strand debonding, which is recognized as the dominant failure mode for ROS composites, b) the use of the weakest link or the shortest path to failure.

Similar models have been developed for characterizing the failure of nacre by Bekah et al. [99] and for aligned discontinuous fibre composites by Pimenta et al. [100].

In the methodology proposed by Selezneva et al. [13], two failure modes are considered, strand failure and strand pull-out. First, a 2D microstructure with random strand placement and orientation is generated, then a network of all the possible failure paths is assembled and, finally, the shortest crack path is found. Each segment or link of the network represents either the load required to fracture the strand or to break the bond between two strands. Strength of each strand was calculated using the CLT and Hashin's failure criteria. While the strength of the overlap (σ) between strands was calculated using the strength-based (Equation 2-3) and toughness-based (Equation 2-4) failure criteria.

$$\sigma = \frac{L_o \tau_i}{t_b} \qquad \text{Equation 2-3}$$

$$\sigma = \sqrt{\frac{2E_b G_{IIc,IL}}{t_b}} \qquad \text{Equation 2-4}$$

where L_o is the overlap length, t_b and E_b are the strand thickness modulus, and τ_i and $G_{IIc,IL}$ are the matrix shear strength and mode II interlaminar fracture toughness. An example of a generated 2D microstructure and the calculated failure path is shown in (Figure 2-9.a). The colour map corresponds to different strands off-axis angles.

Rasheed et al. [64] defined the crack path in the random structure by tortuosity, which is a ratio of the total length of the crack to the thickness of the specimen. These tortuosity values were translated into strengths, based on shear-lag theory. Using geodesic distance transformation, the

shortest crack path assuming cracks initiated in the top plane. The method was proposed for strands of woven fabrics and considered two failure criteria: fibre/matrix failure and the matrix strength criteria.

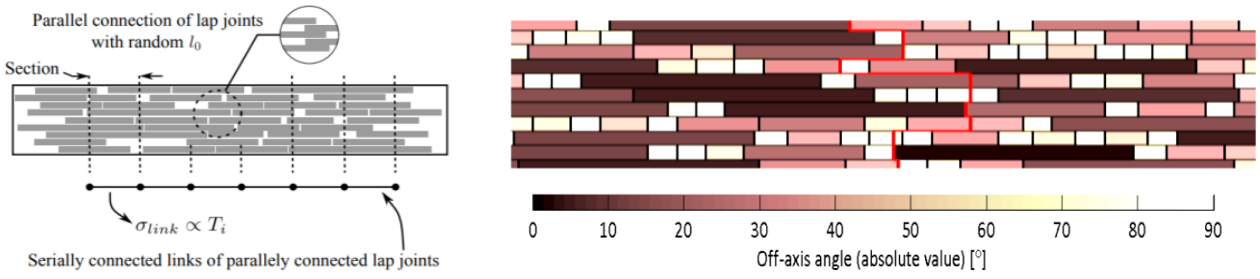

a) b)

Figure 2-9: a) Hypothesized parallel-series of lap joints [64]; b) Model simulating fracture paths in ROS, by Selezneva et al. [98]

2.3.2 Numerical modelling

Researchers have sought for the statistical lower bounds or the basis allowables to quantify the design allowables [12, 29, 83-85] and for certification. Due to the complexities and gamut of design possibilities with ROS composites, Harban and Tuttle [84] proposed the use of stochastic based finite element (FE) simulations accompanied by selective testing efforts. FE modelling accompanied by representative volume element (RVE) definition and stochastic approaches is the only numerical modelling approach found on ROS/ROS-hybrids. The modelling approaches can be classified into three categories based on their scale into: micro, meso and global-local models. These are further categorized based on their methodologies.

Micro-mechanical models

FE models developed for simulating the behaviour of ROS share commonalities with models for ROF, with reference to the principles. In a micro-mechanic based 3D FE model for ROF, Pan et

al. [87] used a modified random sequential absorption algorithm to generate an RVE and coupled it with a homogenization scheme. The fibre-matrix interfacial behaviour was modelled with cohesive elements using a traction-separation law. Multiple realizations indicated that the fracture toughness and interfacial strength governed the failure compared to the matrix cracking and fibre breakage. Ionita et al. [8] proposed a 2D model with the laminated random strand method to evaluate in-plane stiffness, strength and creep behaviour in random strand carbon fibre/urethane of high strand aspect ratios. A random network of strands was generated, as shown in Figure 2-10.b, to create a single "strand layer" located at a certain position from the centerline of the composite followed by the generation of strand layers stacked to achieve the desired laminate thickness. Strains were computed using classical laminate theory (CLT) and strengths through a progressive failure analysis. Multiple "moving windows" were generated to quantify scatter and noted that the isotropy diminishes with an increased "window" size. The method accounted for fibre crimping at the fibre intersection points through a knockdown factor. Works by Harper et al. [101-104] outlined a 2D FE model coupled with a novel meshing method for discrete continuous fibre plastics (DCFP) system to predict in-plane elastic properties of DCFP having narrower fibre bundles and lower V_f comparison to ROS. Fibre bundles were idealized as 1D beam elements and the matrix was modelled using 2D plane stress elements (Figure 2-11.a). TIE constraints in ABAQUS were used for the connections while fibres were allowed to intersect [104]. The authors obtained approximations using Saint-Venant's principle assuming the RVE was embedded in a homogeneous/heterogeneous material used to transmit the load (Figure 2-11.b).

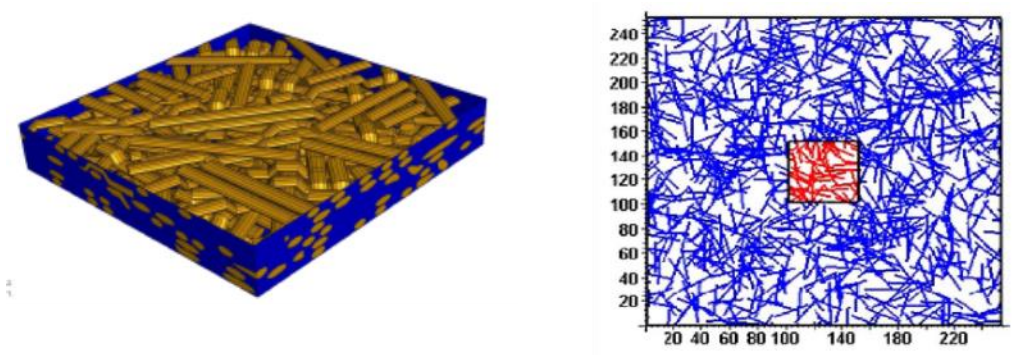

a) b)

Figure 2-10: RVEs of ROF system (V_f = 35 %) [87]; b) Laminate random strand method and moving window scheme [17]

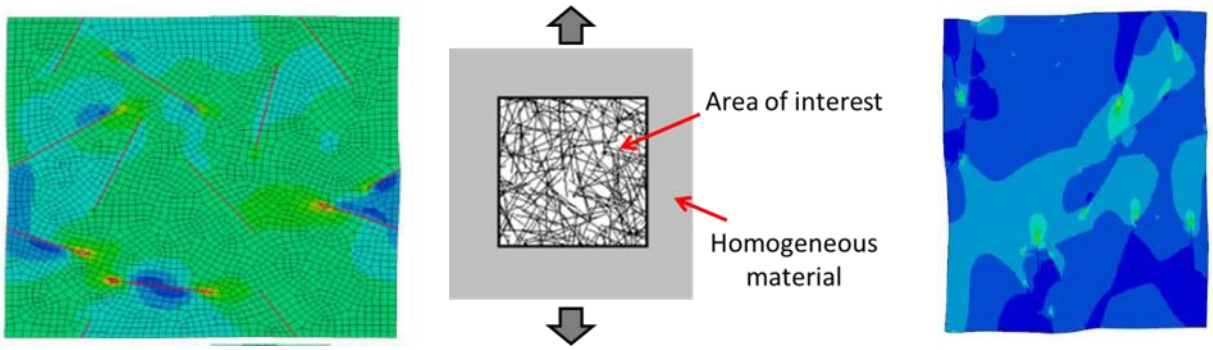

a) b) c)

Figure 2-11: 2D FE for in-plane properties of DCFP: a) mesh of the matrix with 1D beam elements that represent fibres; b) Application of the boundary conditions using at homogeneous material; c) Von-Mises stress contour plots for an RVE [101, 103]

Meso-level models

Applicability of a micro-mechanical approach to high volume fraction and large aspect ratios systems such as ROS is computationally intense, thus, authors simplify the FE simulations by using one level of RVE definition for the micro-scale. The first group of models employs simplistic strand representations with laminate analogies. Feraboli et al. [23] proposed a modified laminate analogy to capture the tensile modulus and its variability. A randomization process was employed to generate statistical distributions of fractions and orientations of chips

within window sizes called the Random Representative Volume Element (RRVE). The size of the RRVE was based on the pattern of alternating regions of high and low strain gradients of a characteristic shape and size obtained from DIC. Symmetric quasi-isotropic virtual laminate properties equivalent to the random layup were applied to RRVE and average elastic properties were calculated using CLT. Using an FE model, the structure was discretized into multiple RRVEs, whose properties were generated independently of the neighbouring ones, and were solved simultaneously (Figure 2-12.a). The RRVE size was 12.7 mm x 12.7 mm. The inconsistencies between the partition size and strand size in the physical specimen and the inability of the model to represent strand continuities across partitions limits its use for strength predictions. Harban and Tuttle [84] employed an FE modelling approach with a Monte-Carlo method to facilitate the certification for discontinuous fibre composite (DFC) structures based on analysis and minimal experimental validation. Stiffness and strength of both notched and unnotched DFC specimens under tensile loading were predicted using a stochastic laminate analogy (SLA) similar to that proposed by Feraboli et al. [105]. Head [106] obtained the optimal size of the RRVE as 19.1 mm x 19.1 mm at generic locations and 3.18 mm x 3.18 mm at the boundaries by comparisons with the experimental surface strains. Ply failures and a damage accumulation model based on the ply discount scheme drove fracture predictions based on Tsai-Wu criterion, while the important characteristic failure modes such as delamination were not captured. Nevertheless, the damage patterns from experiments were in qualitative agreement with experiments and reiterated the use of B-basis design allowables; the usual practice in composites certification. The work share similarities with [107]; both are limited to stiffness predictions and ply-failures only. In an interesting research, Li et al. [108] demonstrated through experiments that the equivalent laminate assumptions were suitable for predicting the modulus of

discontinuous composites, but cannot predict strength without considering the local heterogeneity in their microstructure. Specimens with thick and thin strands were compared. Although the equivalent laminate and ROS specimens demonstrated similar failure modes (tow fracture and tow pull-out under uniaxial tensile loading) the tensile strengths of thin-strands in both cases were higher than that of thicker strands. Earlier onset of tow-debonding/ply-delamination caused by a smaller tow aspect ratio l/t ratio led to matrix shear failure mode while the onset of delamination was quicker in thick strands as explained through the fracture toughness criteria. Heterogeneity and variability of the microstructures in thicker tow specimens were other attributes that led to their low properties. Selezneva et al. [107] proposed a stochastic strand generation procedure coupled with an FE technique to estimate stiffness and strength of ROS while considering the gradual transition of strands between partition, inspired by the works on oriented strand boards [109-111]. The specimen was discretized into small partitions and local strand layup. This geometry was populated with strands that have random orientations and positions. A FE model with Hashin's failure criteria and progressive failure analysis using fracture energy evolution law was generated in ABAQUS to simulate the stress-strain response. The variability of the strain field and the presence of "weak-spots" were captured independent of the partition size and shape, as strands shared multiple partitions. The failure was based on the "weakest-link" principle and was matrix-dominated (Figure 2-12.c). Inability to capture interlaminar behaviour overestimated the strength predictions. The number of strands at a location was variable in the through-thickness direction. To achieve a uniform thickness everywhere, the thickness of each 'ply' in the partition was 'scaled' such that total thickness was a constant, without compensating for their properties. Kravchenko [66] extended the understanding of aligned stack of platelets to ROS morphology. The "digital twins" of ROS test

specimens were created by mapping the local average fibre orientations determined from the density gradients of the X-ray computed tomography (CT) scans, on to a CT-volume-based hexahedral finite element mesh. A Voxel based meshing process from DIGIMAT software was employed to generate samples of material morphology as per a 2D orientation tensors. 3D progressive failure analysis based on continuum damage mechanics for platelet damage modes was coupled with a cohesive zone modelling to capture the dis-bonding between platelets and implemented in ABAQUS software (Figure 2-13). The effect of the strand width, strand length, strand length-to-thickness ratio, and thickness of the specimen on the tensile properties were simulated and compared with experimental data. The methodology yielded reasonably good results despite the absence of resin-rich areas, residual stress and through-thickness damage evolution effects. It was noted that average surface-viewed strains from DIC images driven by the meso-scale heterogeneities near the surface of the coupon could be inaccurate if used to calculate a modulus for the entire region volume due to the exclusion of variations in microstructure in the through-the-thickness direction.

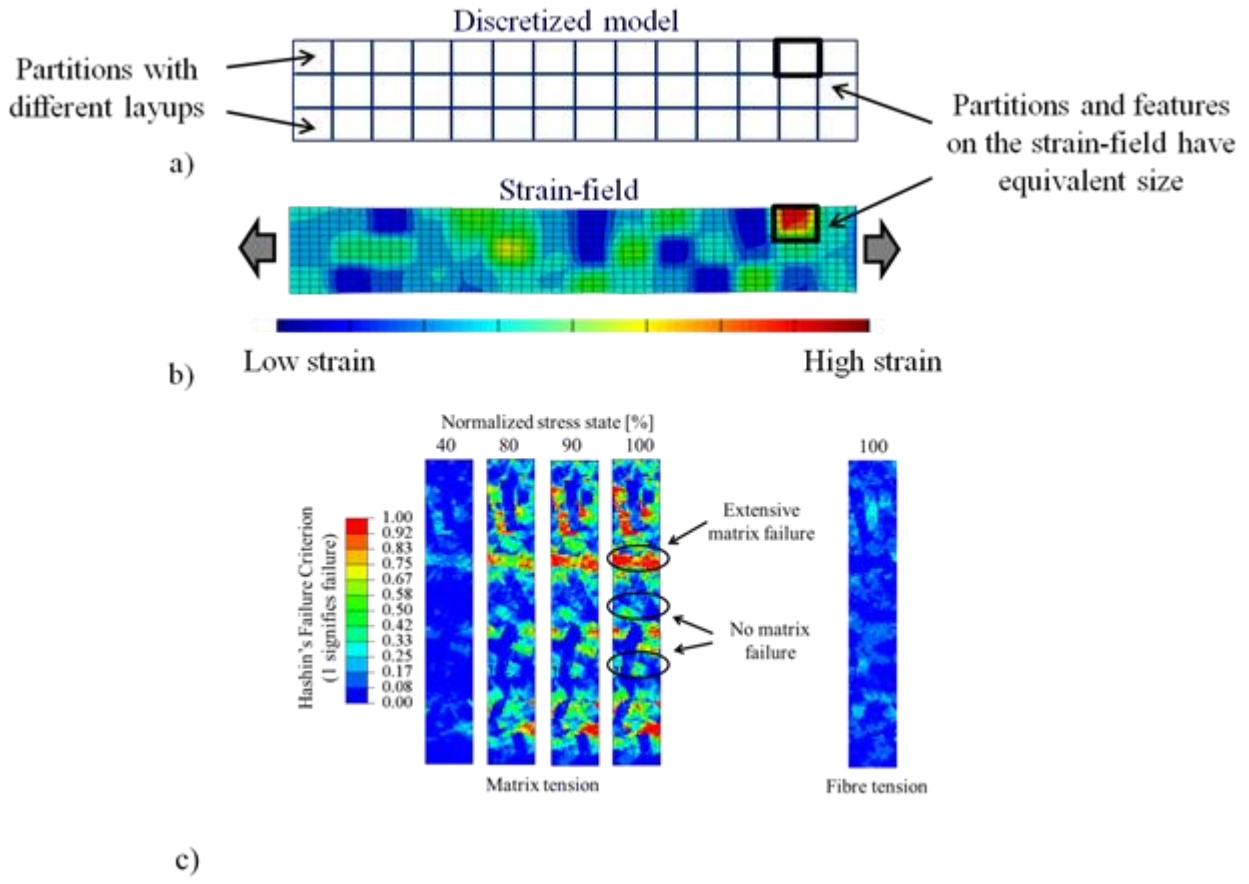

Figure 2-12: a) FE model with RRVE or partitions; b) Resultant strain-field adapted from [105] (colour map corresponds to strain variability); c) Hashin failure contours for matrix and fibres as a function of loading showing matrix dominated failures [107]

The second group of models employs physical strand modelling. Harper et al. [112] modelled ROS systems (with high filament count bundles (>3k) and high (50%) fibre volume fractions) through a geometrical modelling scheme involving three algorithms: a deposition algorithm to determine initial bundle locations and orientations; an intersection-elevation algorithm to detect and avoid bundle–bundle intersections and a spline interpolation algorithm to produce smooth curved fibre bundles. The strands were modelled as shells in an RVE of 38 x 38 x 3 mm (Figure 2-13.b). The effect of consolidation pressure on strands and the resulting out-of-plane waviness was accounted for. Tensile modulus and ultimate tensile strengths were predicted with errors <4-

5% at volume fractions between 40 and 55%. Although the model simulated transverse strand cracking and bundle failures due to shear, strand debonding; a matrix dominated failure was ignored due to the limitations of the tie constraints used for the fibre-matrix interfaces. Larger errors were reported for the ultimate compressive strength (20%) and shear strength (40%) predictions, as some of the dominant failure modes such as fibre buckling were ignored. In a recent work on modelling, Jin et al. [113] discussed pros and cons of FE techniques such as cohesive surfaces, tie constraints and embedded regions in the context of ROS. A combination of tie constraints with cohesive elements between the fibre strands and resin matrix was reported to capture the dominant interfacial debonding mode. Finally, tensile testing and FE simulations of ROS coupons made of T40/800B/epoxy unidirectional strands of 10 mm x 20 mm revealed good stiffness match. Shah et al. [114] proposed a 3D modelling coupled with a randomization process for strand generation and progressive damage analysis methodology for ROS. The model was able to capture out-of-plane effects, interlaminar shear effect, and stress concentration effects at the end of strands. A micro-mechanic failure-based criterion was used to predict failure in DFC by considering constituent properties. The tensile, compressive and flexure behaviour were investigated and compared with the experimental results available in the literature. Qian et al. [115, 116] proposed optimization methodologies for stiffness of discontinuous fibre composites and demonstrated it on a case study.

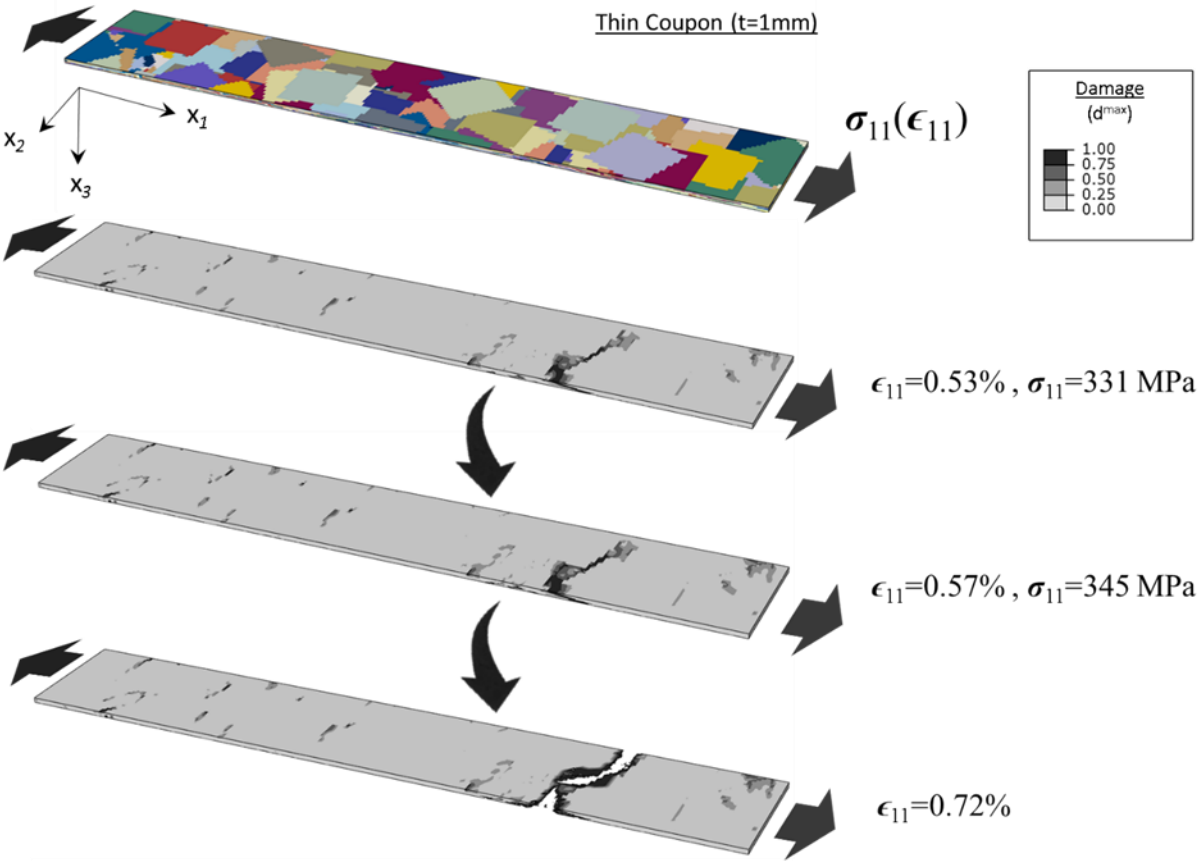

a)

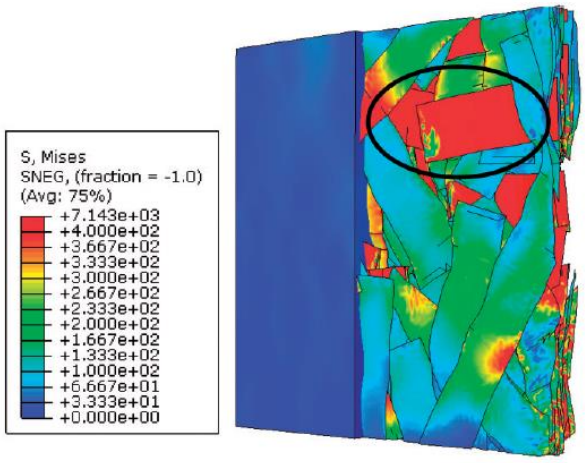

b)

Figure 2-13: a) Progression of failure under tensile loading in a 3D Continuum damage mechanics model under tensile loading [66]; b) Von-mises plot for a 10% V_f, 38x38x3mm RVE prior to coupon failure under tensile load in the strands [112]

Global-local models

Kilic [24, 49] developed a global-local nonlinear modelling approach for ROS composites at the part level. At the local level, the micromechanical unit-cell model generated an effective non-linear response from average responses of two UD layers with axial and transverse fibre orientations. In-plane isotropy assumptions and a weighted average of a matrix-mode layer (transverse or fibres are surrounded by a matrix phase) and a fibre-mode layer (fibres are not shielded by the matrix, and both constituents have the same average strains) were used. At the global level, the developed micromechanical model was implemented within a 3D FE framework using ABAQUS (Figure 2-14.a). The 3D Tsai-Wu failure criterion was used to for damage initiation, and the properties of the fibre unit-cells were set to zero while allowing the elastic and non-linear properties of the matrix unit cells to degrade gradually, to represent the matrix dominant failure initiation and propagation. Although the framework exhibits enormous potential in predicting the overall response of ROS structures, the micro-mechanical model itself was not fully representative of the ROS material and required calibration against the stress-strain curves at the coupon levels specifically the shear behaviour. In another global-local strategy employing external empirical data, Salmi [117] discussed a voxel method combined with a stacking algorithm was adopted for generating RVEs of ROS composites implemented in Digimat software. Using Digimat FE and the orientation tensor for each relevant location (obtained through CT-scans), RVE was generated (Figure 2-14.b) and homogenized properties were computed by means of full field homogenization. Strands and strand interfaces were modelled using solid and cohesive elements respectively. Resin rich zones at the strand ends and strand waviness were accounted for. Limited experimental validations were presented while the model claimed to account for several strand geometric and processing parameters.

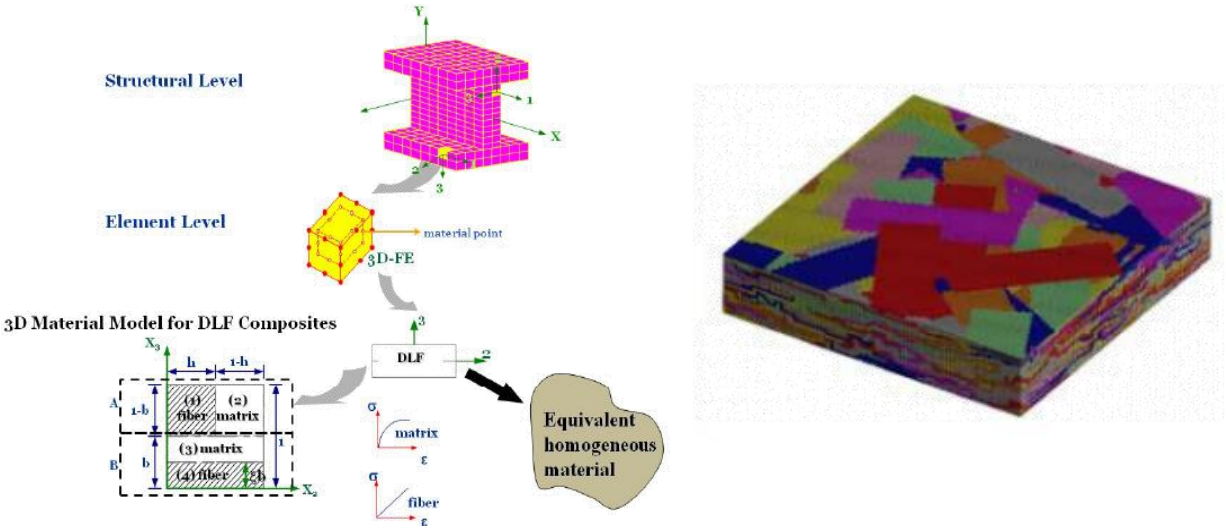

a) b)

Figure 2-14: a) Global-local structural framework by Kilic et al. [58, 59]; b) 3D RVE model incorporated in Digimat [117]

2.4 Literature - Issues to be addressed

Extensive literature survey on ROS architecture and the hybrid architectures of ROS and continuous fibre laminates reveals the following gaps:

a. Works on characterizing the mechanical behaviour of hybrid fibre architectures of randomly oriented strands of carbon/PEEK and continuous fibre tapes of carbon/PEEK do not exist. There is a need to understand the stiffness, strength, and failure characteristics of ROS-hybrids specifically under tensile and interlaminar shear loading at the coupon level, owing to the weaker performance of ROS. Further, the synergistic effects in relevance to hybrid fibre architectures of the same base fibre and matrix systems have not been explored. Thus, there is a strong need for systematic studies on hybrid fibre architectures of ROS and their hybrids at the coupon level.

b. There is a scarcity of predictive modelling techniques for ROS and their hybrids for the calculation of strength and stiffness under in-plane (tensile) and out-of-plane loading

(interlaminar shear), while accounting for the main failure mechanisms and load sharing. Studies on the applicability and validity of several FE models proposed for ROS in relevance to hybrid fibre architectures is questionable. Thus, there is a strong need to understand the mechanical behaviour of ROS-hybrids using simplistic models that capture the crucial failure mechanisms and load sharing.

c. The feasibility of using hybrid fibre architectures on the part level has had limited success. Many defects such as strand waviness and swirling of strands at intersecting junctions of geometric features have not been addressed. The feasibility of manufacturing hybrid fibre architectures of ROS and laminates have not been explored at the part level. Thus, there is a strong need to mitigate the defects and explore the feasibility of using hybrid fibre architectures at the part level.

Thus, the research work presented in this thesis addresses these drawbacks from the literature through the: a) Investigation of the mechanical characteristics of hybrid fibre architectures of ROS and CF at the coupon level, when subjected to tension, and interlaminar shear loading; b) Proposition of predictive modelling techniques for ROS and hybrids for the calculation of strength and stiffness while accounting for the main failure mechanisms and progressive failure; c) Study of the feasibility of using hybrid fibre architectures at part level; minimizing variability and improving performance and processing aspects.

Chapter 3

Coupon Level Studies - Tensile Behaviour

3.1 Experimental Work - Manuscript 2

Tensile Behaviour of Hybrid Fibre Architectures of Randomly Oriented Strands combined with Laminate groups

Abstract

In this work, the tensile behaviour of co-moulded hybrid fibre architectures of randomly oriented strands (carbon/PEEK) combined with laminate groups (Cross-ply, Angle-ply and Quasi-isotropic) is studied. The effects of varying the thickness of the laminate group relative to that of randomly oriented strands, stacking sequence of the architectures within a hybrid specimen, and the ply stacking sequences within the laminate group are quantified. Processing benefits of hybridization such as reduction in warpage and strand waviness are discussed. The tensile

behaviour (tensile stiffness, tensile strength, tensile strain-to-failure, stiffness-to-weight and strength-to-weight ratios) of hybrid fibre architectures is quantified and compared with that of randomly oriented strand specimens, base laminate groups and aluminum 7075. In addition, tensile failure modes have been investigated. Significant improvements in the mechanical properties of randomly oriented strands or a 'reinforcement effect' are observed with small proportions of laminate groups in the specimen. In addition, hybrid fibre architectures exhibit a positive synergy or a positive deviation from the rule-of-mixtures in the overall stiffness and strength behaviour when stacked in specific configurations, despite the same fundamental fibre type and matrix system.

Keywords: Randomly oriented strands, Hybrid fibre architectures, Compression moulding

3.1.1 Introduction

The highly competitive aerospace market drives the need for structural performance, reduction in part mass and costs, and enhancement of processability with fewer post-mould operations. In laminated composites, the fibre architecture governs the design properties and the matrix system provides stable dimensional control to the fibres while contributing to the shear resistance between them. Randomly oriented strand composites (ROS or R) is a fibre architecture comprising of prepreg-based long discontinuous strands of unidirectional tapes or woven fabrics. The industrial potential of ROS composites was exemplified with complex net-shape parts that were competitive with metallic counterparts due to their formability, low-weight and low-cost when manufactured with compression moulding process [6]. Continuous fibre aerospace preforms or tapes (T) exhibiting excellent mechanical performance possess low formability characteristics and are confined to simple shell-like geometries with large curvatures. On the

other hand, discontinuous preforms such as ROS [11, 12] fabricated from compression moulding offer high formability, exhibit stiffness comparable to that of quasi-isotropic (QI) laminates, but possess low tensile strength that inhibits their extensive use in load-bearing aerospace parts (Figure 3-1.a). Thus, a trade-off solution as suggested by various authors [14-21] is to integrate the formability of ROS and performance of continuous fibres (Figure 3-1.a) by using 'hybrid fibre architectures' selectively in part.

The use of hybrid fibre architectures leads to two important effects: a) the reinforcement effect in which the stronger phase at the compromise of its properties enhances the properties of the weaker phase; b) the synergistic effect or the simple deviation from the rule-of-mixture when a hybrid architecture is used. In the literature, the word 'hybridization' in composites refers to the use of two distinct materials characterized by the differences in their strength and elongation [22]. Typically, a high elongation-low strength material has been hybridized with low elongation-high strength material to improve the ductility response of the latter. The behaviour of hybrid systems seldom follows the simple rule-of-mixtures (RoM) approach and usually exhibits a synergistic relationship called the 'hybrid effect' with interlayer stacking arrangements. Further, this effect is described as either positive or a negative deviation from the theoretical RoM [23]. The review article [22] summarizes the works on hybridization and attributes the synergistic behaviour to the damage development, residual stresses and stress concentrations in hybrids.

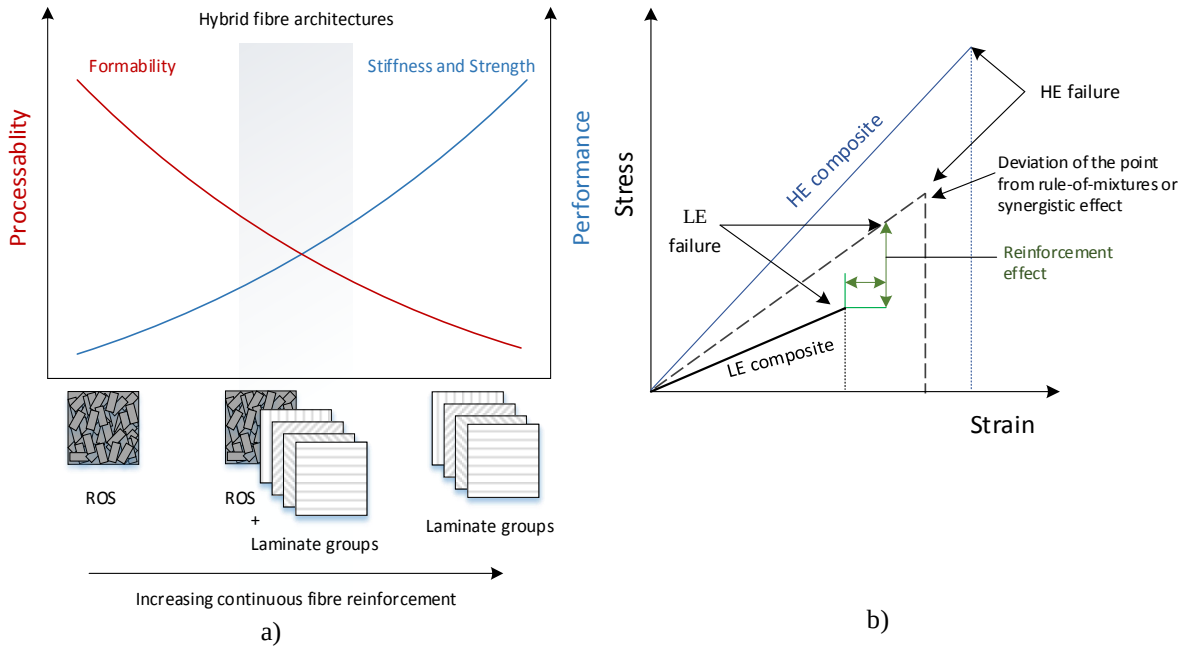

Figure 3-1: a) Composite material systems: performance and processing; b) Hybridization of High Elongation (HE) and Low Elongation (LE) composites showing the reinforcement effect and the synergistic effect

Researchers have reported significant improvements in the properties of discontinuous fibre composites when hybridized with continuous fibres such as unidirectional tapes/woven fabrics of either the same/different material systems. For instance, Lee et al. [70] reported low scatter of the tensile strength and higher transverse strength in short random fibre mat when hybridized with interlayers of continuous fibres. Brooks et al. [118] studied the damage development in a compression moulded fabric/glass mat hybrid and reported an increase of 53% in modulus and 30% in maximum load in hybrids over the glass mat. In a series of experimental works, Selmy et al. [71-73] examined hybrid configurations of unidirectional and random glass fibre/epoxy systems. The properties were improved when tapes were placed in the middle vs. the surface of the composite thus showing that the tensile behaviour was altered by the stacking arrangement. The measured tensile modulus agreed well with the theoretical modulus computed using RoM. Han et al. [33] showed improvements in the bearing strength with ROS/5-harness satin fabric

hybrid. Taketa et al. [119] studied interplied carbon fibre reinforced polypropylene between self-reinforced polypropylene layers and reported improvements in the ductility characteristics. A positive hybrid effect of +7% to +18% was reported on the strain-to-failure characteristics. The modulus and strength behaviour were noted to be lower than the RoM predictions and were attributed to the waviness of carbon fibres caused by the self-reinforced polypropylene shrinkage during consolidation. In a study [120] on achieving pseudo-ductile behaviour of interlaminated hybrids with discontinuous carbon fibres and continuous glass fibres, a bilinear RoM behaviour of the hybrids was observed.

The focus of the current work is to explore the tensile behaviour, to assess the reinforcement effect (Figure 3-1.b) (the improvement in properties of the ROS phase in a hybrid fibre architecture) and to quantify the extent of synergy in co-moulded hybrid fibre architectures of ROS and laminate groups of carbon/PEEK (the deviation from the rule-of-mixtures). The problem investigated here is that of a low elongation-low strength material (i.e. ROS) hybridized with a higher strength-higher elongation material (i.e. continuous fibre laminates) of the same fibre type and matrix system.

3.1.2 Experimental Work

Selection of test configurations

Parameters that govern the performance of ROS at the micro-level include length-to-diameter ratio of the fibre, fibre volume fraction, modulus and strength of fibre and matrix. At the macro-level, the governing parameters include strand orientation distribution, strand length distribution, overlap lengths, strand aspect ratio, voids and resin rich areas. Further, the initial placement of

strands, the strand flow and the specimen thickness would affect the strand out-of-plane orientations within the ROS part. Carbon/PEEK material of known physical properties was chosen (fibre volume fraction = 59%) to standardize the resin system and the fibre length-to-diameter ratio. A fixed strand size (length x width): 25 mm x 12 mm was chosen.

The choice of the test configurations was driven by four aspects: Laminate group, thickness ratio ($t_{laminate}/t_R$), total thickness of the hybrid specimen, and stacking configurations of the phases within a hybrid specimen. Three sets of generic laminate groups from tapes were chosen for hybridization with ROS: Cross-Ply (CP), Quasi-isotropic (QI), Angle-ply (AP). These laminates were characterized by differences in strengths, stiffness and strain-to-failure relative to that of ROS (Figure 3-2.a). The thickness ratio governs the extensional stiffness of the phases, load sharing and progression of failure within a hybrid specimen. Three thickness ratios were chosen such that the extensional stiffness ($EA_{laminate}$=Effective elastic modulus x cross-sectional area of the laminate) equaled /lower /higher than that of the ROS phase. To achieve these ratios, three thicknesses were chosen for the hybrid specimens. The thickness of the ROS phase was varied to achieve the desired thickness ratios, while the laminate group thickness was maintained a constant across hybrid specimens of one set. Three stacking configurations in a hybrid specimen (T-R-T, R-T-R, and T-R) were chosen (Figure 3-2.b) to study the effect of stacking on properties, failure propagation and processing. The test configurations (Table 3-1) were thus selected based on the potential applications, load sharing ratios, ply thicknesses, material availability and processability.

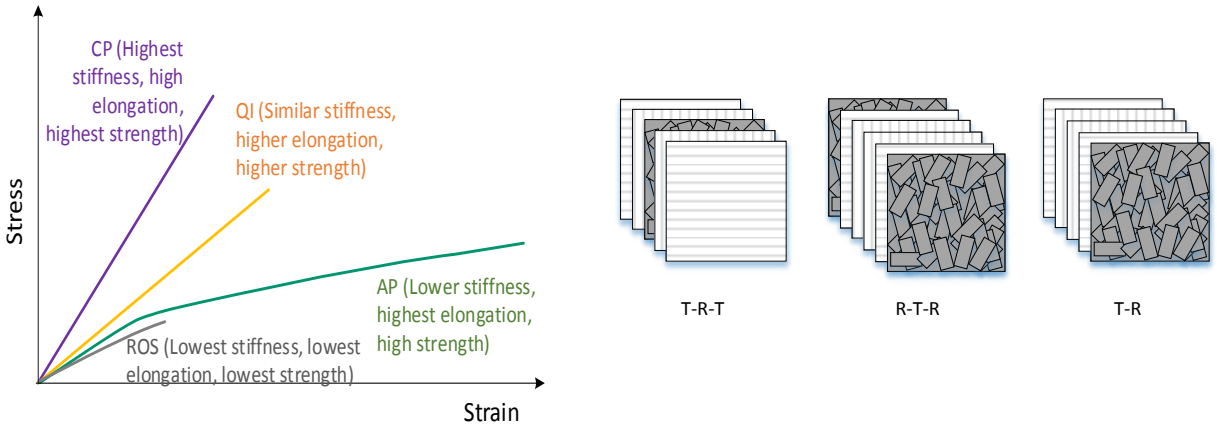

a) b)

Figure 3-2: a) Illustration of stress-strain curves of ROS and laminate groups chosen for hybridization (All comparisons are with reference to ROS); b) Stacking configurations for hybridization exemplified with CP-R hybrids (Note: Thickness ratios are not represented in the illustration)

Configuration	**Stacking**	$\mathbf{t_{laminate}/t_R}$	**Specimen thickness (mm)**
R (base)			2, 3, 4
Base laminate groups	CP ($[0/90/0/90]_{2s}$)		
	QI ($[45/0/-45/90]_{2s}$)		
	AP ($[45/-45]_{2s}$)		
CP-R	T-R-T	15/85, 20/80, 30/70	4, 3, 2
	R-T-R	15/85, 20/80, 30/70	4, 3, 2
	T-R	15/85, 20/80, 30/70	4, 3, 2
QI-R	T-R-T	40/60	3
	R-T-R	40/60	3
	T-R	40/60	3
AP-R	T-R-T	30/70	1.8

Table 3-1: Base ROS, laminate groups and hybrid test configurations

Panel manufacturing and test setup

Strands were placed in small batches into a steel mould of 300 mm x 355 mm and shuffled back-and-forth each time to minimize their initial out-of-plane orientations (Figure 3-3.a). The mould

was placed in a press and minimal pressure was applied to close it. Based on the processing guidelines [12, 121] and trials, the maximum processing pressure and temperature were fixed at 60 bars and 400°C respectively. A full pressure of 60 bars was applied at 400°C (Figure 3-3.b). Following a 20 min dwell, the mould was cooled down at an average rate of 10°C/min. For the hybrid configurations, ROS and laminates were placed in the mould at the same time and co-moulded. The panel was then de-moulded, trimmed and machined into test coupons. For consistency, the same moulding cycle was used for manufacturing of all panels.

Tensile tests were performed as per ASTM D3039 [122], on at least five specimens per configuration. A Digital Image Correlation (DIC) technique was used to obtain the average strain field over the width of the specimen. For the DIC, a 5-megapixel camera with AF75-300 mm Tamron lens was used to capture images at 5 Hz. Specimens were loaded at 2 mm/min. Image analysis was performed using VIC-2D software from Correlated Solutions. A subset size of 35 pixels and a step size of 15 pixels, which correlated to about 3 mm and 1 mm on the specimen respectively, as a coarse averaged out strain-field appropriate for the measurement of a global modulus of heterogeneous material such as ROS was intended [12]. The longitudinal modulus was computed by finding the slope of the stress-strain curve in the strain interval of 1000 – 3000 με.

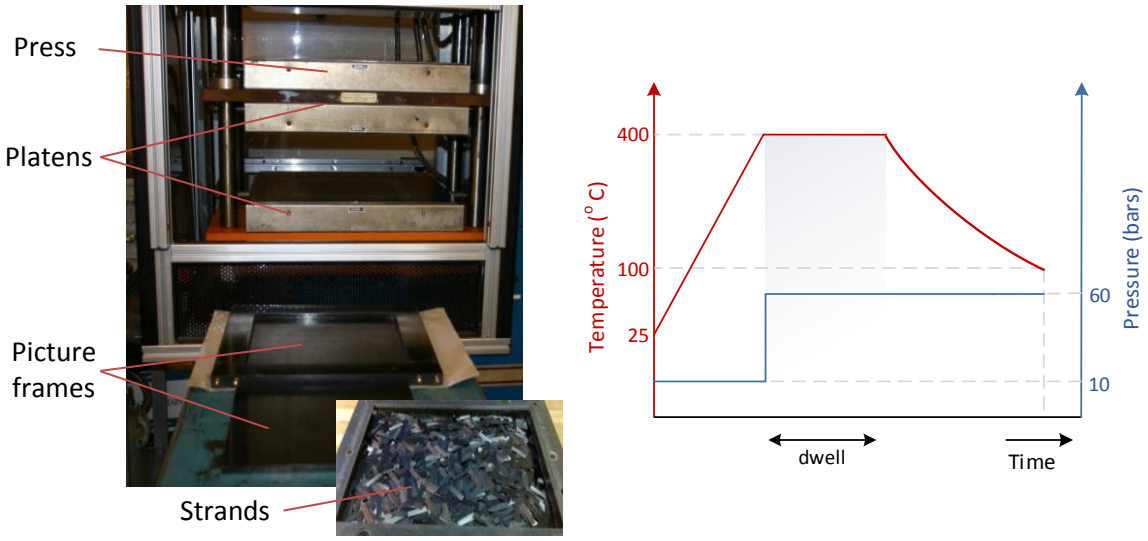

a) b)

Figure 3-3: a) Manufacturing set-up; b) Processing conditions (temperature, pressure and time. Not to scale)

3.1.3 Results and discussions

The results are grouped into three sections: processing observations, mechanical behaviour and the synergistic effect due to hybridization.

Processing observations

Warpage in ROS based panels (ROS and hybrids) is caused by the heterogenous microstructure (i.e. strand orientations results in variable local modulus and thermal expansion coefficients) and the processing conditions (e.g. part–tool interaction, temperature gradients). From the literature, methods to quantify warpage in continuously distorted panels are scarce and of low practical significance. Selezneva et al. [12] used the deviation of ROS panels from the plane-of-best-fit as a measure of warpage. In this work, we quantify warpage using a parameter called the 'Flat Area Fraction' (FAF) which is the ratio of the usable flat area to the total panel area. Usable flat area is

the maximum flat area in a warped panel that satisfies a chosen flatness tolerance. To obtain the usable flat area, the distortion profiles of ROS and ROS-hybrid panels were measured using a co-ordinate measurement machine at every point spaced 25 mm on the panel, to form the warpage profile (Figure 3-4.a). Starting at each of these points, the deviations of the point and its neighbouring points were compared against a chosen flatness tolerance. The maximum usable area for that flatness tolerance was then mapped (Figure 3-4.b) and FAF was calculated. Practically, this area defines the boundaries of the maximum flat region that can be machined from a continuously distorted panel. FAF comparisons for various panels (Figure 3-4.c) indicated that thicker ROS panels exhibited lower warpage or a higher FAF at lower flatness tolerances. Similar observations were reported in [12] and the decrease in warpage in thicker panels was attributed to the increased homogeneity in the microstructure. Additionally, the flexural rigidity of the specimens increases with the thickness and could contribute to the decreased warpage. Further, the FAF increased with hybridization and with the increase of symmetric and balanced layups. QI-R panels with T-R-T configuration exhibit the least warpage. Hybridization of ROS panels showed a reduction of the warpage characteristics for the same thickness thus indicating the benefits of hybridization. It is to be noted that the panels have varying curvature and interpreting them is not easy. In the current research understanding the warpage characteristics is not the primary goal. Thus, warpage values are just reported.

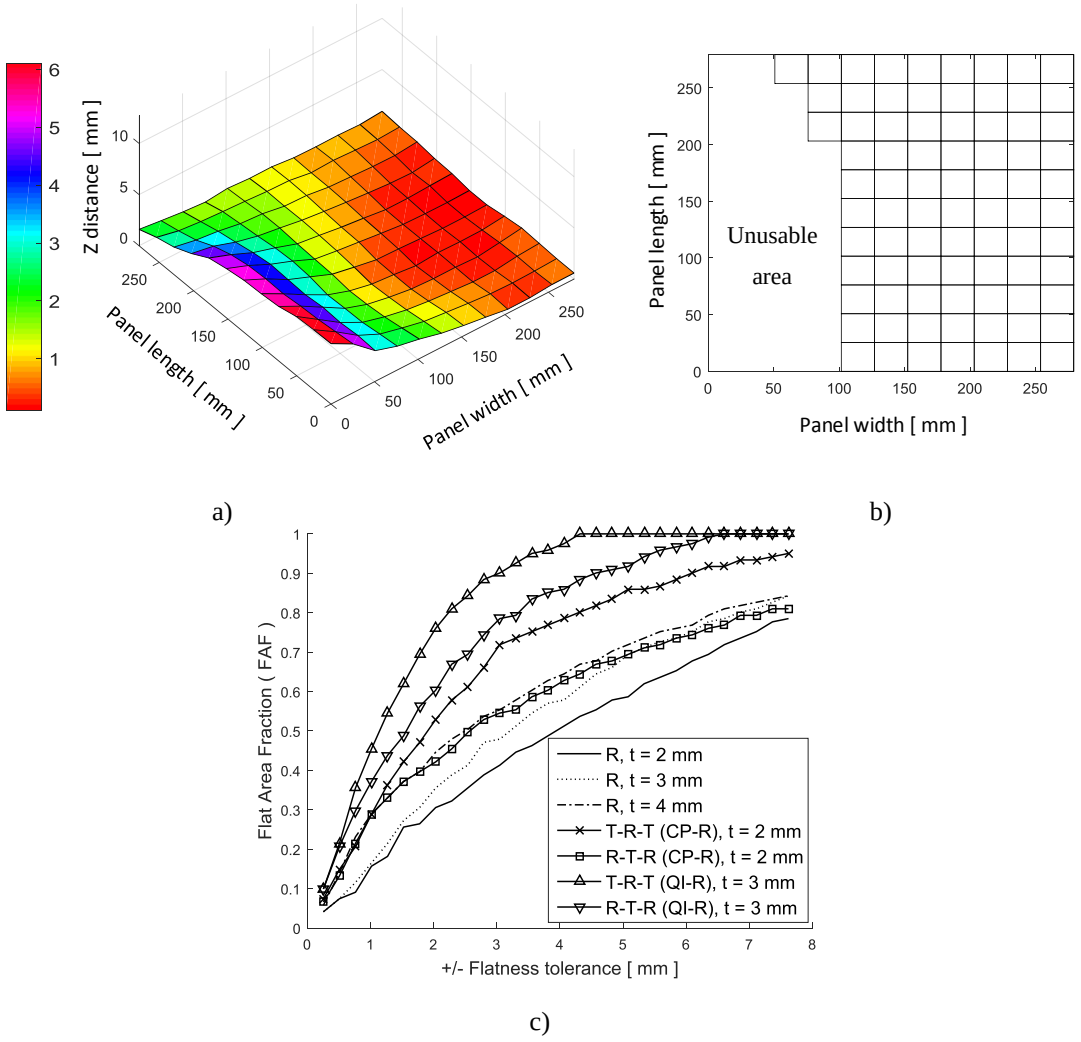

Figure 3-4 : a) Warpage profile of a panel; b) Usable flat area with FAF=67% for a flatness tolerance of +0.9 mm; c) FAF vs. Flatness tolerance for ROS and their hybrids

Other processing effect prominently observed was the strand out-of-plane waviness. Strand waviness or undulations result in interlaminar normal and shear stresses [123] in the out-of-plane directions causing premature failure of the specimens. An important observation from current work and from [12] was that thick ROS panels exhibit more homogeneity of strands due to the dispersion of the strands through the thickness and was accompanied by lower strand out-of-plane orientations. The strand out-of-plane waviness seems to be majorly governed by two

factors: initial strand placement and the resistance offered to the squeeze flow by the layer in contact with the tool. Figure 3-5 shows the micrographs of R, T-R-T, R-T-R and T-R configurations for CP-R hybrids with panel thickness of 4 mm and a thickness ratio of 15/85. Specific stacking configurations of hybrid panels (for instance, T-R-T configuration) exhibit the least strand out-of-plane waviness. This can be attributed to the 0-degree and 90-degree tapes that act as accommodating plies that offer low resistance to the squeeze flow of strands during consolidation. In all the R-T-R configurations, the laminate group that is sandwiched between ROS exhibits out-of-plane waviness. Using microscopic cross-sectional images of multiple specimens and image thresholding analysis using ImageJ software (a proprietary image processing software from Correlated Solutions Inc.), the total noticeable resin rich areas were in the range of 1-2% while the void content was on the order of 0.3% indicating good compaction while the interface of ROS and laminate groups were free of any noticeable defects.

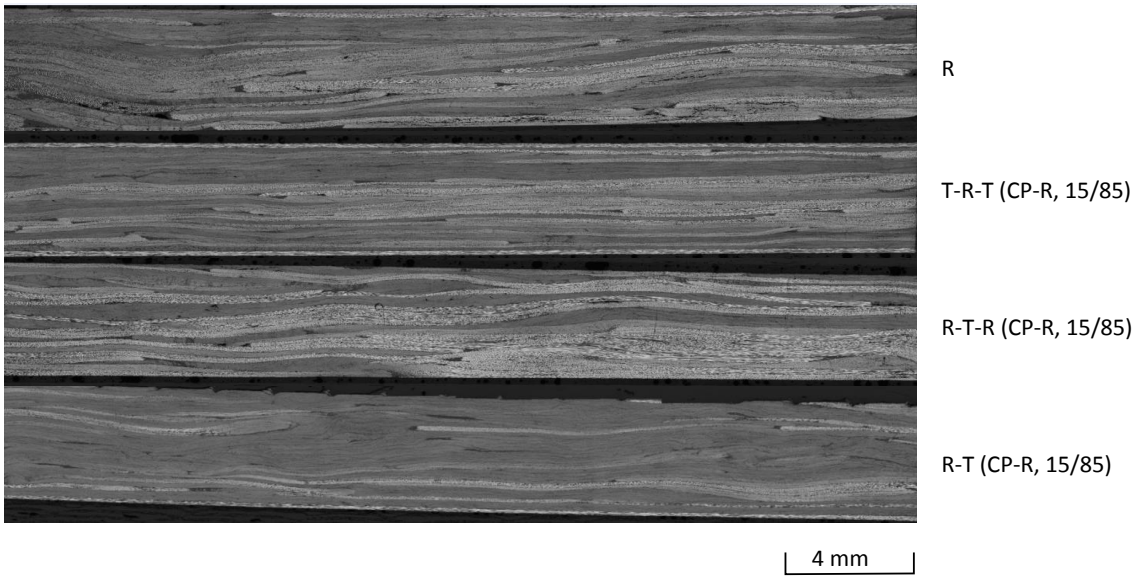

Figure 3-5 : Micrographs of R, T-R-T, R-T-R, and R-T or T-R configurations of CP-R hybrid, for panel thickness of 4 mm

Mechanical behaviour – Tensile properties

Tensile stress vs. strain behaviour

Representative longitudinal stress vs. longitudinal strain curves for ROS, cross-ply and cross-ply-ROS-hybrids (Tapes-ROS-Tapes hybrid stacking) are normalized with ROS properties and depicted in Figure 3-6. The typical behaviour of the stress-strain curve for ROS is mostly linear except for the last 10% of the strain when the curves usually tend to be non-linear. This is attributable to the rapid progression of failure due to sliding or pull-out of strands. Among the base laminate groups, cross-ply has the highest stiffness and strength and determines the upper bound. The stiffness of all the hybrid configurations lies between the ROS and base laminates.

Three key observations on hybrid configurations can be made from Figure 3-6. The first observation is related to the change in the longitudinal stiffness of the hybrids. An increase in the laminate thickness ($t_{laminate}$) in a hybrid specimen relative to the ROS thickness is expected to increase the longitudinal stiffness of the specimen. However, as the $t_{laminate}$ increases from 15% to 20%, the stiffness of the hybrid drops slightly. Further, as the laminate thickness increases from 20% to 30%, the stiffness of the hybrid increases again and tends towards the stiffness of a cross-ply laminate. This behaviour can be attributed to the thickness of the ROS phase in the hybrid specimen. Due to fabrication restrictions, the laminate thickness was constant among all the cross-ply-ROS-hybrids, while the thickness of the ROS phase was varied to obtain various thickness ratios. The thickness of ROS phase was the highest in the 15/85 configuration (3.45 mm), followed by the 20/80 configuration (2.45 mm) and lowest in the 30/70 configuration (1.45 mm). It was noted in this research and from literature [11, 12] that thick ROS panels demonstrate better performance and a reduction in overall strand waviness. Thus, 20/80 specimens exhibit

lower stiffness compared to 15/85 specimens owing to the thickness of the ROS phase in them. Despite the lowest thickness or highest strand waviness in the ROS phase in 30/70 specimens (1.45 mm), the extensional stiffness of the laminate group dominates the stiffness behaviour and enhances the overall stiffness and strength of the hybrid.

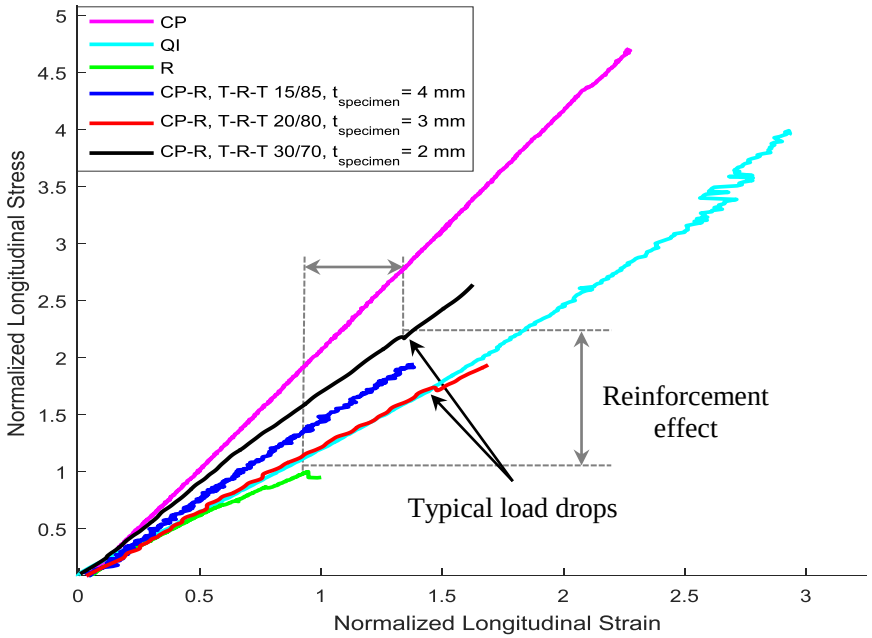

Figure 3-6: Typical stress vs. strain curves of ROS, cross-ply, quasi-isotropic and cross-ply-ROS Tapes-ROS-Tapes hybrids for thickness ratios ($t_{laminate}/t_R$) of 15/85, 20/80, 30/70 (strains are average strains from DIC data)

The second observation is the presence of load drops in the stress-strain curves of the 20/80 and 30/70 hybrid configurations. Load drops are attributable to the ratio of extensional stiffness between the phases, which is explained using the illustration in Figure 3-7. In a hybrid specimen, the axial load is distributed in the architectures proportional to their extensional stiffness. The extensional stiffness of ROS (EA_R) depends on the thickness of the phase and the orientations of the strands within. ROS phase is a weaker architecture with lower strength-to-failure and lower strain-to-failure compared to the laminate group and fails prior to the laminate group. As soon as the ROS phase in a hybrid specimen fails, the load must be transferred to the laminate group

until the complete failure of the specimen. The 15/85 hybrid is a ROS dominant configuration as the extensional stiffness ratio ($EA_{laminate}$ / EA_R) is about 25:75, thus a higher load share in the ROS. With the failure of the ROS phase, the laminate group experiences high loads and fails instantly as the thickness ratio and the stiffness ratio of the laminate group are low compared to ROS (Point A in Figure 3-7). Thus, the stress-strain curves of 15/85 configuration showed no signs of load drop in four of five specimens (Figure 3-6). With an extensional stiffness ratio of about 40:60, the 20/80 configuration is also a ROS dominant configuration (Point B in Figure 3-7). Three of five specimens demonstrated a load drop signifying failure of ROS (Figure 3-6), while the remainder of the loads was carried by the laminate group until final failure due to its considerable proportions in the hybrid. The stress-strain curves for the 30/70 configuration represents a laminate group dominated behaviour with the extensional stiffness of about 55:45 (Point C in Figure 3-7). Four of five specimens demonstrated noticeable load drops with T-R-T configurations (Figure 3-6). Theoretically, the point representing equal extensional stiffness of the ROS and the laminate group can be regarded as the transition between ROS-dominated and laminate-dominated behaviour.

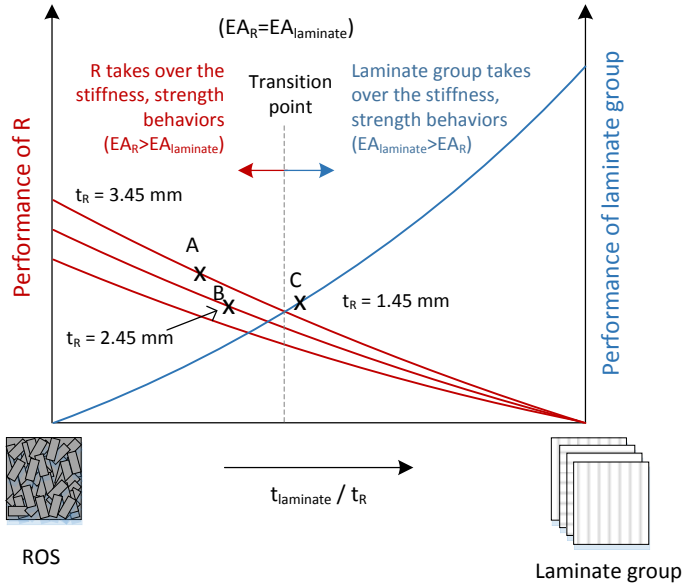

Figure 3-7: Illustration of the hybrid behaviour as a function of absolute thickness of ROS and extensional stiffness of the phases (qualitative representation only, not to scale)

The third observation is the position of the load drop on the stress-strain curve of a hybrid configuration (Figure 3-6). The load drops signify significant failure of the ROS phase, as no other noticeable laminate failures were observed at these drops. When the stresses and strains corresponding to the load drops of the hybrid configurations are compared with that of ROS, there are noticeable strength enhancements to the ROS phase of ~2 times for the 30/70 and ~1.5 times for the 20/80 configuration. These enhancements are due to the 'reinforcement effect' that can be attributed to the load sharing ability of the laminate phase by 'fibre bridging' after local damages in the ROS phase, explained in subsequent sections. The bridging offered by the laminate group is proportional to the laminate stiffness. Thus, the 30/70 hybrid configuration has a higher strength at the load drop compared to the load drop in the 20/80 configuration. The stress-strain curves of the R-T-R and the T-R configurations were similar to that of T-R-T configuration. It is interesting to note that the strains at the load drops for all the hybrids are

around ~1.3-1.5 times the failure strains of ROS specimens. Such an attribute indicates the failure of ROS phase and could assist in the design of parts using ROS-hybrids.

The stiffness of the QI-R hybrids was similar to quasi-isotropic laminate stiffness as the stiffness of ROS was similar to that of quasi-isotropic laminates as indicated in Figure 3-6Figure 3-8. However, the stress-strain curves for the QI-R configuration representing a thickness ratio of 40/60 did not reveal any noticeable load drops despite an extensional stiffness ratio of about 55:45. This could be due to the gradual load transfer/redistribution within the hybrid specimen due to the presence of 45-degree plies in the quasi-isotropic laminate. The angle-ply laminate has the highest strain-to-failure (about 160000 με) and the stress vs. strain curve is highly non-linear. An angle-ply laminate is more representative of a $[\pm 45]_{ns}$ shear test used to obtain shear modulus, shear strain and shear strength. When ROS was hybridized with an angle-ply laminate, the behaviour of the hybrid was no longer shear dominated. Hence, the strain-to-failure of AP-R hybrids is improved moderately. The comparisons of the strength, stiffness and strain-to-failure is shown in subsequent sections.

Tensile modulus

The longitudinal stiffness (E_{xx}) of all the test configurations are normalized with the mean modulus (E_{ROS}) of ROS specimens and illustrated using the box-plots in Figure 3-8. The upper limit on the box-plot represents the max value of the sample set, and the lower limit represents the lowest value. The upper bound on the box represents the 75^{th} quartile while the lower bound represents the 25^{th} quartile. The mid-line of the box represents the median of the sample set. From the comparison, ROS stiffness values are accompanied by a considerable variability and

the mean modulus is ~80% of a quasi-isotropic laminate and ~50% of aluminum 7075. Among the cross-ply-ROS-hybrid configuration, the T-R-T stacking exhibits the least variability followed by R-T-R and T-R. In all the stacking configurations of 15/85 cross-ply-ROS-hybrids, the mean stiffness improvements are either higher than or comparable with that of quasi-isotropic laminates. In the 20/80 configurations, the stiffness values recorded were lower than the 15/85 although the tape proportions were higher, due to reasons discussed earlier. No major noticeable differences in the stiffness characteristics were observed when the ply layup in the T-R-T configuration was changed from [0/90/R/90/0] to [90/0/R/90/0] (represented by the Ti-R-Ti) and the differences in properties were within the experimental accuracies. The 30/70 cross-ply-ROS-hybrid with T-R-T stacking exhibits highest stiffness improvements of ~50%. For the QI-R hybrids, the mean stiffness values of all the three stacking configurations are in the same range as that of a quasi-isotropic laminate. The stiffness of the AP-R configurations shows stiffness values comparable with ROS, owing to the low extensional stiffness of angle-ply laminates. It is to be noted that only five specimens for each configuration were tested due to the material availability and processing limitations. Although this pilot study suggests improvement potential based on the phenomenological behaviour, a higher number of specimens are needed for statistically conclusive results. The B-basis [35] values that represent the conservative knockdowns of design allowables based on the number of test specimens, are thus indicated under the box-plots with solid lines.

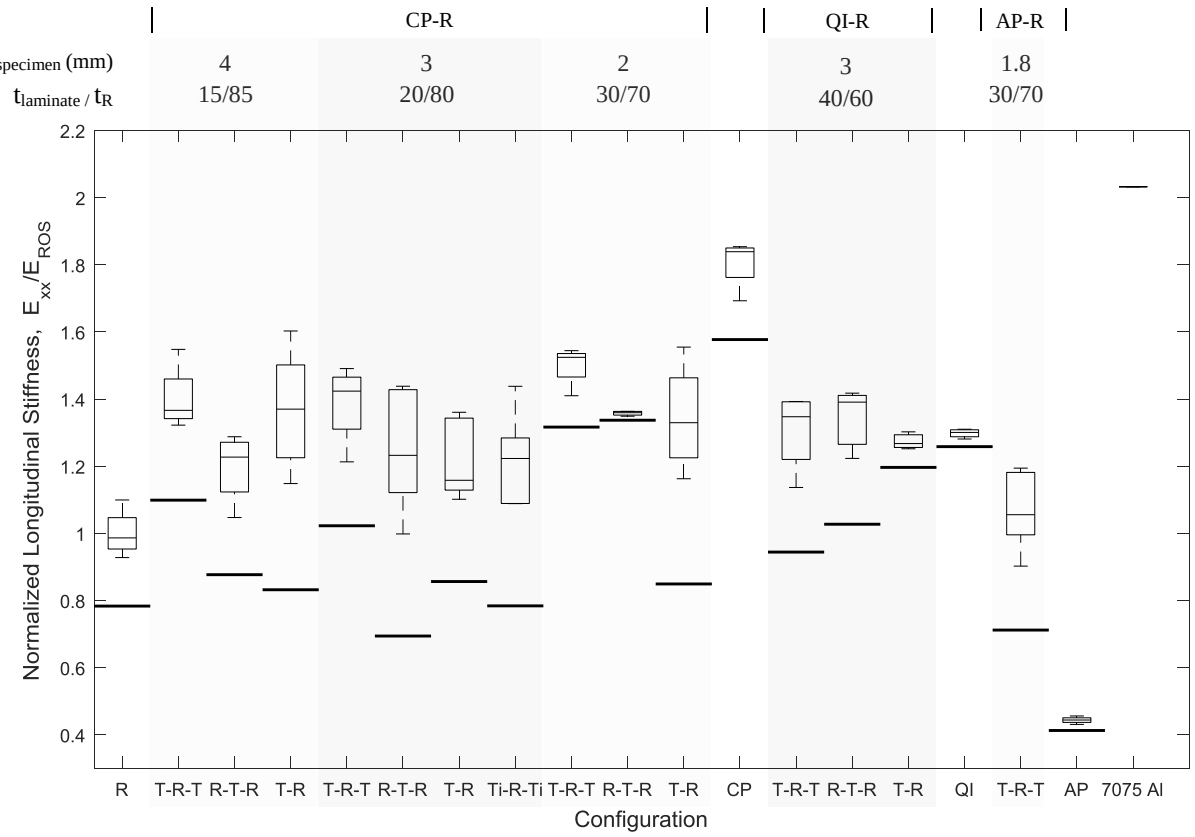

Figure 3-8: Normalized longitudinal stiffness data of the test configurations

Tensile strength and strain-to-failure

The tensile strength of ROS (σ_{ROS}) is ~25% the tensile strength (σ_{xx}) of a quasi-isotropic laminate (Figure 3-9). Hybridization has significant improvements on the tensile strength properties. With the cross-ply-ROS 15/85 hybrid configuration, the tensile strength doubles with the T-R-T stacking, increases by ~1.5 times for the R-T-R, and by ~1.8 times for the T-R stacking. The properties of 30/70 cross-ply-ROS-hybrids are comparable to the yield strengths of aluminum. An increase in strain-to-failure of the hybrid specimens is observed with an increase in the percentage of laminate groups (Figure 3-10), hence the enhancement of strain-to-failure could be considered as a secondary benefit. Overall, strain-to-failure enhancements as high as 60% are observed for the T-R-T configurations for CP-R, QI-R and AP-R hybrids. The symbols

ε_{xx} and ε_{ROS} corresponds to the longitudinal strain and the mean longitudinal strain of the ROS specimens, respectively.

Among all the hybrid configurations, properties of T-R-T stacking exhibited higher properties, followed by T-R and R-T-R stacking. This can be attributed to two factors: reduced out-of-plane strand waviness in T-R-T (Figure 3-5) and a better dispersion of the tapes from the mid-plane of the panel, thus minimizing the influence of in-plane–bending coupling terms. R-T-R stacking exhibit the lowest properties and larger variability compared to T-R-T. From the standpoint of the material distribution, the randomness in the R-T-R is split into two sub-thicknesses and dispersed on either side of a centrally placed wavy laminate group. The T-R stacking offers slightly better properties compared to the R-T-R stacking. The micrographs (Figure 3-5) of T-R show that the laminate group reduces the strand out-of-plane waviness towards their vicinity. Further, T-R represents an unsymmetrical configuration and introduces eccentricities in loading after the failure of the ROS phase. Hence, the properties of T-R are lower compared to the T-R-T configuration and slightly better than R-T-R. Hybrid fibre architectures provide numerous design choices; the design decisions should be made based on the design requirements such as the presence of secondary loads, stiffness-to-weight, strength-to-weight ratios and manufacturing feasibility. For instance, a 30% cross-ply laminate in a 2 mm hybrid produces much higher strengths than a 40% quasi-isotropic laminate in a 3 mm specimen. A hybrid with 20% cross-ply laminate exhibits comparable strengths with a hybrid comprising of 40% quasi-isotropic laminate, both with 3 mm thickness. Hence, when designing a structure requiring thin features for low-weight reasons, a CP-R hybrid can be employed instead of a QI-R hybrid provided the hybrid stacking is achievable.

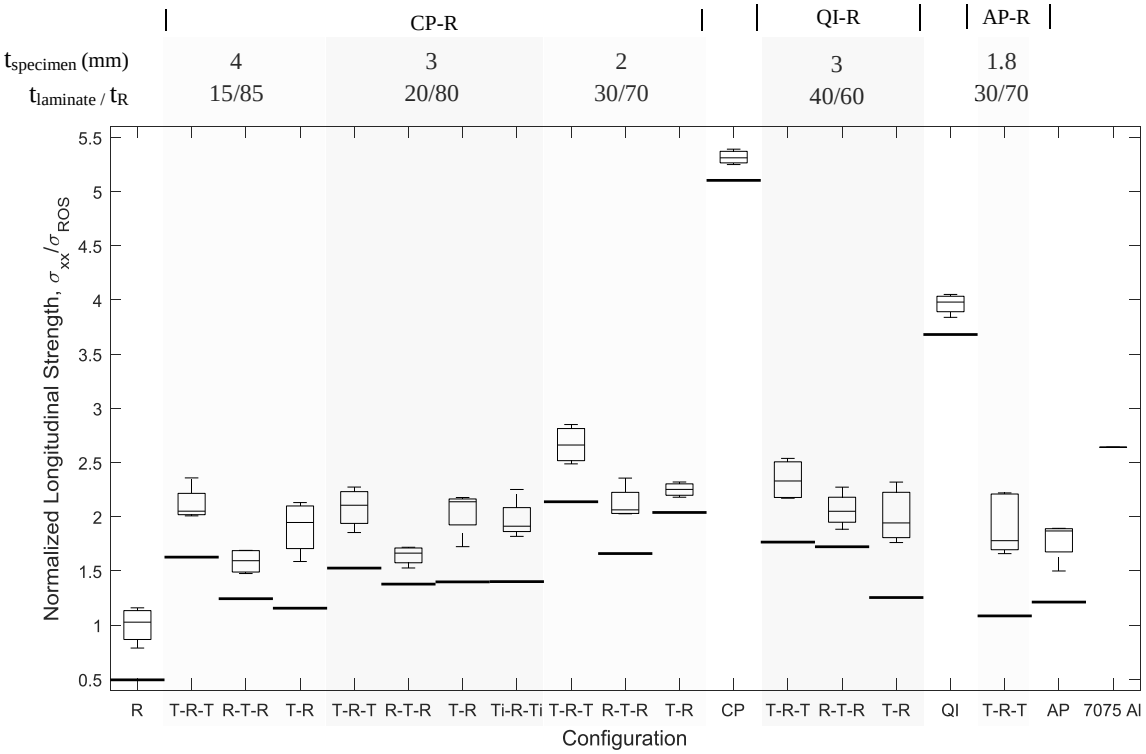

Figure 3-9: Normalized longitudinal strength data of the test configurations

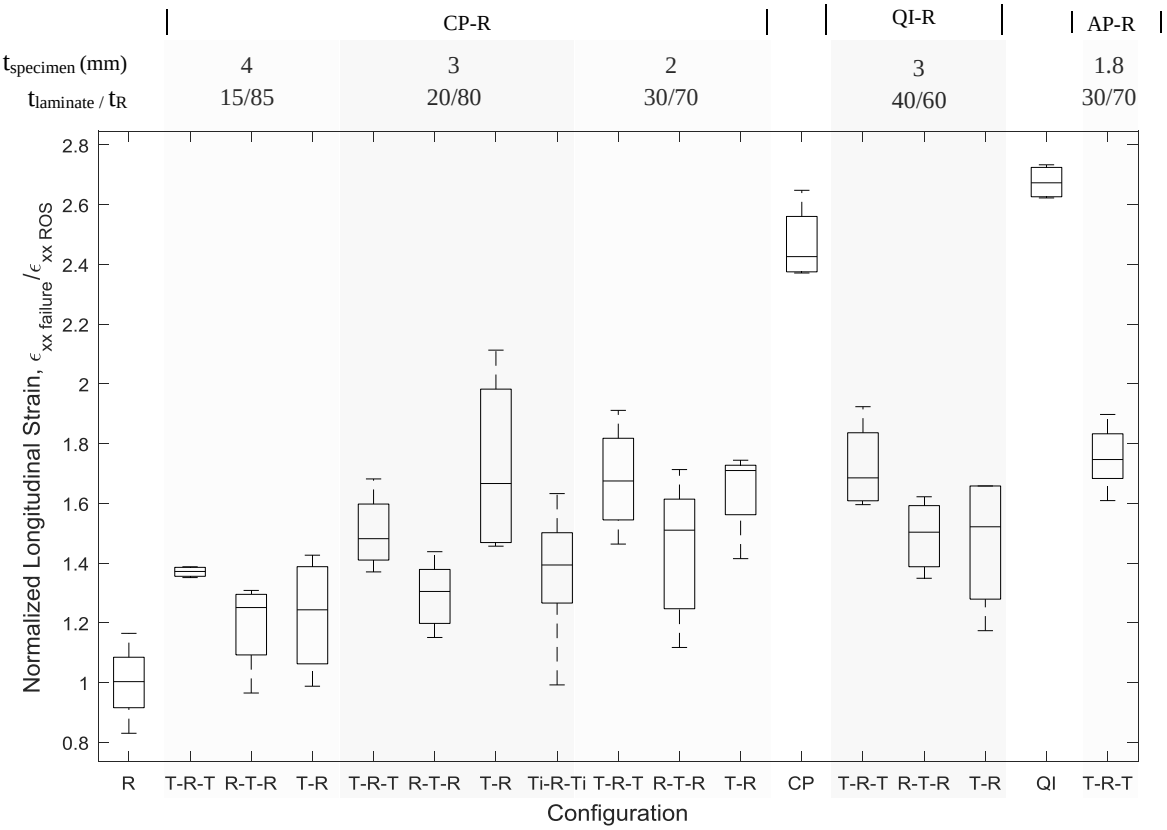

Figure 3-10: Normalized longitudinal strain-to-failure data of the test configurations

Tensile fracture characteristics

Firstly, the failure characteristics in ROS are discussed. The DIC images of the progression of failure in ROS specimens are shown in Figure 3-11.a while Figure 3-11.b depicts the strain variations in ROS-hybrids captured just before failure. Multiple high strain regions were noticed on the ROS specimens, a dominant effect of the heterogenous meso-structure. One of these regions developed predominantly across the specimen causing the final failure. In ROS specimens, some of the high strain regions corresponded to the multiple failure initiations. Over the course of the loading, the region of maximum strains shifted within the specimen. This effect could be attributed to the staggered pattern of ROS phase that alters the strains by arresting the failure propagation. ROS specimens demonstrated a combination of fibre fracture and strand pull-out or delamination [98] in three of the five specimens tested (Figure 3-12.a). Long extensive failure paths were accompanied with fibre pull-out failures. The strands oriented at acute angles to the direction of the loading axis seemed to have failed in fibre fracture. Two ROS specimens failed prematurely and exhibited less fibre pull-out and more an abrupt failure (Figure 3-12.b). A careful observation revealed noticeable out-of-plane strand waviness at those failure locations.

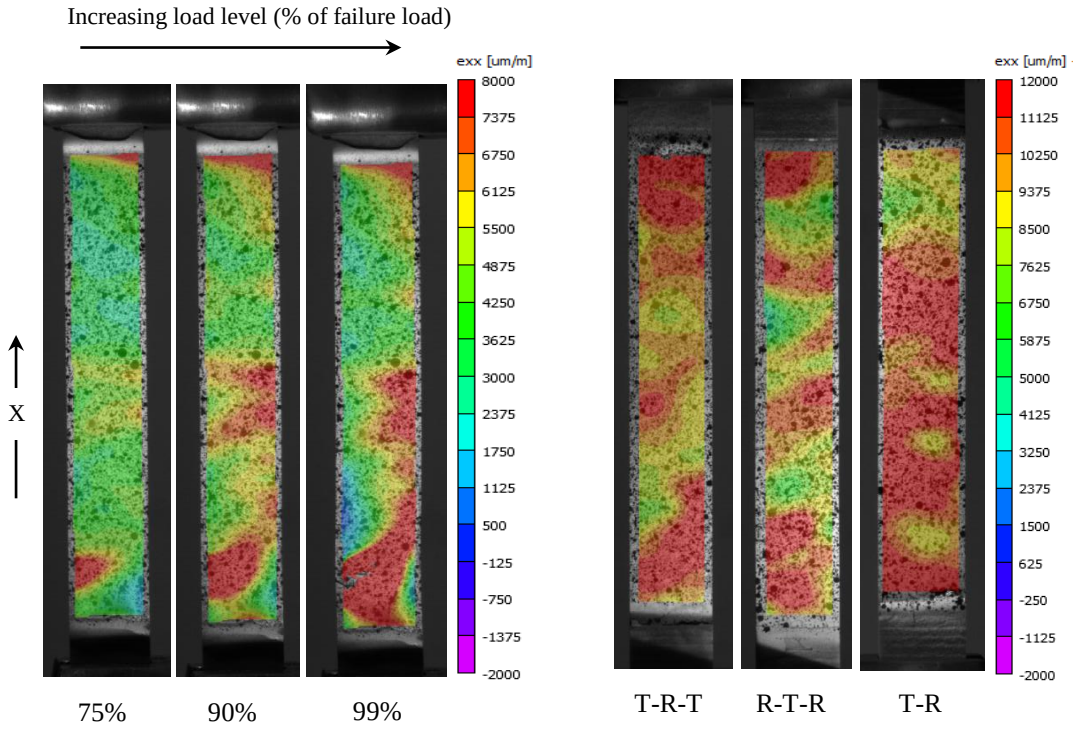

Figure 3-11: a) DIC images depicting the progression of longitudinal strain fields in a ROS specimen with increasing load levels; b) DIC images of hybrid specimens just before failure

The failure in the T-R-T configuration for various thickness ratios is discussed first. When the thickness ratio was 15/85, fibre fracture was dominant, and the extent of the failure was short. Severe damage at more than one location was seen in three specimens, indicating an effect of multiple failure initiations in the ROS dominated configuration. With the increase in the thickness ratio of the laminate group to 20/80, the load distribution changed; a mix of strand pull-out and fibre fracture was observed. Specimens showed longer failure paths (Figure 3-12.c) and multiple failures compared to that of the 15/85 configuration. Two of five specimens tested had more than one severe damage location. With the 30/70 configuration, more net failures were observed in most specimens, while the strand pull-out seemed to be a secondary effect. It is to be

noted that premature failures were caused due to the strand waviness (Figure 3-12.d), despite the configurations. Premature failure is relative to the specimens that failed at a high load. For example, if one of the ROS specimens failed at a low load, and when we observe the failure, a significant strand waviness is seen. The failure patterns are abrupt signifying that the waviness has a huge impact on the strength. Thus, the failure load in the specimen would have reached a higher load had the strand waviness were minimal. The evidence of the failures due to waviness are shown in the images. Multiple locations of high strains are observed in the DIC images of hybrids, much more than those of ROS specimens (Figure 3-11.b). This can be attributed to the redistribution of the loads between various regions of ROS due to fibre bridging.

In R-T-R configurations, more strand pull-out and longer failure paths (Figure 3-12.e) were observed when compared to the T-R-T stacking. Almost all the configurations with R-T-R were characterized by the presence of delamination at the interface of ROS and the centrally placed wavy laminate group (Figure 3-12.f). In R-T-R, as the ROS phase fails at low strains, the wavy tapes start bearing the loads and start to stretch. Since some parts of ROS are still in contact with the tapes, the interface starts delaminating thus causing extensive failures. All the R-T-R stacking configurations exhibited similar failure characteristics despite changes in the thickness ratios. The T-R configurations demonstrated random failure characteristics. QI-R hybrids exhibited long failure paths that could be attributed to the higher strain-to-failure of the quasi-isotropic laminate that extends beyond the failure of the ROS phase. AP-R also demonstrated long failure paths/fibre pull-out in the ROS phase and matrix separation in the 45-degree plies explaining the lack of contribution from the angle-ply towards the strain enhancement of the AP-R hybrid.

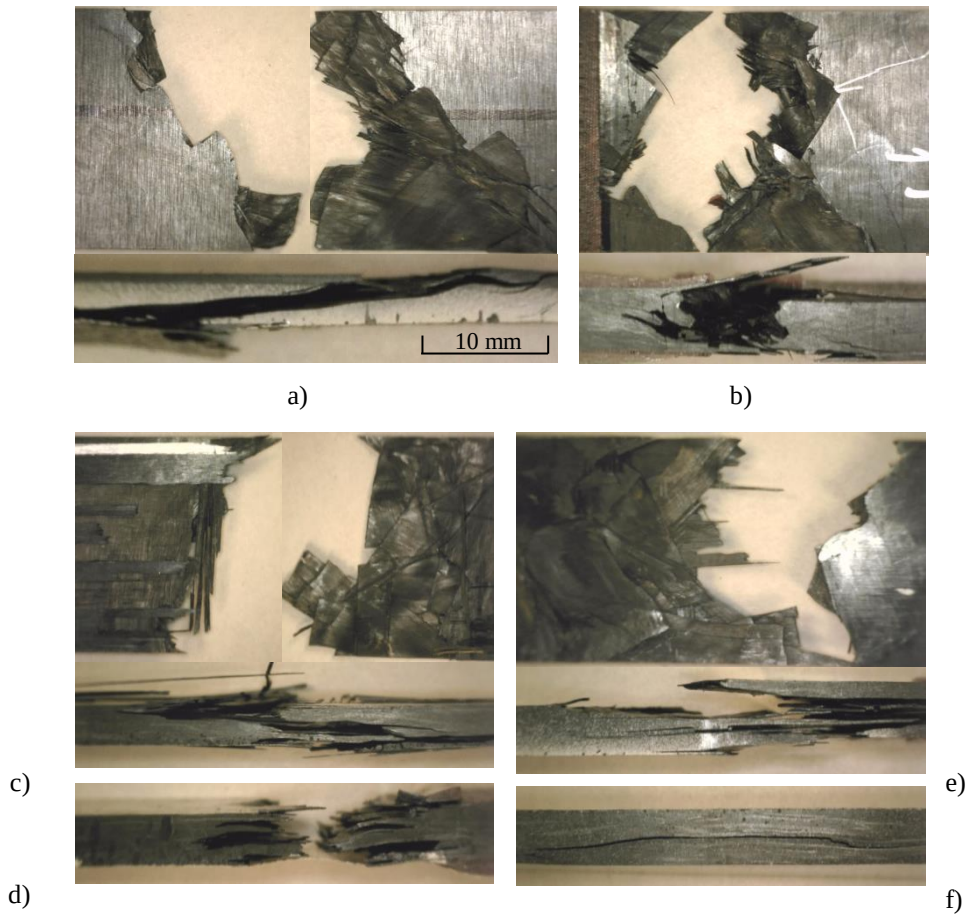

Figure 3-12: a) Typical failures comprising of fibre failure and fibre pull-out in most ROS specimens; b) Premature failures in ROS caused due to significant strand waviness; c) T-R-T configuration with long failure paths; d) T-R-T configuration with shorter failure paths; e) Long failure paths observed in R-T-R; f) Long delamination in the R-T-R specimens along the laminate interface away from the final failure

Stiffness-to-weight and Strength-to-weight ratios

Stiffness-to-weight and strength-to-weight ratios for all the test configurations are compared with each other and with 7075 aluminum (Figure 3-13.a). Aluminum has higher stiffness-to-weight ratio (~20% higher) compared to ROS material while quasi-isotropic laminate has equivalent stiffness-to-weight ratio to Aluminum. With 15/85 CP-R hybrids, the T-R-T stacking exceeds the

ratio for Aluminum. Stiffness-to-weight ratios for 20/80 CP-R hybrids are much higher than 15/85, which is the effect of increasing the laminate groups. With QI-R hybrids, the 40/60 thickness ratio exceeds the stiffness-to-weight ratio of aluminum. AP-R hybrids exhibit a huge improvement in the stiffness-to-weight ratio compared to that of angle-ply laminate. Similarly, the comparison of the strength-to-weight ratios is depicted in Figure 3-13.b. A clear increase in strength-to-weight ratios can be observed with the increase in the proportions of the laminate groups. Thus, hybridization enhances the stiffness-to-weight and strength-to-weight ratios of ROS to values comparable with aluminum.

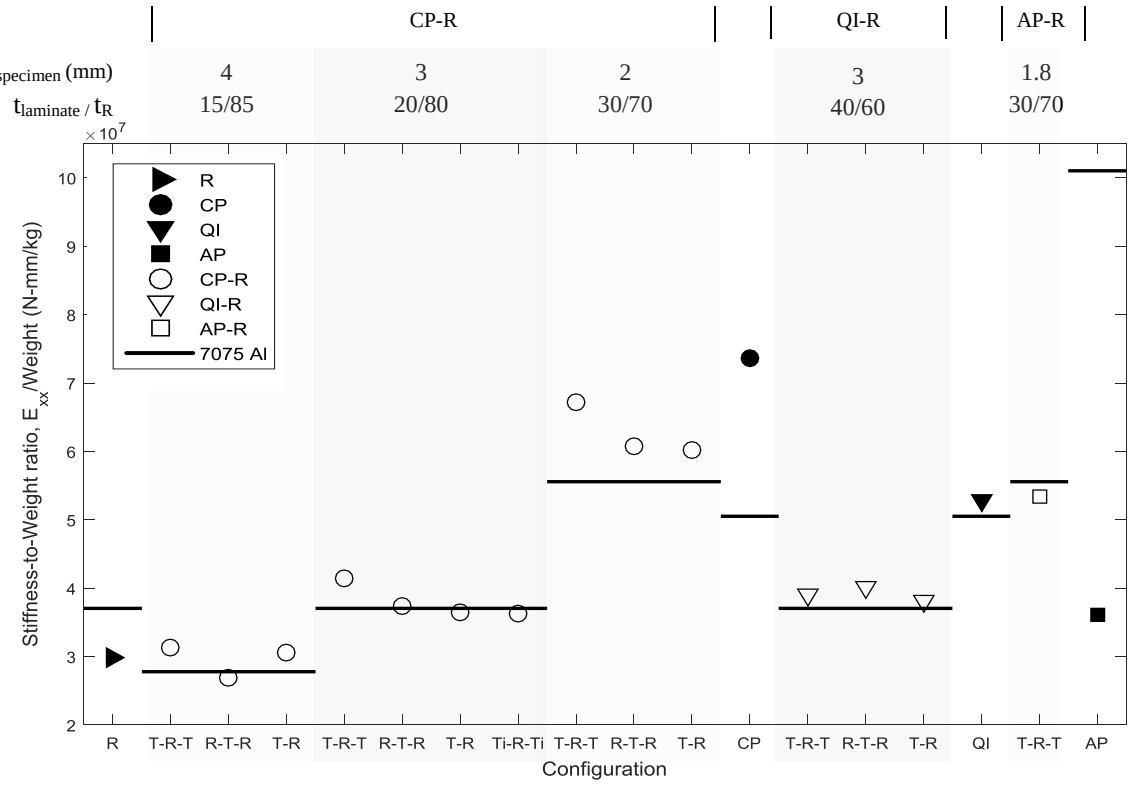

a)

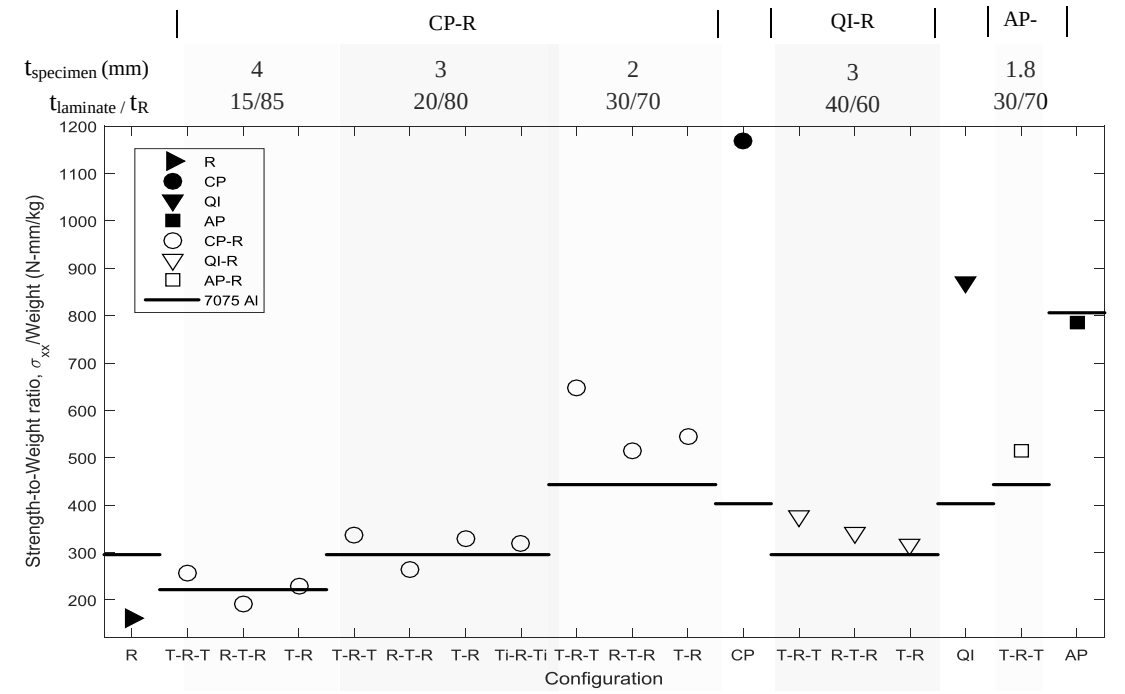

b)

Figure 3-13: a) Stiffness-to-weight comparisons; b) Strength-to-weight ratio comparisons

Synergistic effect in hybrid architectures

In addition to the reinforcement effect that compensates the properties of the weaker ROS architecture, the use of hybrid architectures of ROS and laminate groups displayed synergistic effects. The longitudinal tensile modulus of materials usually obeys the rule-of-mixtures (RoM) [124]. However, with ROS-hybrids, especially with T-R-T stacking, a positive deviation from the RoM or a positive synergy is observed in the stiffness and strength behaviour in all hybrids (CP-R, QI-R and AP-R) across all thickness ratios (15/85, 20/80, 30/70) (Figure 3-14.a, b). A positive deviation in the modulus as high as 19% is observed with 20/80 CP-R hybrids, +13% deviation in QI-R and +24% in AP-R hybrids. The strength of 15/85 CP-R hybrid is accompanied by a deviation of +20%. From the graphs we observe that the deviation is the highest at approximately in-between 20/80 and 30/70 ratios. Thus, in an ideal scenario of controlled material properties, the maximum positive synergy for the tensile performance due to hybridization would be observed at equal extensional stiffness of the phases or at the transition point (Figure 3-7). Stiffness and strength data for R-T-R and T-R configurations follow the RoM (Figure 3-14.c, d).

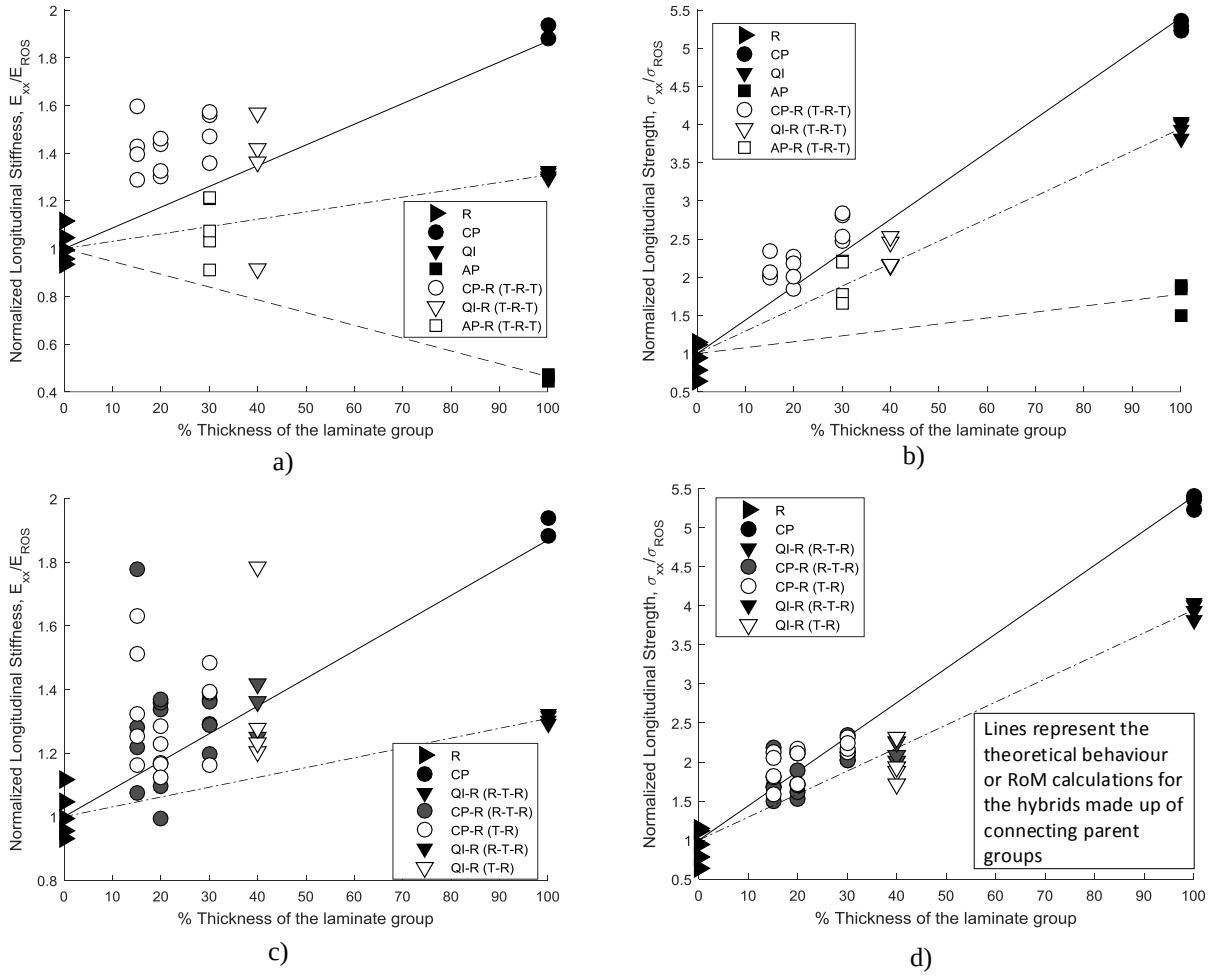

Figure 3-14: a), b) Hybridization (T-R-T) stiffness and strength; c), d) (R-T-R) and (T-R) stiffness and strength

In the literature, two or more distinct phases chosen for hybridization are characterized by three crucial aspects: strain compatibility, varied strength and stiffness characteristics [22]. Hybrid architectures of ROS and laminate groups are also characterized by the same three aspects. In the review work [22], the authors summarize two major hypotheses that lead to the synergistic effect in interply hybrids: the residual stresses hypothesis and the failure development hypothesis. The hybrid effect in filamentary structures is attributed to residual shrinkage stresses due to differences in the thermal contraction of the two phases [22]. It was reported that the thermal effect can only account for the synergistic effect of up to 10%, while hybrid effects of up to 50%

have been reported in the literature. However, ROS-hybrids exhibit warpage in the panels due to the differences in thermal properties in the heterogeneous meso-structure. Warpage in panels could cause eccentricities while loading and reduce the load carrying capacity. In contrast to the argument, a positive deviation from RoM of up to +20% is observed in T-R-T hybrids. Thus, the occurrence of positive synergistic deviation due to the residual thermal stresses is considered low or negligible.

The second hypothesis is the damage development process. In filamentary hybrid structures, as one of the fibres breaks, it locally loses its load carrying capacity and the load transfers back to the neighbouring fibres through the matrix. Fibre bridging caused by the neighbouring undamaged fibres allows the damaged fibre to regain its strength at a specific distance from the damage. At the damaged locations, the neighbouring fibres will be subjected to stress concentrations of ~5% to ~15% [22] and lead to an increased failure probability, leading to the development of clusters of broken fibres with increasing strain. If one of these clusters grows large enough, an unstable final failure follows. The same analogy could be used at the macro-level to describe the failure development process of ROS-hybrids and illustrated in Figure 3-15.

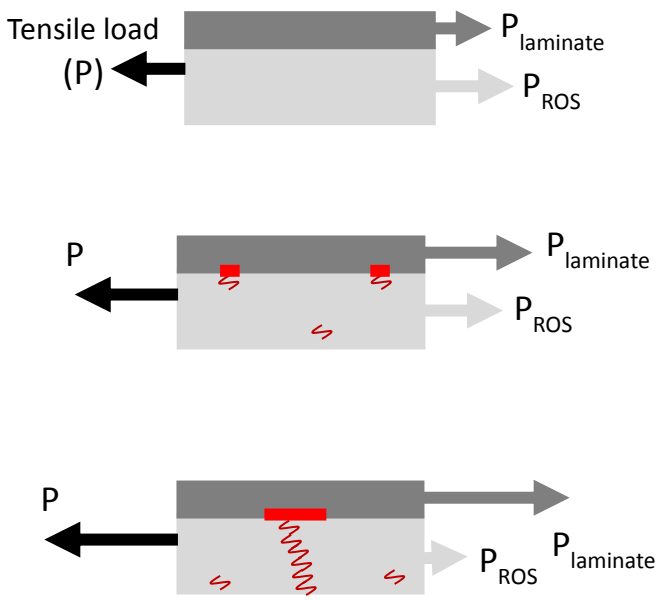

Figure 3-15: Illustration of the failure development process in ROS-laminate group hybrids

As the ROS-hybrid is loaded, multiple local failure initiations appear within the ROS phase (Figure 3-15). The multiple damage initiations have been observed by several researchers through non-destructive inspections and ultrasound scans [41, 125]. These damage locations cause stress concentrations at the ROS-laminate interfaces. The ROS phase regains its strength at a certain distance from the damage location due to the fibre bridging effect of the laminate group as the ROS phase is still in contact with the laminate group in all locations except the damage location or, in other words, the laminate group is bridging the ROS phase. This effect enhances the failure strength of the ROS phase and causes the 'reinforcement effect'. As the load increases, multiple local failures in the ROS cause increased stress concentrations along the ROS-laminate interface. The set of damages in the ROS phase grow into a cluster capable enough to reduce the load carrying capacity of the ROS phase greatly while causing high stress concentrations at the ROS-laminate interface. Further, the total failure of the laminate group occurs at loads much below its intended capacities because of these high stress concentrations. It

should be noted that the ROS phase despite the significant loss of the load carrying ability, does possess some minimal integrity [11] due to the complex meso-structure that resists the complete failure. Multiple failures have been observed in many hybrid specimens that supports the damage development hypothesis. Nevertheless, a precise explanation and quantification of the positive deviation in T-R-T specimens is rather complex and could be attributed to several factors that govern the failure characteristics, load sharing and load redistribution. Thickness ratios and stiffness ratios play a vital role in determining the load sharing among the phases. The heterogenous meso-structure and staggered patterns govern the rate at which the failure clusters are developed within ROS. The stiffness of the laminate group and the layup decides the bridging ability of the laminate group in the hybrid. Matrix toughness and plasticity add more complexities to the behaviour at the clusters and interfaces. Advanced simulations must be adopted to better understand the damage development process.

3.1.4 Conclusion

Hybrid architectures of randomly oriented strands and laminate groups represent a trade-off solution of formability and performance characteristics. Three aspects of hybridization are explored: processing observations, mechanical behaviour under tension loads, and the synergistic effect due to hybridization. Processing benefits of hybridization include reduction in warpage and strand waviness. Flat Area Fraction, an easily quantifiable parameter for warpage measurement has been introduced. Hybridization reduces the warpage and increases the Flat Area Fraction. QI-R hybrid is the least warped. Further, strand waviness in ROS phase is reduced when laminates are stacked in T-R-T configuration, followed by T-R and R-T-R.

The tensile behaviour (tensile stiffness, tensile strength, tensile strain-to-failure) of fibre architectures of ROS and laminate groups (Cross-ply, Angle-ply and Quasi-isotropic) is quantified and compared with each other and with aluminum. The thickness of the ROS phase, strand out-of-plane waviness, hybrid stacking configuration and the ratio of the extensional stiffness of the phases have a significant effect on the tensile properties. Improvements of up to 40% in stiffness, and strength improvements as high as twice are observed for a CP-R hybrid with T-R-T stacking with only 15% of laminate reinforcement. Similarly, thickness ratios of 20/80 and 30/70 demonstrate higher properties owing to increased proportion of the laminate. Strain-to-failure enhancements of up to 40% are observed for CP-R hybrids with 15/85 thickness ratio and about 60% for QI-R and AP-R hybrids. Consistent improvements were reported on QI-R and AP-R hybrids. T-R-T configuration produces the best results in terms of stiffness, strength and variability. ROS-hybrids produce better stiffness-to-weight and strength-to-weight ratios and could serve as an effective replacement for aluminum.

Addition of laminate groups enhances the properties of the ROS phase by almost twice, through the reinforcement effect possibly resulting from the fibre-bridging phenomenon. Although the fibre and the matrix systems of ROS and laminate groups are the same, their distinct properties qualify them as two different materials from the perspective of hybridization. Synergistic effects exist between these architectures when stacked in a T-R-T stacking configuration. A positive deviation from the rule-of-mixtures of 19-24% in stiffness and 20-27% in strength is observed across all hybrids with T-R-T stacking. The graphs show that the positive synergy is the highest at the transition point, at which the extensional stiffness of ROS and laminate groups are equal.

3.2 Modelling Work

This sub-chapter is not included in manuscripts. The focus of this sub-chapter is the proposition of a simplistic meso-structure model that generates the absolute and relative behaviour of ROS and ROS-hybrids with reasonable accuracies. The current work utilizes semi-empirical and stochastic 2D and 3D FE modelling approaches with progressive damage to simulate the tensile behaviour of the ROS and the Cross-ply/ROS 30/70 hybrid configuration. The stochastic 3D FE modelling utilizes three important stages: the use of a strand placement and generation procedure representative of the heterogeneous meso-structure; intralaminar progressive failure analysis using Hashin failure criteria for damage initiation and a fracture energy based linear softening law for damage propagation; and the use of traction-separation laws for the cohesive elements to model interlaminar behaviour. In addition, the modelling calls for the use of empirical parameters, derived from measurements from the micrographs of the final state of the meso-structure. The 2D model utilizes the first two stages and excludes the interlaminar progressive behaviour. Both 2D and the 3D models possess the same strand and laminate definitions. Effects of hybridization on the stress-strain behaviour, failure characteristics, and the variability are quantified and compared with the experimental results.

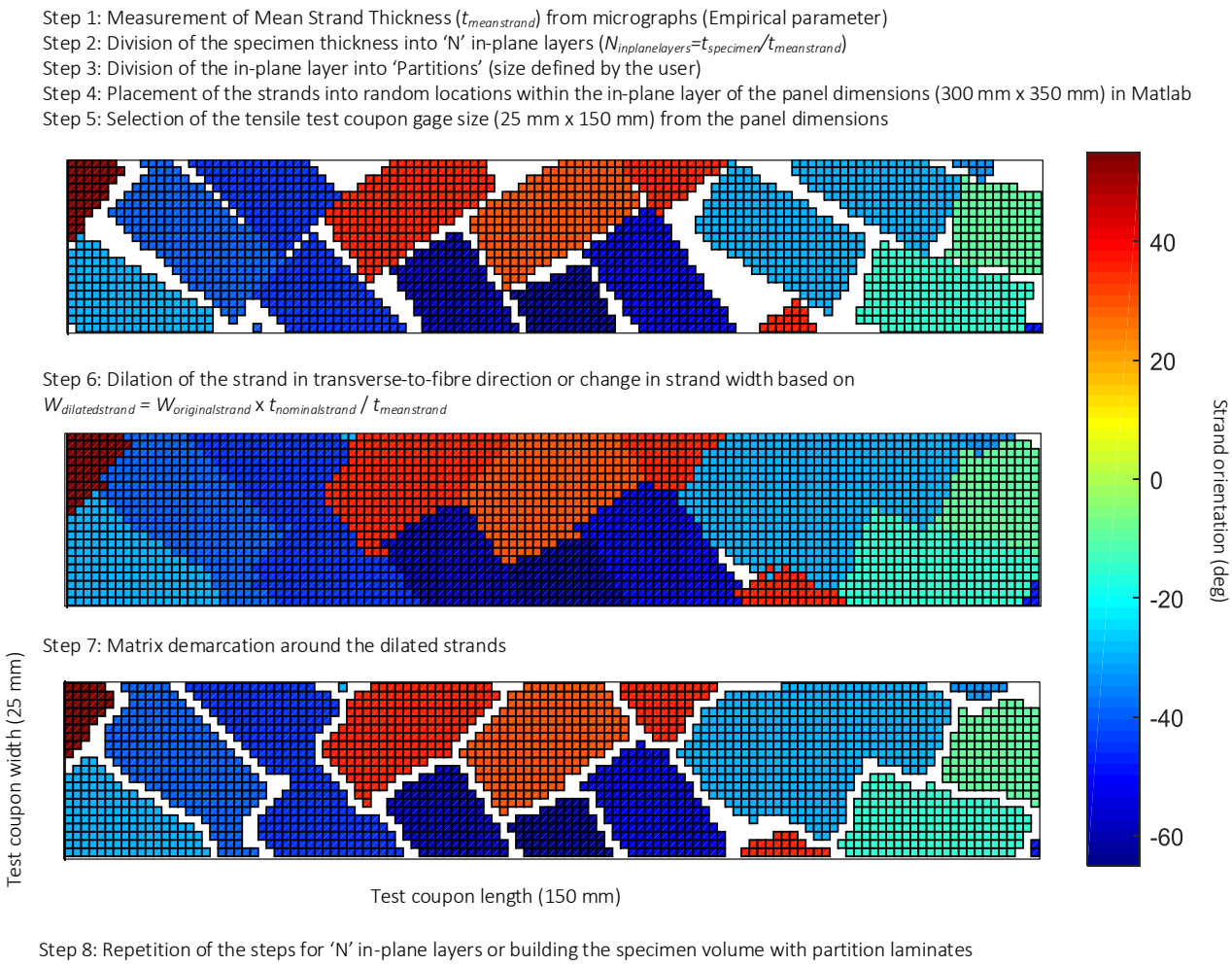

Figure 3-16: Strand generation procedure (with a partition size of 1.25 mm x 1.25 mm)

3.2.1 Randomization algorithm and Laminate analogy

The strand generation procedure generated in Matlab is illustrated in Figure 3-16, while a detailed description of the randomization algorithm is given in [28]. ROS specimens, when discretized into a uniform mesh of smaller units referred to as 'partitions', can be regarded as an assembly of arbitrary layups filling up the partitions. While the strand arrangement is random in 3D space, the arrangement of the strands is analogous to that of a laminate (referred to as 'Partition laminate') on the scale of a partition. Based on the strand size, the strands extend

across various partitions establishing the continuity of the strand thus filling the partitions with ply properties. In this work, a realistic way of dilating the strands is included to compensate for the change in strand thickness. Continuity of strands across partitions is maintained. Resin properties are assigned to the partitions plies that are unfilled by the strand dilations. A defect-free microstructure is assumed due to the low void content. The discontinuity between strands is modelled by resin demarcation, which separates two strands in any direction within an in-plane layer while the in-plane layers are mutually separated through cohesive element interfaces. The matrix demarcation around the strands replicates the shear load transfer mechanism between the in-plane layers. While the initial strand arrangements and the flow could induce strand out-of-plane waviness in ROS parts, higher part thickness and hybridization reduces the strand waviness [13]. Strand waviness is analogous to ply waviness that result in interlaminar normal and shear stresses causing pre-mature failure [123]. However, the model assumes planar strand arrangements for the strength predictions thus, slightly over estimate the strengths of ROS and some hybrid configurations. The cells filled by the matrix within an in-plane layer is assigned isotropic properties while the cells filled with ply properties are assigned properties as per their orientations.

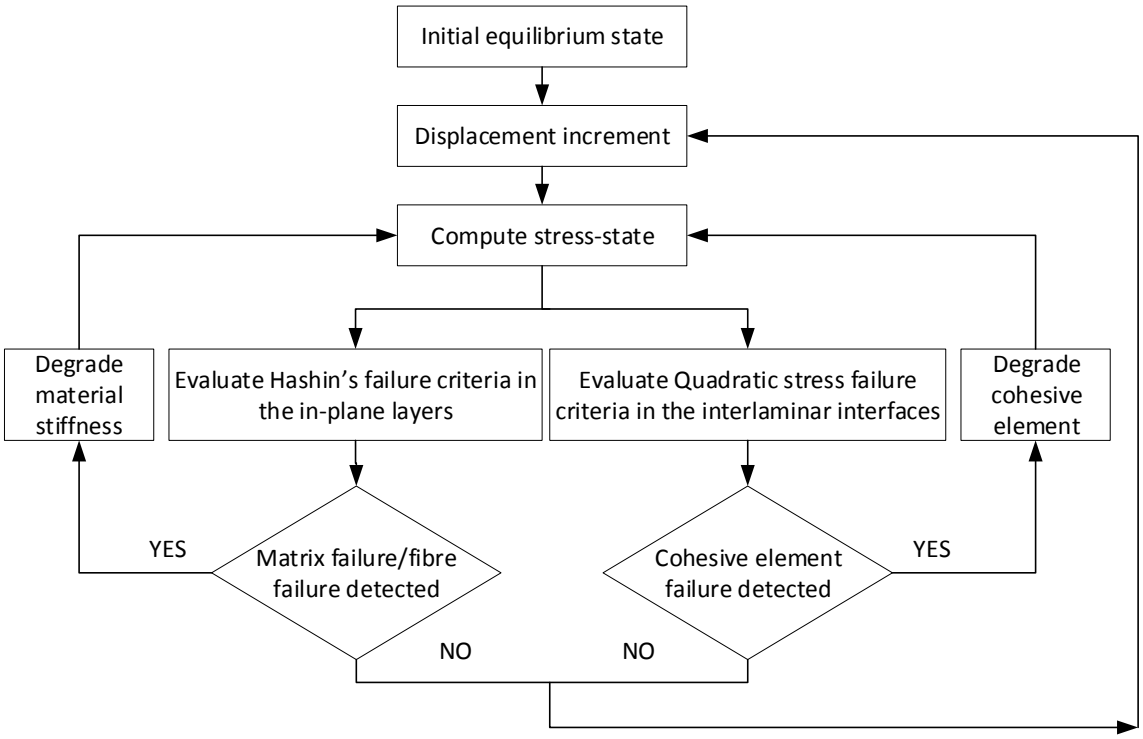

Figure 3-17: Flowchart of the progressive damage analysis of the ABAQUS FE model

3.2.2 Intralaminar progressive failure analysis

The in-plane strand behaviour is modelled using the progressive analysis [107, 126, 127] comprising of three aspects: failure initiation in the specimen according to Hashin's failure criteria, damage propagation modelled by a linear softening law based on fracture energy dissipation and damage stabilization by a viscous regularization scheme. Damage initiation or the onset of damage is governed by Hashin's failure criteria (Equation 3-1 to Equation 3-4) [128] that accounts for the combined effect of various stress components on each failure mode while differentiating the fibre and matrix failure modes and are available in ABAQUS.

Fibre tension ($\sigma_{xx} \geq 0$): $$F_f^t = \left(\frac{\sigma_{xx}}{X^T}\right)^2 + \left(\frac{\tau_{xy}}{S^L}\right)^2$$ Equation 3-1

Fibre compression ($\sigma_{xx} \leq 0$): $$F_f^c = \left(\frac{\sigma_{xx}}{X^C}\right)^2$$ Equation 3-2

Matrix tension ($\sigma_{yy} \geq 0$): $$F_m^t = \left(\frac{\sigma_{yy}}{Y^T}\right)^2 + \left(\frac{\tau_{xy}}{S^L}\right)^2$$ Equation 3-3

Matrix compression ($\sigma_{yy} \leq 0$): $$F_m^c = \left(\frac{\sigma_{yy}}{2S^T}\right)^2 + \left[\left(\frac{Y^C}{2S^T}\right)^2 - 1\right]\frac{\sigma_{yy}}{Y^C} + \left(\frac{\tau_{xy}}{S^L}\right)^2$$ Equation 3-4

In the above equations, σ_{ij} represents the components of the effective stress tensor; X^T and Y^T denote longitudinal and transverse tensile strength; X^C and Y^C denote longitudinal and transverse compressive strength; S^L and S^T denote longitudinal and transverse shear strength.

Damage propagation is modelled by linearly softening the material based on the concept of fracture energy dissipation [129] and the equivalent stress-displacement curve. The equivalent displacement (δ_{eq}) is used to calculate the damage variable (d) corresponding to the particular failure mode such that the total energy dissipated for a failure mode does not exceed the area under the stress-strain curve, which is then used to compute the damaged stiffness matrix (C_d) of the laminate [129]:

$$d = \frac{\delta_{eq}^f(\delta_{eq} - \delta_{eq}^o)}{\delta_{eq}(\delta_{eq}^f - \delta_{eq}^o)}$$ Equation 3-5

where δ_{eq} is the current displacement; δ_{eq}^o is the displacement at which the damage initiation criterion for that mode is met, and δ_{eq}^f is the displacement at which the material is completely

damaged.

$$C_d = \frac{1}{D}\begin{bmatrix} (1-d_f)E_x & (1-d_f)(1-d_m)\nu_{yx}E_x & 0 \\ (1-d_f)(1-d_m)\nu_{xy}E_x & (1-d_m)E_y & 0 \\ 0 & 0 & (1-d_s)G_{xy}D \end{bmatrix} \quad \text{Equation 3-6}$$

where

$$D = (1-d_f)(1-d_m)\nu_{xy}\nu_{yx} \quad \text{Equation 3-7}$$

In this expression, d_f, d_m and d_s are the damage variables that denote the current state of fibre, matrix and shear damage calculated specifically for each of the failure modes using Equation 3-5.

3.2.3 Interlaminar progressive failure analysis

Simulating the interlaminar behaviour is crucial since strand delamination was shown to be one of the primary failure modes [12]. The interaction between the in-plane layers is defined through surface-based cohesive elements with negligible thickness and linear elastic traction-separation interaction behaviour prior to damage (Figure 3-18). The initial uncoupled cohesive contact stiffness is defined by the normal and tangential stiffness components (K_n, K_s, K_t).

A Quadratic stress criterion is used for the damage initiation:

$$\left(\frac{\sigma_n}{\sigma_{Imax}}\right)^2 + \left(\frac{\sigma_s}{\sigma_{IImax}}\right)^2 + \left(\frac{\sigma_t}{\sigma_{IIImax}}\right)^2 = 1 \quad \text{Equation 3-8}$$

where σ_n is the normal contact stress in the pure normal mode, σ_s is the shear contact stress along the first shear direction, and σ_t is the shear contact stress along the second shear direction

defined as the cohesive forces acting along the contact normal and shear directions divided by the current area at each contact point. The parameters σ_{Imax}, σ_{IImax} and σ_{IIImax} represent the peak values of the contact stress when the separation is either purely normal to the interface or purely in the first or the second shear direction, respectively. Likewise, δ_{Imax}, δ_{IImax}, and δ_{IIImax} represent the peak values of the contact separation, when the separation is either purely along the contact normal or purely in the first or the second shear direction, respectively. Similarly, δ_{If}, δ_{IIf}, and δ_{IIIf} represent the separations at failure and are used to calculate the damage variables at a failure mode.

The damage evolution or the progressive degradation of the cohesive stiffness for the surface-based cohesive elements is characterized by energy-based damage evolution criteria as a function of mixed mode using Benzeggagh-Kenane (B-K) analytical forms, as shown in Equation 3-9.

$$G_{IC} + (G_{IIC} - G_{IC})\left(\frac{G_{shear}}{G_T}\right)^{\eta} = G_{TC} \quad \text{Equation 3-9}$$

with

$$G_{shear} = G_{II} + G_{III} \quad \text{Equation 3-10}$$

$$G_T = G_I + G_{shear} \quad \text{Equation 3-11}$$

where G_{IC}, G_{IIC} and G_{IIIC} are the critical energy release rates for normal mode, first shear and second shear directions respectively. A very low viscosity coefficient is specified for damage stabilization and convergence. All the values are listed in Table 3-4.

The underlying behaviour for the progressive degradation is similar to that of the in-plane progressive degradation except that the fracture energies dissipated in the former are for fibre tension/compression and matrix tension/compression while the energies used here are the critical energy release rates for the interfaces (normal, and shear directions). Thus, the same illustration

Figure 3-18 can be used to illustrate the damage evolution with equivalent stresses as the abscissa and equivalent displacement as the ordinate, while the energies dissipated would be G_{ft}, G_{fc}, G_{mt} and G_{mc}.

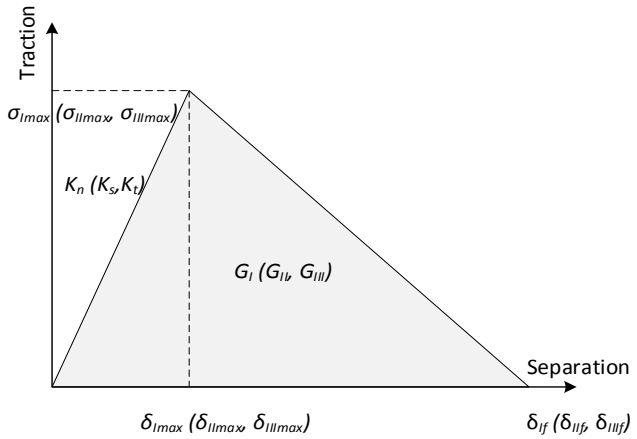

Figure 3-18: Energy based traction-separation damage evolution for the cohesive interfaces

Material properties*	Carbon/PEEK prepreg	Pure PEEK resin [38]
Longitudinal modulus, E_x	130	3.7
Transverse tensile modulus, E_y	10	3.7
Poisson's ratio, υ_{xy}	0.33	0.3
In-plane shear modulus, G_{xy}	5.2	1.42
Interlaminar shear modulus, G_{xz}	5.2	1.42
Out-of-plane shear modulus, G_{yz}	3.7	1.42
Longitudinal tensile strength, X^T	2280	100
Longitudinal compressive strength, X^C	1300	100
Transverse tensile strength, Y^T	86	100
Transverse compressive strength, Y^C	86	100
Longitudinal shear strength, S^L	152	70
Transverse shear strength, S^T	94	70

* All the modulus values are in [GPa] and all the strength values are in [MPa]; Out-of-plane shear modulus was calculated based on the transverse isotropic assumption; and transverse tension and compression strengths were assumed to be the same

Table 3-2: Stiffness and strength properties of carbon/PEEK prepreg and pure PEEK resin

Fracture energy (N/mm) [126]	Carbon/PEEK prepreg	Pure PEEK resin
Longitudinal (fibre) tension, G_{ft}	1	10
Longitudinal (fibre) compression, G_{fc}	1	10
Transverse (matrix) tension, G_{mt}	10	10
Transverse (matrix) compression, G_{mc}	10	10
Viscous regularization factor	0.0001	

Table 3-3: Damage evolution properties of carbon/PEEK and pure PEEK resin for intralaminar analysis

Fracture properties [126, 127]	
$K_I = K_{II} = K_{III}$ [N/mm^3]	10^6
Damage initiation	
Normal strength allowable, σ_{Imax} [MPa]	80
Shear strength allowable in the first and second shear directions, $\sigma_{IImax} = \sigma_{IIImax}$ [MPa]	100
Damage evolution and stabilisation	
Critical energy release rate for normal mode, G_{IC} [N/mm]	1.7
Critical energy release rate for shear modes, $G_{IIC} = G_{IIIC}$ [N/mm]	2
Viscosity coefficient	0.002
η, B-K coefficient	2.284

Table 3-4: Carbon/PEEK properties for cohesive surface behaviour (interlaminar analysis)

3.2.4 Implementation through finite element modelling

The strand placement procedure in Matlab was interfaced with ABAQUS finite element software through custom Python language scripts resulting in a fully automated procedure for creating two-dimensional (2D) or three-dimensional (3D) FE models or virtual specimens of ROS and ROS-hybrids. The FE modelling introduces three characteristic parameters: partition size, mesh size and virtual specimen size or RVE size. Partition is the smallest area within an in-plane layer

with a distinct ply orientation. Thus, smaller partition sizes define the strand geometries better. In the literature, while Feraboli et al. [105] determined the partition size based on the coarseness of the DIC contours, Selezneva et al. [107] showed that a partition size of 1.0 mm provided results within 6% compared to a size of 0.5 mm in terms of convergence.

Mesh size is another parameter that governs the convergence, the total resin rich area in the specimen and the choice of the partition size. Smaller mesh sizes produce accurate results with a compromise on the computational time while larger mesh sizes would increase the resin volume fraction within the specimen. Further, a sensitivity analysis of the mesh size in the range of 0.5 – 3.0 mm by Selezneva et al. [16] showed that no observable effects except that the use of larger mesh sizes resulted in coarser pattern of field quantity contours. Further, it was noted that the mesh size must be at least the size of the partition or finer, as each mesh element must be fully within a partition (i.e. it cannot be split between two partitions with different layups). Thus, for the virtual specimens, a mesh and partition size of 1.0 mm x 1.0 mm was chosen as a trade-off between the accuracy, total resin rich area and the computational time. Excluding the matrix demarcation, the total resin rich area in the virtual specimens with 1.25 mm mesh size was ~8-9% while the mesh size of 1.0 mm produced a resin rich area of ~3-4% typically as measured from the micrographs. The heterogeneous meso-structure in ROS complicates the process of determining the critical dimensions for RVE definition [102] due to the lack of periodicity or due to the large sizes of RVE required to define periodicity compared to that of part sizes. Further, testing as per ASTM methods requires a finite width of the specimens resulting in various fibre lengths within the specimen. Thus, the virtual specimens are selected analogous to the way the test specimens are cut from a panel. Thus, the size of the virtual specimen was chosen to be 25 mm (same as test specimen width) while the length was chosen to be twice the length of the

strand (50 mm) to be able to distinguish a strand aligned at zero and a zero-degree tape in the laminate group. Both, the strand and specimen lengths have negligible differences in their stiffness contributions if fibre length/fibre diameter ratios are considered according to Halpin-Tsai relations [130]. Further, both initial strand length and virtual specimen length are >> 50 x fibre critical length, thus allowing for an efficient stress transfer as noted by Chang et al. [6].

Two types of FE models were used to simulate the virtual specimens: a) 2D FE model: utilizing the randomization algorithm and the intralaminar progressive failure method; b) 3D FE model: utilizing the randomization algorithm, intralaminar and interlaminar progressive failure methods. Both 2D and 3D models use the same partition size, layup, and virtual specimen sizes. A comparison between the 2D and 3D models is made to emphasize the importance of the interlaminar progressive failures for the strand sizes chosen. The 2D model is meshed using general-purpose reduced integration conventional shell element (S4R). The 3D FE model is meshed using 8-noded hexahedron element continuum shell element (SC8R) for the in-plane layers while the interfaces are modelled with surface-based cohesive behaviour. Thus, both progressive damage analysis within the in-plane layer and interfaces can be modelled using Hashin's damage initiation and energy based cohesive failure respectively in a 3D model. For the boundary conditions, a constant displacement is applied along one edge, and the opposite edge is restrained in the longitudinal direction. The other degrees-of-freedom (dof) are such that the rigid body rotations of the model are restrained, while the model can expand or contract laterally in the width direction and in the through-thickness directions, as shown in Figure 3-19. Similar boundary conditions were applied on the 2D model. The stress-strain curve is captured by incrementally applying a displacement and measuring the force and moment resultants. Five virtual specimens were generated with randomized layups for each test configuration. Failure

was assumed to occur when the model failed to converge in the FE analysis. Loading was applied incrementally with a constant step size, but as the element properties began to degrade, the step size was automatically reduced with the aim to achieve convergence. As noted in ABAQUS [129], stiffness degradation in materials led to convergence difficulties, which were mitigated with a viscous regularization scheme. The viscous regularization factor ensures that the tangent stiffness matrix is positive definite for a sufficiently small-time increment. The higher the viscosity coefficient, the higher is the fracture load. Based on the parametric studies [107, 126, 127] of the influence of the mesh size and viscous regularization factor, the best choice of the viscosity coefficient and the fracture energies were determined. Further, the 2D and 3D models were validated against two sets of experimental tests before implementing them on ROS and ROS-hybrids: a) On standard laminates such as QI, AP and CP; b) On the aligned slit-tape experiments from Selezneva et al. [98]. The results from the tensile test simulations matched the classical laminate theory calculations of standard laminates (QI, CP) with <2% errors in mean stiffness and <5 % for the mean strength behaviour with the chosen parameters. Further, the simulations matched with <5% errors with the slit-tape experiments for the shorter overlap specimens whose failures were primarily driven by the matrix shear properties.

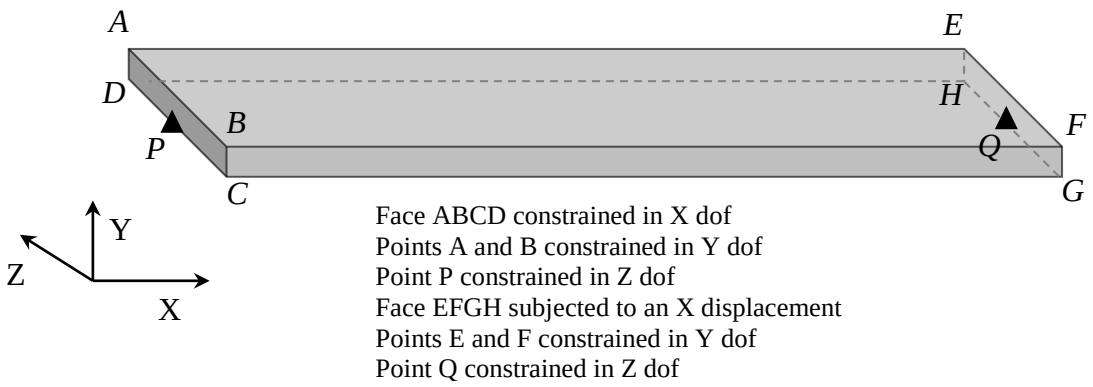

Figure 3-19: Boundary conditions imposed on the virtual tensile specimen

Table 3-2, Table 3-3, and Table 3-4 list the FE parameters used for the modelling along with their references.

The stiffness and strength prediction of ROS based specimens are rather complex owing to the multitude of parameters governing their mechanical behaviour. While the 2D and 3D models are certainly improvements over other 2D models in literature, there are a few limitations associated with them. The model assumes an RVE at the meso-level which inhibits the capacity to predict delamination within the strand or inter-slitting failures. Some of the primary drivers of the performance are the process parameters that influence the material properties. For example, residual stresses are induced due to uneven crystallization shrinkage and differences in the coefficients of thermal expansion within the heterogenous meso-structure. The model excludes these effects. The strand waviness has a major effect on the stiffness and strength behaviour which are excluded from the simulations. Thus, the possibility of the simulations overestimating

the properties is expected. Finally, the matrix demarcation around the strands is to avoid the load transfer between strands in the in-plane directions, while allowing only the shear load transfer mechanism between the strands. Such a demarcation adds more resin proportions into the model while reducing the stiffness of the virtual specimens.

3.2.5 Results and Discussion

Stress-strain curves

The experimental and model (2D and 3D) stress vs. strain curves for the ROS and the 30/70 hybrid configuration are depicted in Figure 3-20. The typical behaviour of the stress-strain curve for ROS is mostly linear except for the last 10-15% of the strain when the curves usually tend to be non-linear. The rapid progression of failure in the specimens causes such a behaviour. The 2D and 3D virtual models did demonstrate slight non-linearity, and local load drops with the progression of the load. While the stress vs. strain curves of both models tend to be in the same range as the test specimens, due to the reasons explained in the previous paragraph on the matrix demarcation, both 2D and 3D models tend to be less stiff and elongate more than the test specimens. The test specimens however experience stiffness and strength reduction due to the presence of strand waviness, whose precise magnitude is unknown. Nevertheless, the macro stiffness and the strengths are well predicted by both 2D and 3D models. Thus, the methodology using the in-plane layer of strands with dilation and matrix demarcation results in an improvement over the other 2D in-plane model proposed in literature. For example, the researchers [107] had showed discrepancies of ~30% for the stiffness and ~39% for strength in ROS specimens for the same strand and process parameters as this study, while this study shows a mismatch of ~25% in strength compared to the experiments. It is also important to note that

thicker virtual specimens exhibited slightly higher stiffness and strength compared to thinner ROS specimens, as observed by several researchers [12, 36, 66].

ROS and ROS-hybrid specimens, due to the heterogenous meso-structure, are influenced by tension-bending and tension-twist couplings. Thus, the deformed shapes are unique from specimen to specimen as shown Figure 3-21. Further bending and twisting reactive moments are generated in the specimens due to the couplings. Thus, the final failure of the specimens is due to a combined stress state that is caused by the moments and the axial loading. While the magnitude of these moments is unique from specimen to specimen, in a general sense, T-R-T results in a higher resultant moment due to the higher resistance offered by the tape layers placed on either side of the ROS group. The experimental curves and the virtual specimen curves match well as for the 30/70 hybrid configurations as the behaviour of laminate dominant groups are well established and predicted by FE models.

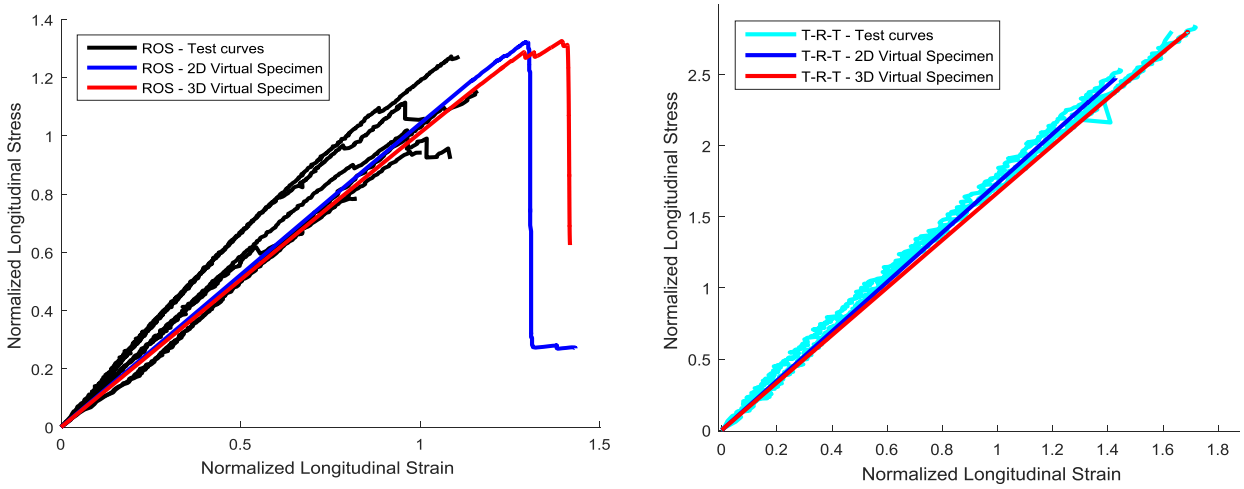

a) b)

Figure 3-20: a) Experimental stress vs. strain curves of ROS specimens and representative stress vs. strain curves of 2D and 3D virtual specimens; b) Experimental stress vs. strain curves of 30/70 T-R-T hybrid specimens and representative stress vs. strain curves of 2D and 3D virtual specimens (all the curves are normalized with reference to ROS mean properties)

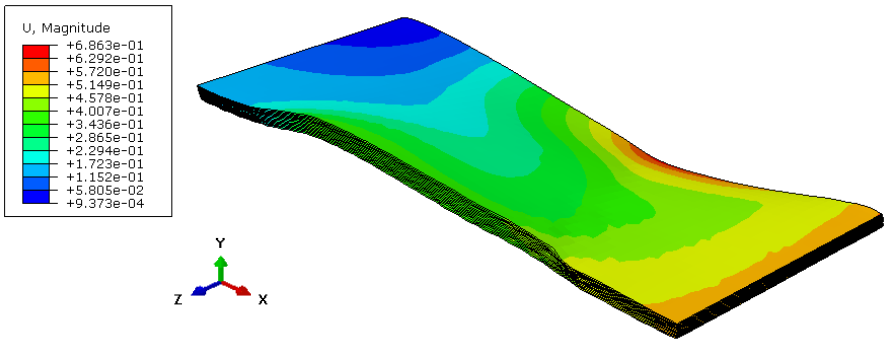

ROS

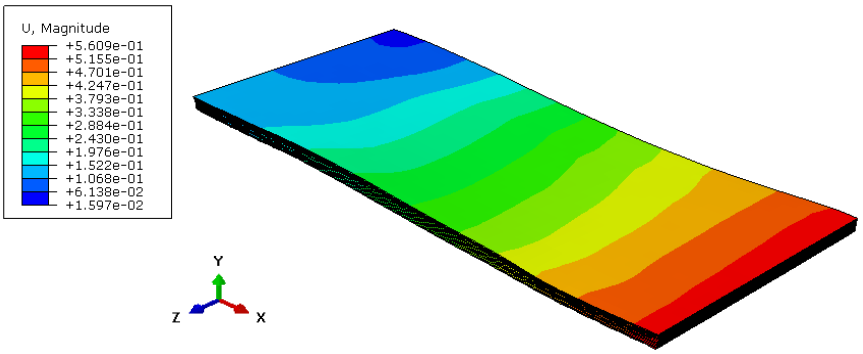

T-R-T

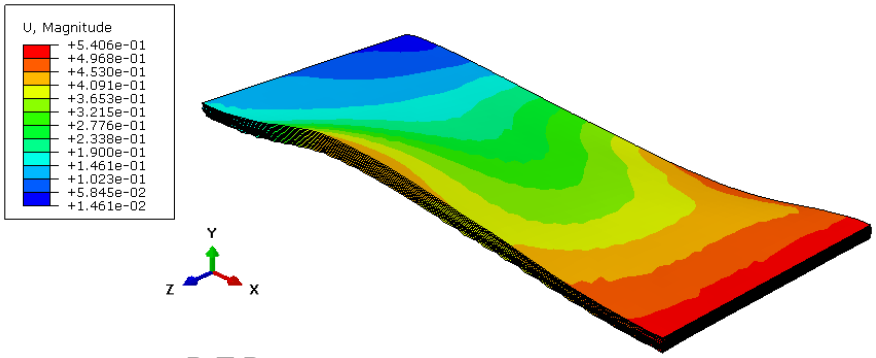

R-T-R

Figure 3-21: Deformed shapes of the virtual specimens for ROS, 30/70 thickness ratio (T-R-T and R-T-R stacking configurations) at the highest tensile load. A scale factor of x10 is used for the deformation. U is the resultant displacement in mm

Stiffness and Strength comparisons

The normalized longitudinal stiffness and longitudinal strengths of all the experimental and virtual (2D and 3D) specimens are shown in Figure 3-22. The stiffness of both 2D and 3D

models are ~10-12% lower than the experimental results. While precise explanations for such differences are unknown, reasons such as the exclusion of the strand waviness behaviour and inclusion of the matrix demarcation is believed to primarily contribute to these differences. Further, it was shown in [107] that longer strands tend to cause longer overlaps and subsequently an increase in the probability of fibre failures in the specimen. The model and the experimental results match well with the inclusion of the tapes. Overall, for all the 30/70 hybrid configurations, the stiffness predictions of the 3D virtual specimens are within ~8-12% of the experimental values, signifying that the predictability of the behaviour increases with the inclusion of the laminate groups. The model predictions for the T-R-T and the R-T-R configurations are similar. The experimental values are slightly lower for the R-T-R configuration owing to the waviness in the centrally placed laminate group. The 3D models outperform the prediction capabilities of the 2D models, due to the inclusion of the cohesive behaviour.

The strength predictions of the 2D and 3D models are ~25% higher than the experimental values for the ROS specimens. ROS specimens of 2 mm thickness, as discussed in the previous sections, demonstrate high strand waviness, which are not factored into the strength calculations of the virtual specimens. Among the hybrid configurations, the strengths for the T-R-T configurations are predicted with a greater accuracy than that of ROS specimen predictions. In the T-R-T configuration, the strand waviness is minimized by the tape layers on either side of a centrally placed ROS group. The 2D and 3D models over predict the strength of R-T-R configuration by ~8% and ~15% respectively. These differences could be attributed to the waviness in the laminate group and the strand waviness in the ROS groups. The variability in the virtual specimens is primarily due to the in-plane strand orientations while the variability in the

experimental specimens is due to the strand waviness, residual stresses, and strand orientations. Overall, the scatter in the models is similar to those of the experiments. It is to be noted that the relative differences in the stiffness and strength values between the virtual specimens are very close to that of the relative differences in the stiffness and strength values of the experiments. Such relative differences are important to quantify the relative effect of configurations in terms of a standard laminate, without extensive testing efforts. Another important aspect is that both 2D and 3D models predict the positive synergistic behaviour in the T-R-T configuration with reasonable accuracies.

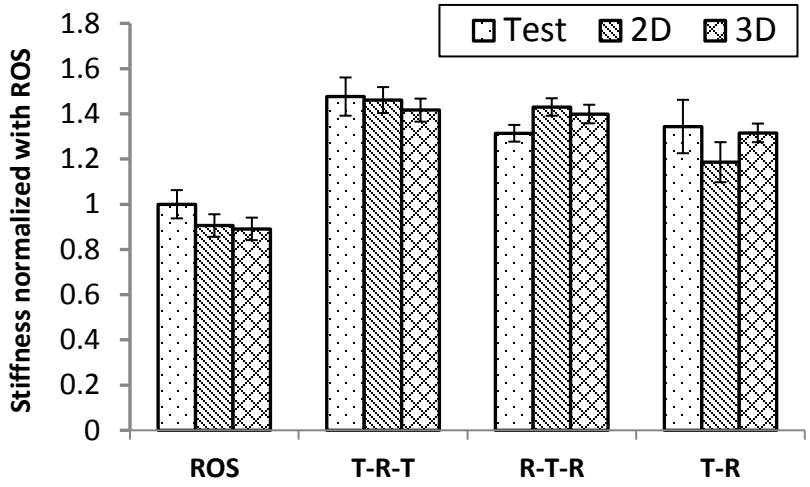

a)

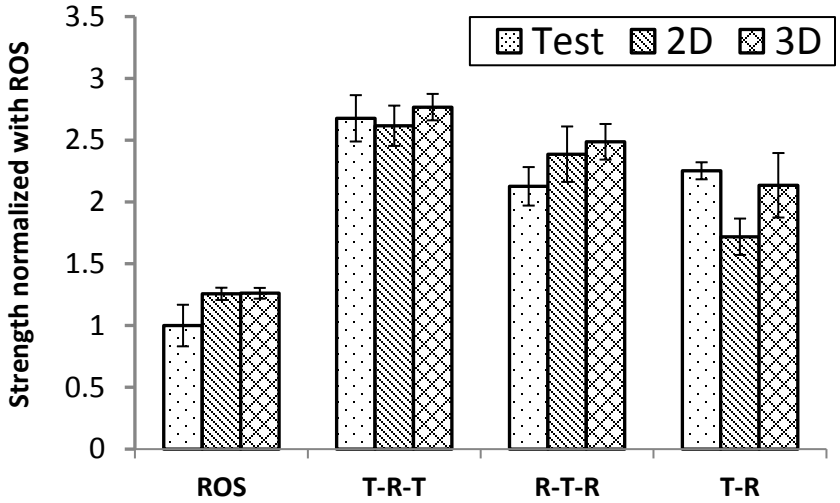

b)

Figure 3-22: a) Stiffness comparison; b) Strength comparison (all the properties are normalized with reference to ROS mean properties)

Failure characteristics

In general, for the strand sizes chosen, the failure in ROS specimens displayed a combination of fibre failures, multiple matrix failures and multiple delaminations. An example of failure indices are shown for a layer of an ROS specimen at the highest load, in Figure 3-23.a-c. The images indicate the extent of the fibre and matrix damages have reached an index of 1.00 signifying

multiple failure initiations, while the cohesive initiation has yet to reach an index of 1.00. Figure 3-23.d indicates the final failure or damage variable in the complete specimen, due to shear. A characteristic of the failures as discussed in the previous sections, is the occurrence of multiple failures within the specimen. These multiple failures could be in the form of fibre or matrix failures in an in-plane layer or due to cohesive failures in the interfaces of any two in-plane layers. Irrespective of the nature of failures, the weakest regions form a cluster leading to the final failure of the specimen.

In the T-R-T specimens, the axial load is distributed in the architectures proportional to their extensional stiffness. With the failure of one of the phases in a hybrid specimen, the load is transferred to the other remaining material until the complete specimen failure. In the chosen hybrid configuration, (i.e. 30/70), the ratio of the extensional stiffness of the laminate group to the extensional stiffness of ROS is 55:45. Extensive matrix dominated failures are observed in the ROS specimens at the highest load as shown in Figure 3-24.a. The final failure however is caused in the tape layers of the laminate group as shown in Figure 3-24.b. The R-T-R configurations demonstrated similar behaviour to that of T-R-T except that the R-T-R configurations involved much more extensive matrix failures at the interfaces with the laminate groups. Among the hybrid stacking configurations, T-R-T demonstrated the highest properties, despite all the configurations possessing similar axial properties theoretically.

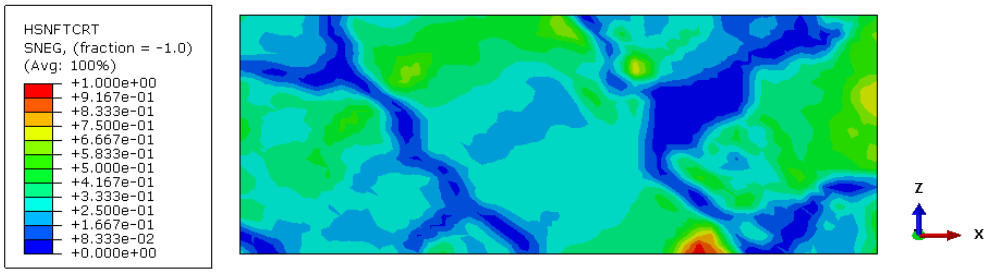

a) Hashin criteria: Fibre tension failure indices at the highest load in an in-plane layer

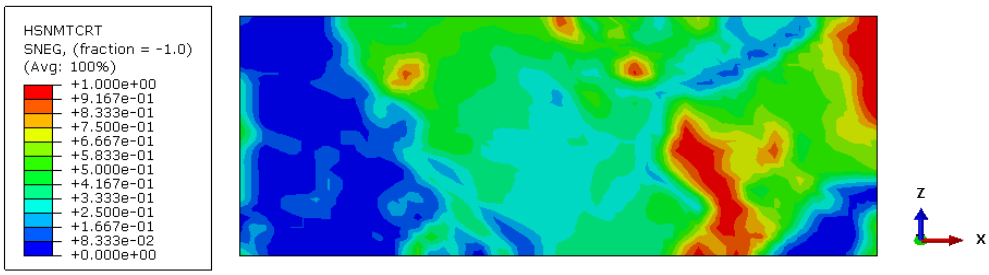

b) Hashin criteria: Matrix tension failure indices at the highest load in an in-plane layer

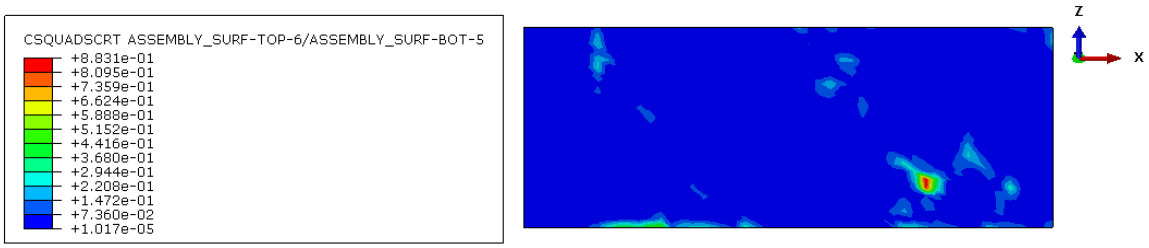

c) Quadratic stress criteria: Cohesive failure indices at the highest load between two in-plane layers

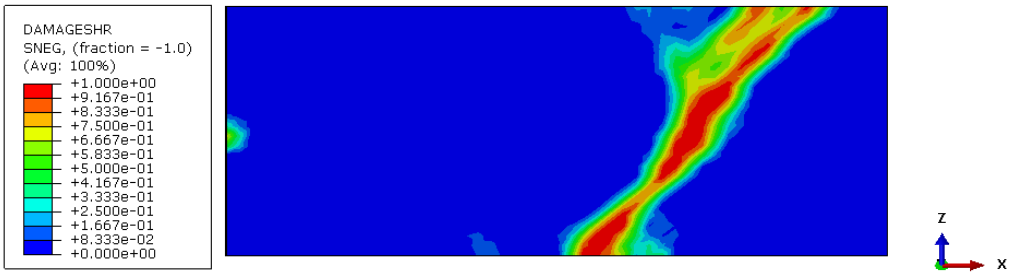

d) Final shear damage in the ROS specimen

Figure 3-23: a-c). Examples of a layer in an ROS specimen with multiple failure occurrences; d) Final shear damage in the same ROS specimen

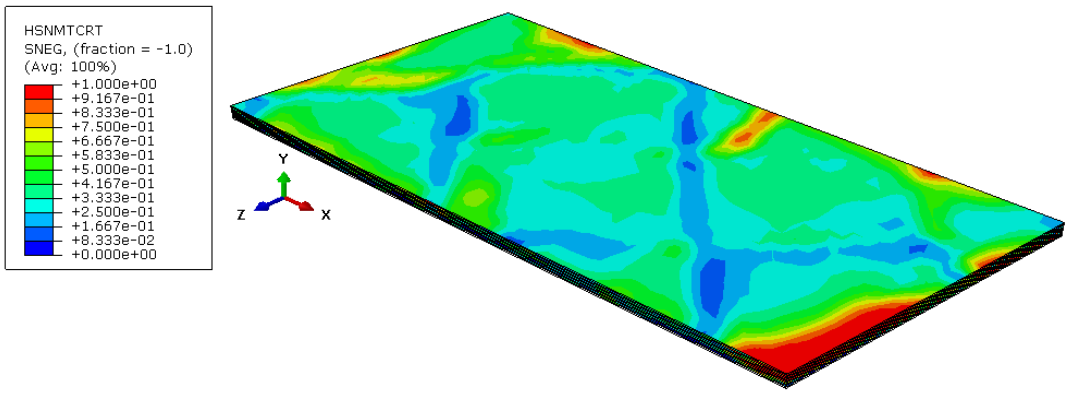

a) Hashin criteria: Matrix tension failure indices in the ROS phase in a T-R-T specimen at the highest load

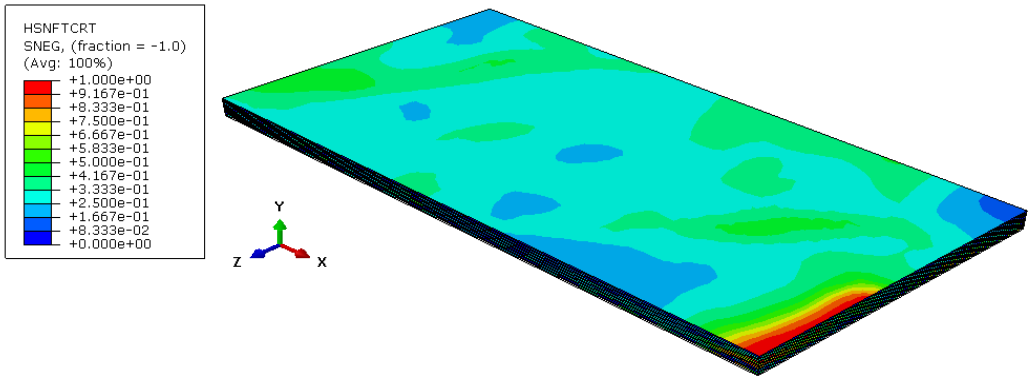

b) Hashin criteria: Fibre tension failure indices at the highest load in a T-R-T specimen indicating final failures in the tapes

Figure 3-24: Example of failure occurrences in a T-R-T specimen

3.2.6 Conclusions

Simplistic stochastic FE models (2D and 3D) have been proposed to generate the absolute and relative behaviour of ROS and ROS-hybrids. The tensile behaviour of 2 mm thick ROS specimens and hybrid fibre architectures specifically the 30/70 hybrid configuration are simulated and comparisons with the experiments have been made. The 2D model utilizes two of the following three stages: the use of a strand placement and generation procedure and empirical parameters to replicate the processing, intralaminar progressive failure analysis using Hashin failure criteria for damage initiation and a fracture energy based linear softening law for damage propagation, and the use of traction-separation cohesive element laws to model the interlaminar

progressive analysis. The 3D model utilizes both intralaminar and interlaminar progressive prediction methods. Overall, both the modelling approaches match the trends observed during experiments, predict the tensile stiffness and strength of the specimens, and provide preliminary insights into the hybridization aspects. The modelling method certainly demonstrates improvements over other 2D models in literature for ROS, while the 3D modelling is first of its kind proposed and adopted for a hybrid fibre architecture of ROS with laminate groups.

Chapter 4

Coupon Level Studies – Interlaminar Shear Behaviour

4.1 Experimental and Modelling Works – Manuscript 3

Interlaminar Shear Behaviour of Hybrid Fibre Architectures of Randomly Oriented Strands Combined with Laminate Groups

Abstract

This work explores the interlaminar shear behaviour of hybrid fibre architectures of randomly oriented strands (ROS) combined with three laminate groups (Cross-ply, Quasi-isotropic and Angle-ply laminates) fabricated using compression moulding. Apparent interlaminar shear strengths of selected configurations are measured. Effects of hybridization on the shear properties of ROS based specimens are quantified and compared with pure ROS and benchmark laminates. Shear strength of hybrid stacking sequence (with laminate groups on either side of a centrally placed ROS group) demonstrate a synergistic effect with higher strengths (up to 25%) than both parent architectures. Negative synergies (up to 20%) are observed due to the

sandwiching of laminates in-between two ROS groups. The synergy effects are attributed to the load sharing among the constituents and are explained using a semi-empirical model that utilizes a stochastic strand placement procedure and an adaptation of the analytical formulas for the interlaminar shear and bending stress distributions.

Keywords: Randomly oriented strands, Hybrid fibre architectures, Short beam shear strength, Hybrid effect

4.1.1 Introduction

Geometric features such as edges, thickness variations, and structural joints cause stress gradients in the interlaminar directions leading to delaminations in laminates. The interlaminar shear strength (ILSS) represents the resistance of a layered composite to internal forces that tend to reduce relative motion parallel to and between the layers [72] and has relatively low values compared to the longitudinal tensile strength. While ILSS is primarily a matrix dominated property, factors such as the adhesion between fibres and matrix and/or between the adjacent layers, the matrix and fibre types, fibre volume fraction, ply stacking sequence, and resistance offered by the material architecture to crack propagation govern the final failure. With ROS-hybrids, additional parameters such as the relative thickness of laminate groups compared to ROS, strand waviness and the relative stacking positions of the materials govern the performance. A few authors have studied the interlaminar shear behaviour of ROS composites. Selezneva et al. [12] measured the ILSS of pure ROS using short-beam shear strength (SBS) tests [131] and double-notch tests [132]. The double-notch tests significantly underestimated the strengths compared to the SBS tests due to the stress concentrations at the notches causing premature failure. SBS tests were reported to be appropriate for comparisons despite the complex stress state. Leblanc et al. [52] quantified the effect of the void content on the SBS strengths of

compression moulded ROS specimens and reported that a consolidation pressure of at least 60 bars is essential to minimize voids in carbon/PEEK ROS material. While specific work on quantifying the ILSS of ROS-hybrids has not been found in literature, some authors have reported improvements in the ILSS properties of random short fibres when reinforced with tapes [72].

In the literature, a few authors have developed analytical expressions for the interlaminar shear stress distribution in arbitrary layups [133]. Of interest is the work of Hajianmaleki et al. [134] who derived the expressions for through-the-thickness shear stress distribution of an Euler beam comprised of an arbitrary layup, based on the work of Vinson et al. [135]. Researchers have employed stochastic models to predict the in-plane properties of ROS. Feraboli et al. [105] captured the local modulus variability by discretizing the ROS specimen into representative volume elements (RVE) with randomly assigned material properties. The use of a large size of the discretized element, with random layups independent of their neighbouring elements, led to discontinuities of properties across the element boundaries and complicated the choice of an appropriate RVE size. Recently, Selezneva et al.[107] used a stochastic strand generation procedure to place strands with random orientations and locations within a specimen. This network of strands was then discretized using a mesh with each element representing a laminate. Classical laminate theory and finite element analysis determined the stress-strain behaviour while Hashin's failure criteria estimated the strength, under tensile loads. Further, the number of strands at a location was variable in the through-thickness direction. To achieve a uniform thickness everywhere, the thickness of each 'ply' in the partition was 'scaled' such that total thickness was a constant, without compensating for their properties. This led to the over prediction of properties and caused strand discontinuities across partitions leading to higher

property gradients between partitions. Selezneva's approach excluded the contribution of resin rich areas. Kilic et al. [49] proposed a 3D micromechanical finite element model for the analysis of ROS thermoplastic parts. The micromechanical model was not fully representative of the ROS material and required some calibration against the non-linear stress-strain curves of test-coupons. Nonetheless, the technique demonstrates good potential. Recently, a 3D finite element based stochastic modelling method for ROS parts was proposed in Digimat software [136] using a voxel based method and cohesive elements, and needs extensive validation against experimental data. None of the stochastic models deal with the prediction of out-of-plane properties at the coupon/part level. Hybridization in the literature refers to the use of two or more distinct materials characterized by the differences in their strength and elongation, typically to obtain synergistic behaviour [22]. The synergistic behaviour is usually quantified either by a positive or a negative deviation from the theoretical rule of mixtures (RoM) [23]. Such synergies in hybrids are attributed to the damage development process, residual stresses and stress concentrations [22]. Positive synergistic behaviour of tensile properties were reported [13] in ROS-hybrids, while studies on out-of-plane loading have not been carried out.

ROS-hybrids are intended for use in parts with complex geometric features. Thus, understanding the interlaminar shear behaviour is specifically important for their design. While some experimental work and no theoretical work have been performed in the literature on ILSS of ROS material; none of the works published have specific relevance to ROS-hybrids. This research work explores the interlaminar shear behaviour of hybrid fibre architectures of randomly oriented strands when combined with three laminate groups. Effects of hybridization on short-beam shear strengths, failure characteristics, load-displacement behaviour and the

variability of ROS-hybrids are quantified against pure ROS and benchmark laminate groups. The hybridization takes into consideration the effects of the thickness ratios ($t_{laminate}/t_{specimen}$), laminate stacking and stacking sequence of the architectures (hybrid stacking). Through a simple stochastic semi-empirical model and analytical expressions for the through-thickness shear and bending stresses, the synergistic behaviour of ROS-hybrids is explained.

4.1.2 Experimental work

Test methods

The short-beam shear strength test [131] is a three-point bending test that characterizes the shear resistance of fibre reinforced composites to interlaminar failure. The strength values from SBS tests are referred to as the 'apparent interlaminar shear strength' due to its dependence on the specimen geometry. The test specimen ends rest on two roller supports with the loading nose applying a load at the mid-span of the test specimen (Figure 4-1). A parabolic shear-stress distribution is expected between the loading nose and support rollers in the thickness direction. The stress distributions are skewed closer to the loading and support rollers, due to stress concentrations. With ductile matrices such as PEEK, plastic yielding may alleviate localized stress deviations. The ASTM standards ensure that the size of the specimen induces a dominant interlaminar shear mode of failure. Nevertheless, the presence of bending moments and stresses under the loading nose and supports induce a complex stress state within the test specimen. Such a complex state results in a variety of failure modes including the interlaminar shear failure, flexural failure, and failures dominated by inelastic deformations. Although under combined stress state, the short-beam shear test results provide quantitative estimates when relative

comparisons are being made, thus, allowing their use for quality control and material evaluations.

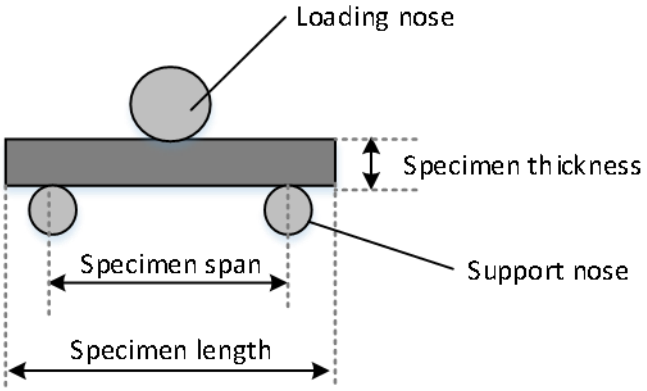

Figure 4-1: Short beam shear testing (schematic diagram – not to scale)

The test samples with thickness-to-span length, width-to-span length, and thickness-to-span length ratios of 1:4, 1:2, and 1:6 respectively, are used. Support roller radius and loading nose roller radius are 3 mm and 6 mm respectively. A loading rate of 1.0 mm/min is used on a 5kN tensile testing machine. Apparent interlaminar shear strengths for rectangular specimens are calculated using,

$$\text{Apparent interlaminar shear strength} = 3P/4bt \qquad \text{Equation 4-1}$$

Where P is the load at failure, t is the specimen thickness, s is the support span and b is the specimen width. Ten specimens for each configuration are tested and consistent failure modes with visibly noticeable interlaminar failures are reported.

4.1.3 Modelling work

Through-the-thickness stress distribution in 3-point bending scenario

The expressions for the through-the-thickness shear and bending stress distribution within an Euler beam of arbitrary layup [134] has been adapted for a simply supported beam subjected to a mid-point load. The final expressions for the bending and interlaminar stresses are listed below while their derivations are elaborated in Appendix A.

$$\sigma_x = \frac{Q_{11} F x}{2(A_{11} D_{11} - B_{11}^2)} (B_{11} - z A_{11}) \quad \text{Equation 4-2}$$

$$\tau_{xz} = \frac{F}{2b(A_{11} D_{11} - B_{11}^2)} \int_h^z Q_{11} (B_{11} - z A_{11}) \, dz \quad \text{Equation 4-3}$$

4.1.4 Strand placement procedure and stochastic model

A semi-empirical model that utilizes a stochastic strand placement procedure and analytical expressions for the interlaminar shear and bending stress distributions for an arbitrary laminate is proposed. ROS specimens, when discretized into a uniform mesh of smaller units referred to as 'Partitions', can be regarded as an assembly of arbitrary layups filling up the partitions. For example, a cross-sectional image of a hybrid specimen (Figure 4-2) shows that while the strand arrangement is random in 3D space, on the scale of a partition, the arrangement of the strands is analogous to that of a laminate (referred to as 'Partition laminate'). Based on the strand size, the strands extend across various partitions establishing the continuity of the strand.

Firstly, the mean strand thickness ($t_{meanstrand}$) is measured from several micrographs across various configurations. Measurements indicate that the consolidation pressure causes reduction

of the strand thickness compared to their nominal thickness. This is the semi-empirical parameter in the model and depends on the strand flow and consolidation pressure. In the strand placement procedure, plate dimensions as in the moulding fixture are chosen. The plate thickness is divided into '*n*' in-plane layers ($N_{inplanelayers}=t_{specimen}/t_{meanstrand}$). A Matlab program discretizes each in-plane layer into partitions. The partition size ($1/20^{th}$ of strand length) is much smaller than individual strands to maintain continuity of material properties across partitions and to avoid the definition of an RVE. Strands with random orientations are generated and placed at random locations within these partitions on each in-plane layer as per the strand size (Figure 4-3.a). As the volume of the strands is unchanged, the reduction in the strand thickness is to be compensated for by the dilation of the strands in the transverse-to-fibre directions (Figure 4-3.b). The dilation factor ($W_{dilatedstrand}/W_{originalstrand}$) is computed and the strands are dilated in the model as per the dilated strand width ($W_{dilatedstrand} = W_{originalstrand} \; x \; t_{nominalstrand} / t_{meanstrand}$). Figure 4-3.c and Figure 4-3.d show panel surfaces of low and high strand dilations. Resin properties are assigned to the partitions plies that are unfilled by the strand dilations. From this larger model, model specimens of widths equal to that of test specimen widths are chosen to replicate the way the test coupons are trimmed from an actual plate. Figure 4-4 shows the variation of longitudinal stiffness within a model specimen. The fraction of resin rich areas calculated in a test specimen from the model is about 2-2.5%. Tape reinforcements are added to the specimens at different positions to simulate the hybrids. The model specimens comprising of partition laminates are now subjected to a 3-point bending scenario. The interlaminar shear stress and bending stress distributions are computed using Equation 4-2 and Equation 4-3 at the specimen mid-span.

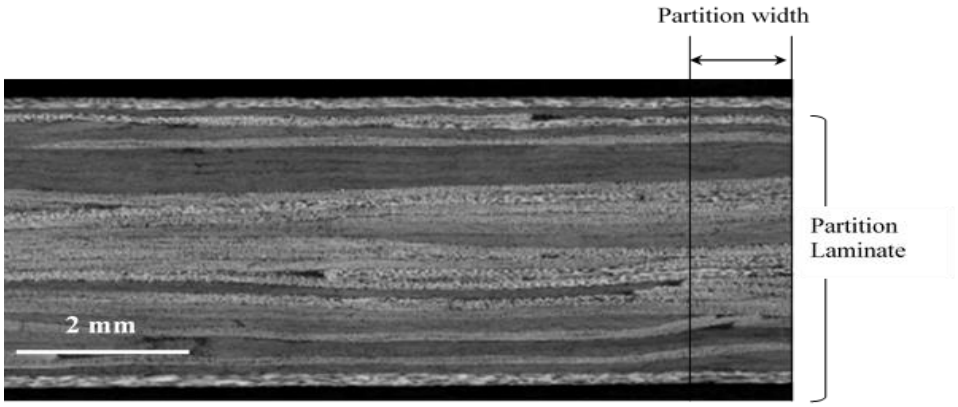

Figure 4-2: Cross-sectional micrograph of a Tapes-ROS-Tapes specimen

In this work, a realistic way of dilating the strands is included to compensate for the change in strand thickness. Scaling of thickness is eliminated and continuity of strands across partitions is maintained. The model uses a stochastic procedure in conjunction with analytical formulas and eliminates the need for complex finite element analyses. However, the model assumes planar strand arrangements and ignores the effect of strand waviness and the presence of matrix between the strand in-plane layers, thus, slightly over estimating the behaviour. While the initial strand arrangements and the flow could induce strand out-of-plane waviness in ROS parts, higher part thickness and hybridization reduce the strand waviness [13]. Strand waviness is analogous to ply waviness that results in interlaminar normal and shear stresses causing pre-mature failure [123]. The contribution of the residual stresses, edge effects and roller stress concentrations are not considered. A defect-free microstructure is assumed due to the low void content.

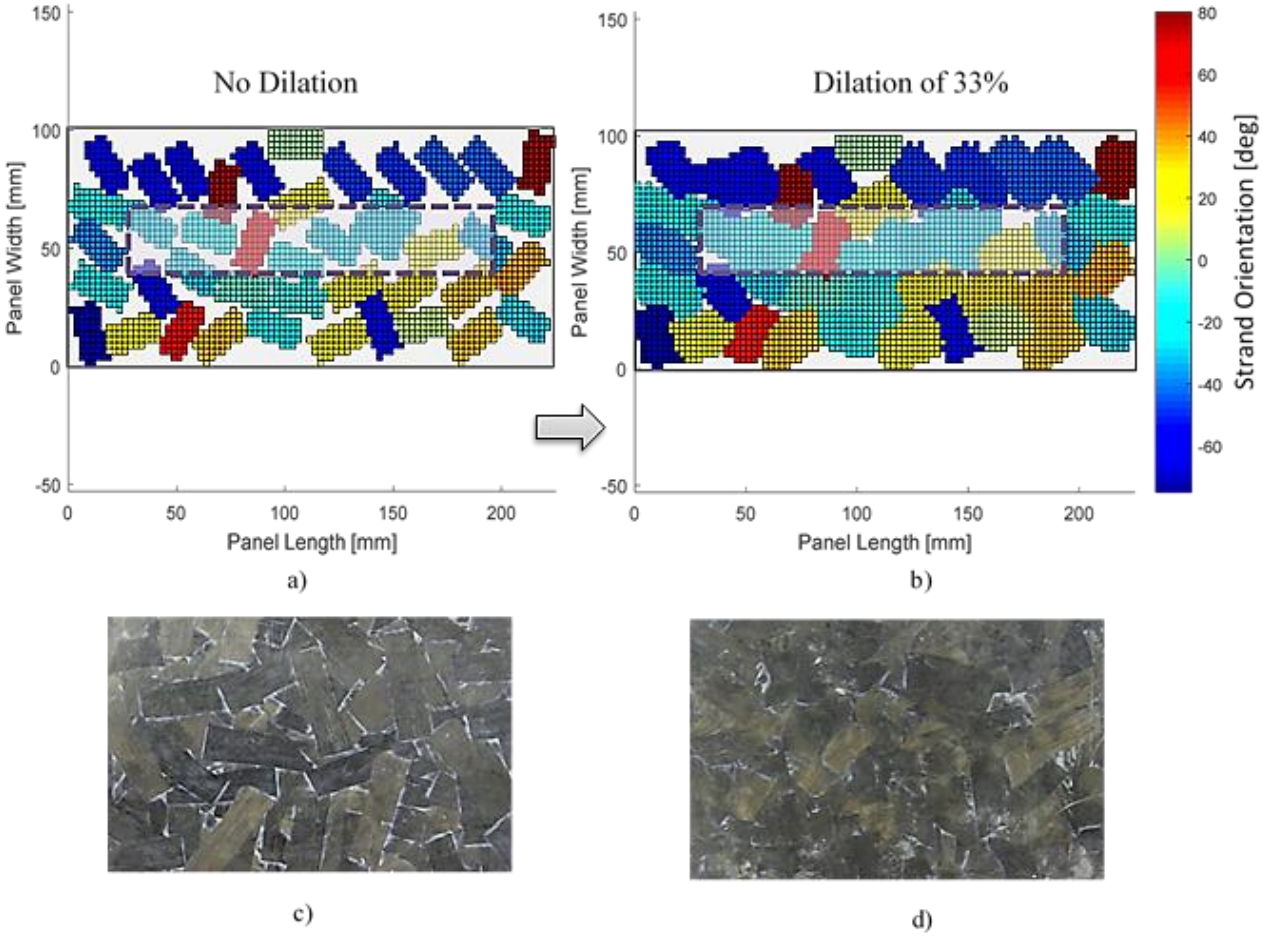

Figure 4-3: a) Top view of an in-plane layer without strands dilation; b) Top view of an in-plane layer with strands dilation; c) Top view of a ROS panel with low strand dilation; d) Top view of a ROS panel with high strand dilation

4.1.5 Results and Discussions

Experimental results

Load-displacement curves

Typical load–displacement curves of ROS and hybrid configurations of 3 mm thickness are shown in Figure 4-5.a. The responses of all the curves are linear in the early stages of loading, and non-linear towards the later stages attributed to the gradual failure of ROS phase. The curve for R3 (ROS material with 3 mm thickness) is characterized by several load drops. As the load increases, weaker spots in ROS develop cracks or delaminations. The staggered pattern,

however, resists the crack propagation causing load redistribution. On further loading, the weakest delamination develops as the critical failure. In most of the specimens, towards the end of the load-displacement curve, interlaminar failure has been observed with or without flexural failures accompanied by noticeable load drops. ROS-Tapes-ROS and Tapes-ROS configurations exhibit similar load drops as that of R3, towards the end of the curve. As expected, the stiffness of R3 is the least and the T-R-T is the highest. The T-R-T configuration adds to the bending stiffness of the specimen with the tapes placed on either side of the ROS material. T-R has a higher stiffness compared to the R-T-R hybrid.

Failure characteristics

Mixed-mode failures (i.e. tension, compression, and delaminations due to interlaminar shear) are observed in specimens, thus complicating the task of precisely recognizing the failure mode that caused the onset of damage. Each of the failures is carefully examined along with the load-displacement curves and strengths with dominant interlaminar failure modes have been reported. Among the benchmark laminates Cross-ply and Quasi-isotropic laminate groups demonstrate clear delaminations due to interlaminar shear. Angle-ply laminate group demonstrated interlaminar shear failures accompanied by inelastic stability modes. As the thickness of AP was lower than the ASTM standards, the results are not reported. Pure R3 specimens exhibited both flexural and interlaminar dominated failures. Among the hybrids, all the T-R-T configurations showed clear interlaminar failures in the ROS phase. T-R-T provides forced symmetry of the specimen and promotes the failure within the ROS phase. While the shear dominant failures are caused around the neutral axis, the asymmetry within the ROS phase shifts the neutral axis. R-T-R showed mostly clear interlaminar with secondary flexural failures originating from the interface of the ROS and the laminate. The waviness of the laminate group induces out-of-plane

stresses that add to the interlaminar shear stresses. T-R showed a mix of interlaminar and flexural failures but fewer than those of R-T-R. No noticeable failures were observed under the rollers. Figure 4-5.b represents images of various configurations with their typical failures.

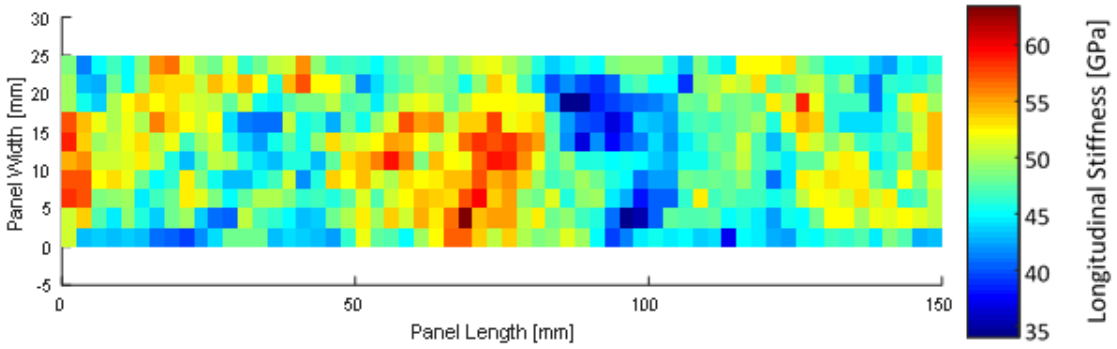

Figure 4-4: Longitudinal stiffness of a ROS specimen obtained using classical laminate theory on partition laminates (low and high modulus patterns on the plots are larger than the partition size)

Strength comparison

Figure 4-6 compares the strengths of test configurations normalized with the mean SBS strength of R3. The strength of R3 is like that of QI, while the variability of R3 is much higher. The strength of CP is about 10% higher than QI. Among the hybrid stacking configurations (i.e. T-R-T, R-T-R and T-R), T-R-T has the highest apparent interlaminar shear strengths that surpass their parent laminates demonstrating a dominant positive synergy. The reasons for such a synergy can be attributed to the improved load sharing between the phases and will be explained in the subsequent section. Among the various thickness ratios, the properties of 20/80 hybrids are the highest representing improvements of 25% in the T-R-T and 7% in the T-R configurations. R-T-R configurations in all the hybrids demonstrate high variability and lower properties than pure ROS specimens due to the waviness of the laminate group. Further, QI-R hybrids demonstrate an increase in the SBS strength only in the T-R-T stacking. T-R-T stacking of AP-R configuration demonstrates strengths similar to that of QI and ROS. In this research, the extent of synergy is

quantified by the deviation from the highest SBS strength of the parent groups that form the hybrid. Quantifying the synergy with reference to RoM is inappropriate under interlaminar behaviour, as the failures are dominated by the matrix. From Figure 8, we observe that all the T-R-T configurations exhibit a positive synergy of about 20-25% when compared to the SBS of the CP and QI laminate groups, primarily due to improved load sharing among the phases. While, a negative synergy of 20-25% is observed for all the R-T-R configurations, T-R and R-T configurations mostly exhibit positive synergies. Thus, we can observe that the SBS is a strong function of the hybrid stacking sequence. It is to be noted that only six specimens for each configuration were tested due to the material availability and processing limitations. Although this pilot study suggests improvement potential based on the phenomenological behaviour, a higher number of specimens are needed for statistically conclusive results.

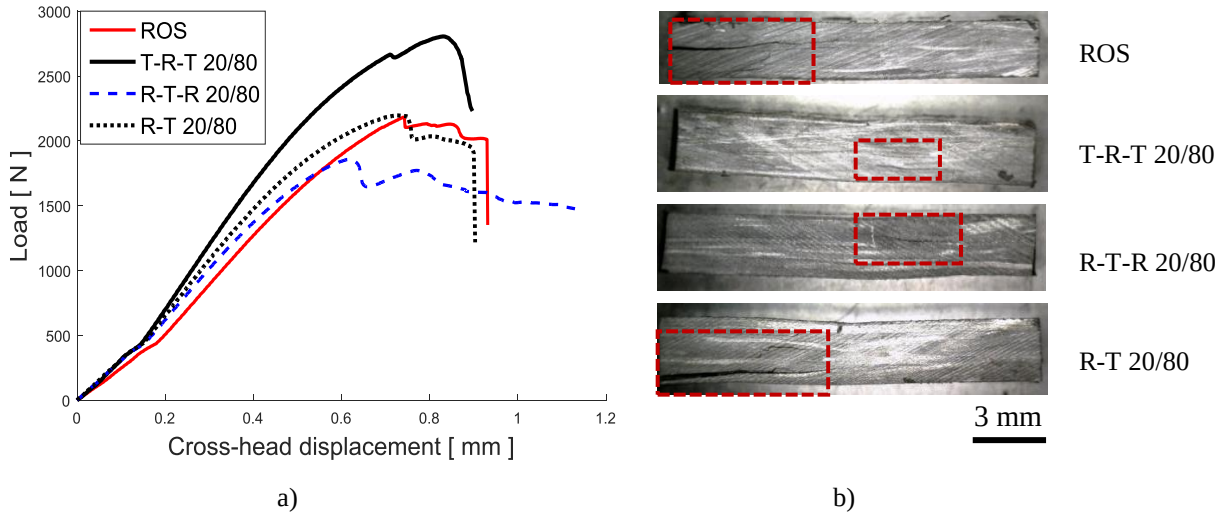

Figure 4-5: a) Typical load vs. displacement curves of selected configurations; b) Interlaminar failures of selected test configurations at around neutral axis of the specimens

Modelling results

Figure 4-7 compares the shear stress distribution of standard laminates with the R3 specimen. All the stresses are normalized with respect to the shear stresses in an equivalent homogeneous beam. An unsymmetrical layup in the R3 specimen shifts the location of the neutral axis along the thickness direction and changes the location of the maximum shear stress. CP exhibits the least maximum shear stress while R3 the maximum. Figure 4-7.b compares the shear distributions of R3 and the hybrids with the same thickness. The T-R-T configuration induces more symmetry into the specimen and forces the neutral axis to be closer to the mid thickness of the specimen. T-R-T demonstrates the least max stress behaviour while R-T-R changes the neutral axis position.

Figure 4-7.c compares the bending stress distributions of selected hybrid configurations. In the T-R-T configuration, the maximum bending stress in the ROS phase is alleviated by the laminate group. The bending stiffness of the outer tape layers is much higher than the ROS phase in the T-R-T. This causes a higher load sharing in the laminate layers compared to the ROS phase relieving some bending loads in ROS thus causing failures dominated by interlaminar shear than bending. This load sharing among the hybrid architectures enhances the short beam shear strength. The T-R configurations also demonstrate this synergistic load sharing. The R-T-R configuration demonstrates least strength as the stresses due to bending are much higher in the ROS compared to those of the other configurations. Further, the waviness in the centrally placed laminate group can trigger increased interlaminar stresses causing premature failure at the interface of the laminate and ROS phase, which cannot be captured by the model.

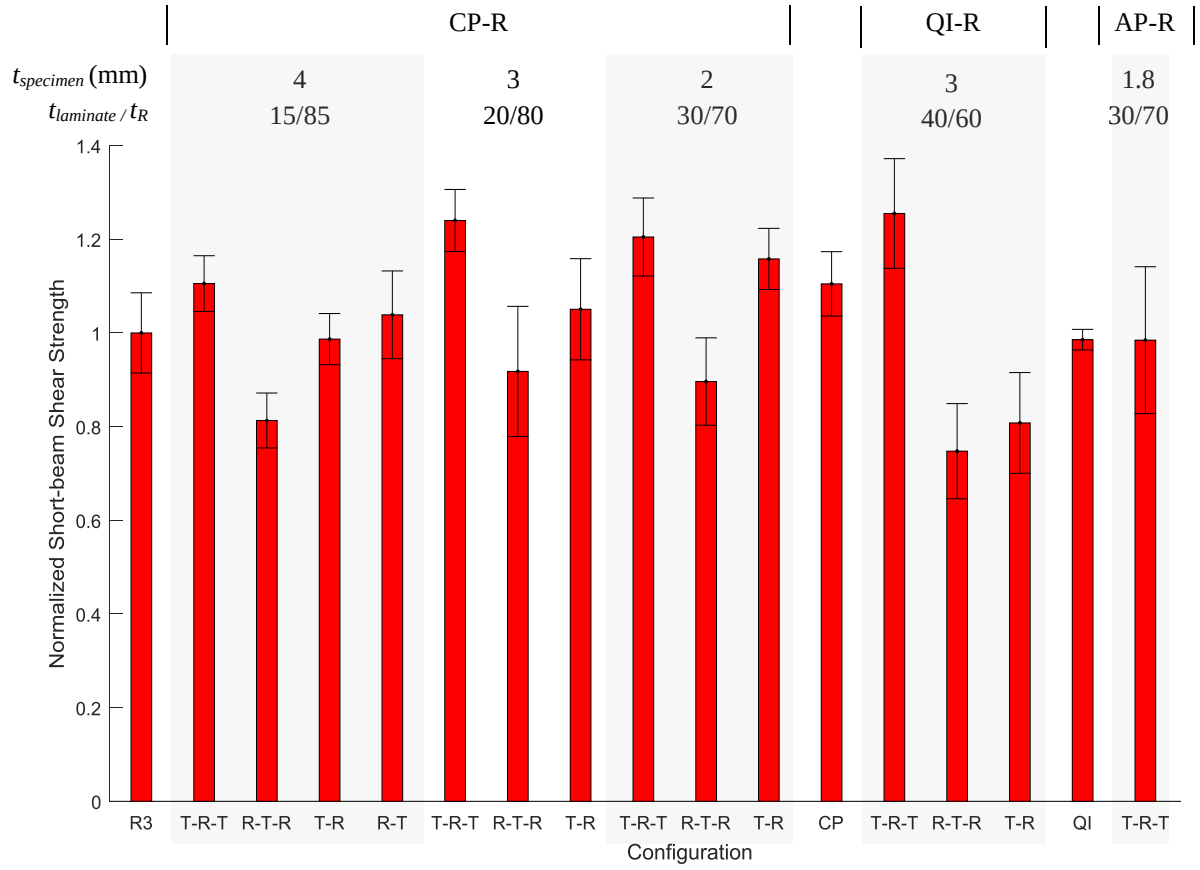

Figure 4-6: Experimental short-beam shear strength comparisons for all the test configurations

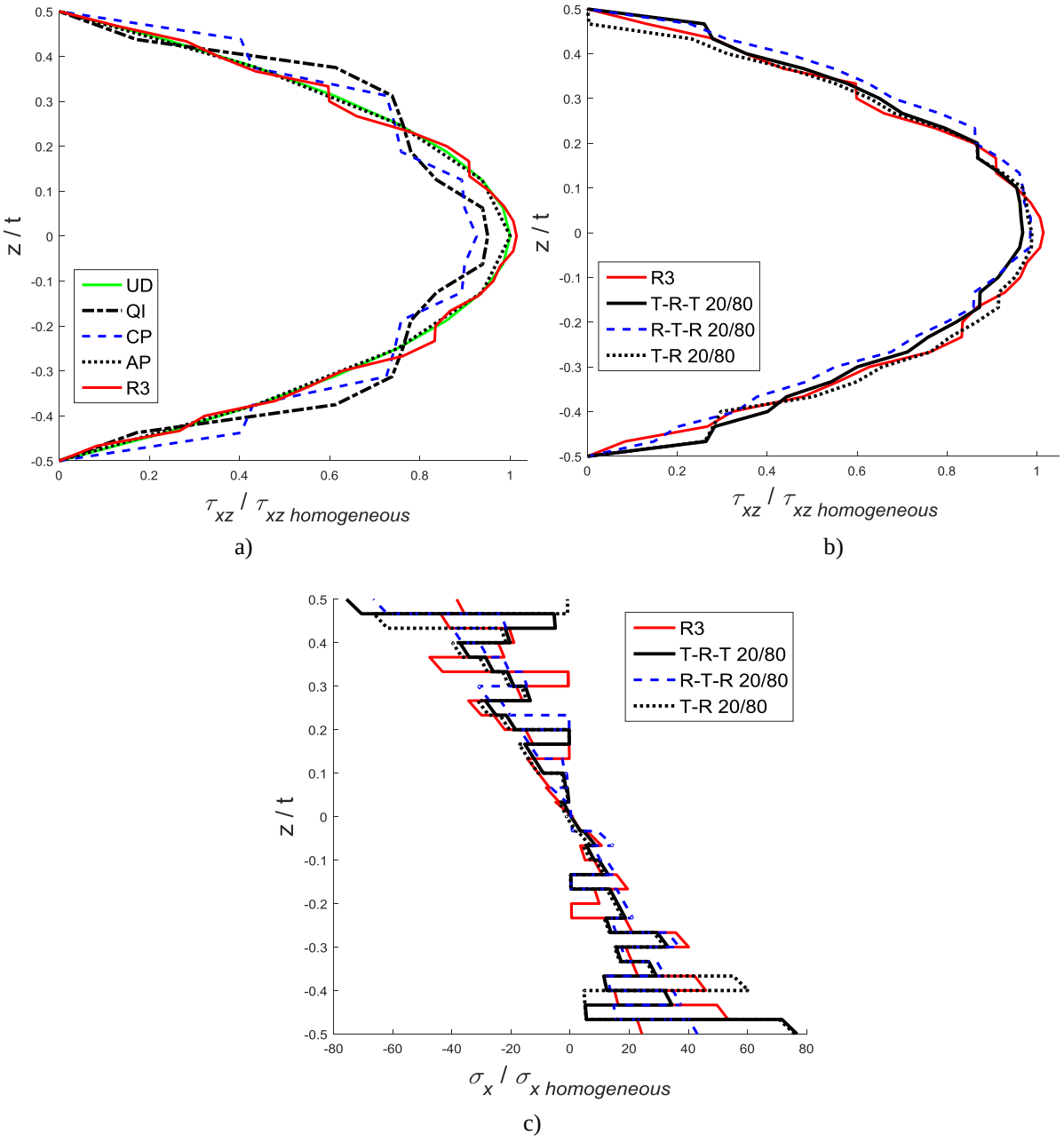

Figure 4-7: a) Theoretical interlaminar shear stress distributions of base groups (UD, QI, CP and AP) at the mid-span of the model specimen; b) Theoretical interlaminar shear stress distributions of selected hybrid configurations; c) Axial stress distributions of selected hybrid configurations due to bending load

The maximum shear stress in each configuration is first normalized with the maximum shear stress in a homogeneous specimen, to eliminate the effect of the dimensions, and is called the normalized shear factor ($A = \tau_{xz\ max\ homogeneous}/\tau_{xz\ max\ specimen}$). This factor is analogous to the safety factor in shear, and a higher value of the shear factor represents a lower value of maximum shear stress in the specimen. Normalized shear factors are again normalized with respect to the shear factor obtained for the R3 configuration to obtain the relative shear factors ($B=A_{configuration}/A_{R3}$). The relative shear factors represent the shear stress levels of the configurations relative to R3 specimens. Thus, a higher value (>1) of relative shear factor represents a lower value of maximum shear stress in a configuration compared to the R3 configuration. A similar approach is followed to obtain the normalized bending factor (C) and relative bending factors (D). However, the bending factors utilize the maximum bending stresses in the ROS phase in a hybrid specimen, and not the maximum bending stress in the entire specimen, as the laminate group is less prone to failures due to bending loads compared to ROS. Further, the relative stress factor, a ratio of relative bending factor to that of relative shear factor ($E=D/B$) is obtained. A higher value of relative stress factor signifies that the specimen has a lower maximum bending stress in the ROS phase compared to the maximum shear stress. Five trials are performed to arrive at the mean and standard deviations of the relative shear, relative bending and relative stress factors for all the configurations and are plotted in Figure 4-8.

Relative shear factors of CP and QI exhibit 8% and 4% higher values respectively, compared to the R3 configuration. These are about the same magnitude as that in the experiments. The modelling predicts a higher value of relative stress factor for AP than the experiments and cannot be compared directly as the failures in the experiments for AP was dominated by inelastic failure modes. Shear factors in the ROS phase depend on the strand orientations, unsymmetry in the

partition and the resistance to the crack path. Relative shear factors in hybrids show that T-R-T can carry higher or almost equal shear stresses compared to R3. T-R carries lower shear stresses than R3 while R-T-R carries least stress. Similarly, the relative bending stress factors demonstrate that the bending stress levels in the ROS phase are much lower in the T-R-T, then the T-R and highest in the R-T-R configurations. Further, with an increase in the ratio of tapes, a reduction of stress levels can be observed, owing to the increase bending stiffness of the laminate group. Six simulations were considered per test configuration.

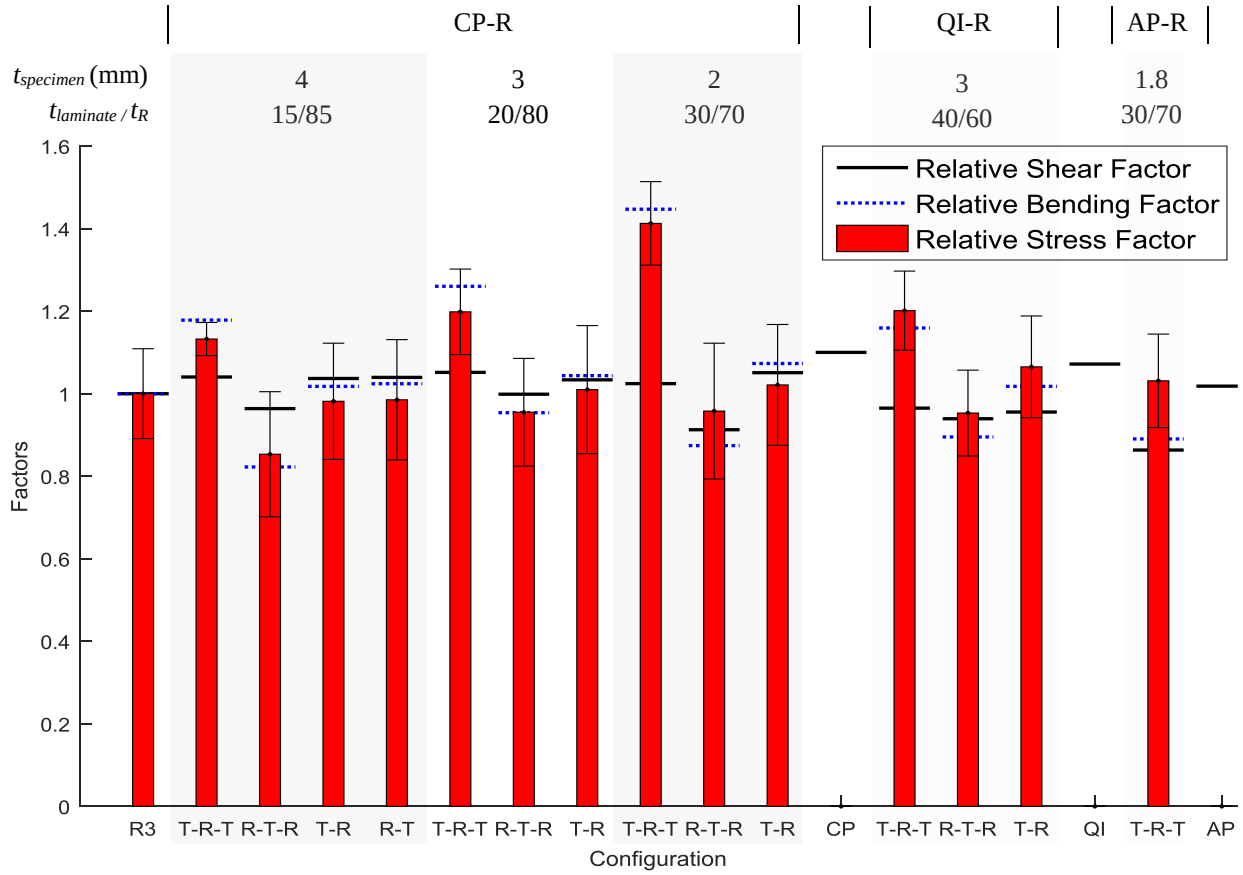

Figure 4-8: Relative Shear, Bending and Stress factors for the test configurations – comparison

The failure initiation in a ROS phase could be either due to shear or due to bending and the absolute strength of the specimen depends on the shear and bending strengths. The relative stress

factor (a ratio of the bending stress levels to that of shear stress levels in ROS) is a parameter that can be used to quantify the relative behaviour among configurations. Laminate groups in the hybrid specimens resist more bending and allow the failure in ROS to be predominantly interlaminar driven, based on the hybrid stacking configuration. The final failure of the test specimens is governed by the bending and shear stress levels compared to the allowables. A comparison of the relative stress factors of the hybrid configurations follows the experimental trend. For example, T-R-T 15/85 demonstrates an increase of about 11% compared to the ROS phase in the experiment, and the ratio from the relative stress factor from the model demonstrates about 12%. Similar reduction in values of about 20% is observed in R-T-R 15/85 in experiments and about 11% in the model. In other words, the model slightly overestimates the improvements in stress factors mostly in the cases of R-T-R and T-R, which can be attributed to the assumptions of no strand and ply waviness in the model. With the decrease in the thickness of the ROS phase, strand waviness increases and causes waviness of the laminate group. Thus, the model predictions for T-R-T at 30/70 overestimate the actual experimental behaviour. Similar comparisons are found in all the configurations within reasonable deviations. Increased synergies are obtained with an increased stiffness difference between the ROS and the laminate groups. Thus, a known behaviour of standard laminate such as a CP or QI can be obtained by testing and a predictive model based on a strand placement procedure is adequate to obtain reasonably accurate estimations of both qualitative and quantitative behaviour of the configurations relative to each other, despite the combined stress state in the specimens. The extent of synergy in hybrid configurations can be estimated based on the relative stiffness differences between the phases calculated using the model. It should be noted that the stress levels in the ROS phase are being

compared across all the configurations as the predictive models for interlaminar strengths of ROS do not exist.

4.1.6 Conclusions

The interlaminar shear behaviour of ROS and their hybrids is explored in this work. The short beam shear test method as per ASTM D2344 is chosen for relative comparisons despite the complex stress state in short beam shear test specimens. Experimental results demonstrate that the Tapes-ROS-Tapes configurations have the highest strengths, followed by Tapes-ROS and ROS-Tapes-ROS configurations. The R-T-R configuration demonstrates lower strength than the pure ROS specimens. The most interesting observation is the synergies in T-R-T configurations that exhibit higher properties of up to 25% than both of their parent constituents. This synergy is attributed to the improved load sharing among the phases. R-T-R configurations demonstrate a negative synergy with losses up to 20-25% in strength. Overall, the properties of T-R-T configurations are better than the parent materials, across all the laminate groups and thickness ratios.

A semi-empirical model for the simulation of ROS and their hybrids has been developed based on a stochastic strand placement procedure in conjunction with analytical expressions for interlaminar shear and bending stress distributions, for a three-point bending loading case. Using the model, the interlaminar and the bending stress variations across the specimen thickness are obtained. As the short beam shear test specimens are under a combined stress state, the shear and the bending stresses are compared. Graphs show that the T-R-T configuration alleviates the maximum bending stress in the ROS phase leading to an improved load sharing. Further, the model successfully captures the relative behaviour of the configurations and the extent of

synergy in various hybrids, with reasonable accuracies. The model uses the ratio of the bending to the shear stress levels in configurations relative to that of the stress levels ratios in ROS to predict the relative behaviour and synergies. The model exhibits a potential to reduce testing effort by providing relative behaviour of ROS-hybrids in reference to a few standard tests of benchmark laminates.

Chapter 5

Part Level Studies

5.1 Experimental Work on Stiffened Panels of ROS-Hybrids – Manuscript 4

Flow-control and Hybridization Strategies for Thermoplastic Stiffened Panels of Long Discontinuous Fibres

Abstract

The current research aims at mitigating the flow-induced manufacturing issues (strand waviness and swirling of strands) encountered in complex parts of randomly oriented strands (ROS), through the hybridization of ROS with continuous fibres, while emphasizing the ease of manufacturing and repeatability. Three hybridization strategies are proposed for T-stiffeners that represent the generalized intersecting junctions of stiffened panels. The strategies include: flow-control element (FCE), flange reinforcements (FR) and rib reinforcements (RR). A quantitative assessment of pull-out strengths of five T-stiffener configurations is made. FCE improves the

strand flow at the junction, reduces variability and enhances the pull-out b-basis design allowable by about 24%. A quasi-isotropic laminate as FR with an FCE produces 12.5% pull-out strength improvement. RR causes reinforcement delamination from the ROS part, dropping pull-out strength by about 6%. A transient heat transfer analysis of the tooling set-up was simulated using finite elements to devise a preferential cooling strategy that minimizes porosity in ROS panels with T-stiffeners.

Keywords: Long Discontinuous Fibres, Randomly Oriented Strands, Compression moulding, Flow-control, T-stiffeners, Stiffened panels

5.1.1 Introduction

ROS parts/panels have found limited use in load carrying and complex shaped aerospace structures such as brackets and stiffened panels, despite their excellent formability characteristics. Two critical manufacturing defects that limit the structural performance of compression moulded ROS parts/panels include: out-of-plane waviness of strands (Figure 5-1.a) and swirling of strands (Figure 5-1.b) at intersecting junctions of the panel and their stiffening features. Stiffening features in a panel primarily resist the out-of-plane and axial loadings while the panel itself resists the shear load. Pull-out loading is the critical loading scenario on such stiffening features in stiffened panels. T-stiffeners comprising of a flange and a web in construction, represent the most generalized stiffening feature. Interlaminar properties such as the interlaminar shear strength (ILSS) and interlaminar tensile strength (ILTS) are crucial in determining the pull-out strength of the T-stiffeners. Composites are weaker in the out-of-plane directions compared to their in-plane directions. While ply waviness leads to an increase of interlaminar stresses and a decrease of in-plane properties [123], a similar analogy can be applied to strand waviness in ROS parts; strand waviness decreases the in-plane properties due to the

introduction of interlaminar stresses [13]. However, a marginal increase in the interlaminar shear strength has been observed with an increase in strand waviness by Selezneva et al. [12] and no systematic studies have been carried out on the interlaminar tensile strength of ROS. Swirling (Figure 5-1.b) is a manufacturing defect resulting from a resistance to the strand flow direction. Swirling is mostly observed at the junctions of geometric features when subjected to multiple flow masses. Swirling results in significant variability of both in-plane and out-of-plane properties, directly affecting the pull-out load capacity of the part. Component level tests [35] are essential to obtain the pull-out strength allowable as the T-shape is subjected to a complex stress state at the junction region that is highly anisotropic in nature. Further, based on the thermal distribution in the tooling and the part, surface defects such as porosity could arise. It occurs when the temperature field is not uniform, uneven crystallization causes loss of pressure on the part. The tooling set-up used in the study can cause a loss of pressure in the rib when the flange crystallizes. Surface defects could be critical in a compression loading scenario of the part reducing its properties by almost 25% in ROS specimens [137]. Further, these defects could act as crack initiation locations, thus necessitating a thorough thermal analysis and experimental validation of the heating, dwell and cooling phases of the compression moulding process. Thus, it is crucial to obtain a defect-free junction and a defect-free surface in an ROS based T-stiffener before assessing its pull-out load capacity.

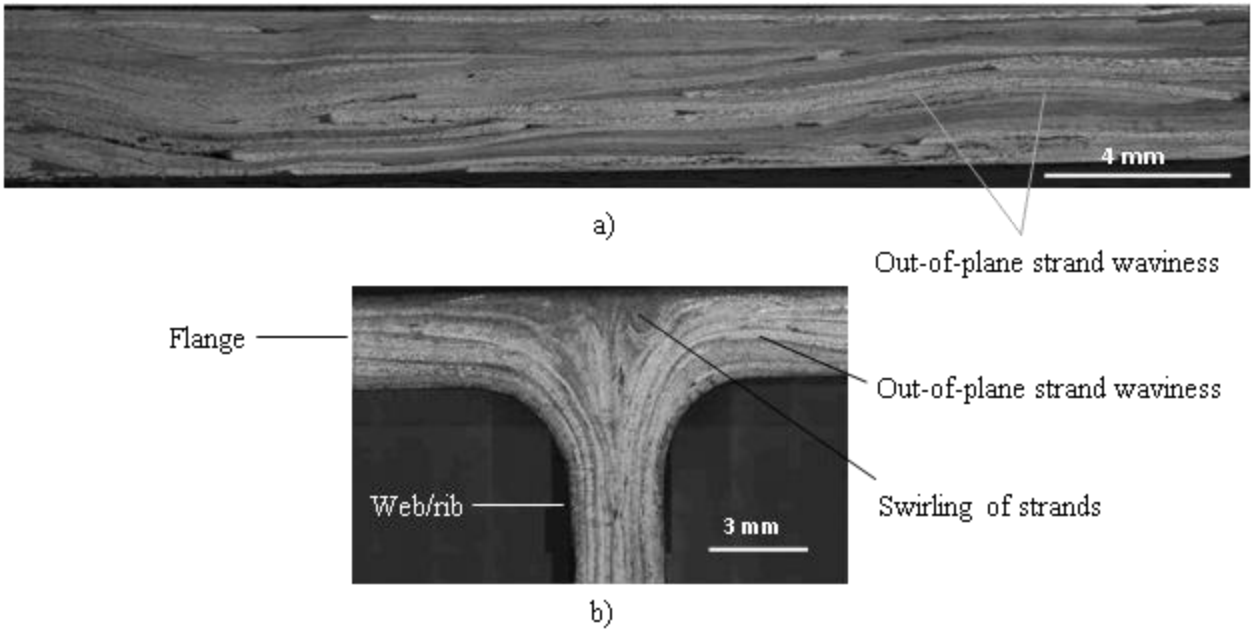

Figure 5-1: a) Micrograph of ROS flat specimen fabricated with 25.4mm x 12.7mm carbon/PEEK strands showing out-of-plane strand waviness; b) Micrograph of ROS T-stiffener with swirling and out-of-plane strand waviness at the junction of web and flange

Researchers have reported improvements in the mechanical behaviour of discontinuous fibre composites such as ROS by hybridization with continuous fibre architectures, at the coupon level. Continuous fibre reinforcements such as unidirectional tapes/woven fabrics of the same material as the discontinuous architecture were considered [13, 33, 71]. Strand waviness, hence the variability, has shown to be reduced on flat panels by the addition of laminate groups [13]. The reduction in the strand out-of-plane waviness was attributed to the accommodative behaviour of the 90-degree plies. At the part level, Wakeman et al. [1] proposed the use of hybrid fibre architectures for trade-off solutions of formability and structural performance and fabricated a plate made of continuous fibres and ribs of short fibres co-moulded as one-part. Leblanc et al. [51] enhanced the properties of T-stiffeners fabricated with ROS by adding cross-ply layers on the flange/base panel of the stiffener. However, the strand flow into the rib cavity

caused excessive undesirable waviness of the flange laminate. In the literature, hybridization of composites refers to the combined use of two distinct materials; usually high elongation-low strength material with low elongation-high strength material to improve the ductility response of the low elongation material [22] while exploring the synergistic behaviour called the 'hybrid effect'. While positive synergistic behaviour was demonstrated in hybrids of ROS and continuous fibre laminates [13], hybridization in the current context refers to the use of reinforcement strategies to enhance the structural performance of ROS based stiffened panels while retaining its formability characteristics.

In the literature, researchers of hybrid and non-hybrid ROS parts [15, 49, 51, 138] seldom dealt with the mitigation of strand waviness and swirling issues that cause significant variability in the mechanical behaviour. In the current research, hybridization strategies are proposed to address these critical issues in ROS based parts. The strategies are implemented and validated with experimental testing of representative T-stiffeners. The effects of these strategies on the stiffness, strength, failure modes and variability are quantified. The pull-out strength test results are compared with conservative estimates of the pull-out strength of quasi-isotropic L-stiffeners using analytical formula and experimental data from literature.

5.1.2 Hybridization strategies

Three hybridization strategies are proposed: flow-control method, flange reinforcements (FR) and rib reinforcements (RR). The flow-control method channelizes the flow of strands using a flow-control element (FCE) (Figure 5-2.a). A pyramidal stack of unidirectional tapes (with fibres in the rib length direction) constitutes the FCE. Appendix B describes a typical FCE in detail with the design procedure. The flow-control element facilitates the strand flow inside the rib

cavity and around the junction as the 90º tapes within the FCE provide an accommodative sliding interface to the flow direction. The presence of 0° plies in the flow-control element enhances the axial stiffness in the depth direction of the junction, which could be regarded as a secondary benefit. Elements analogous to an FCE have been used in industry in T-stiffeners fabricated with continuous fibre composites, known as a 'Radius Filler' or a 'Noodle' [139, 140]. The noodle's purpose is to fill the junction cavity and to provide dimensional stability to the plies when subjected to consolidation pressure. The use of noodles in continuous fibre composites however does not promote the flow and differs from an FCE in the design calculations. Consequently, the application of the flow-control method to short fibre or ROS composites is novel. Flange reinforcement (Figure 5-2.b), added in the form of a lamina or a laminate, is a hybridization strategy that can be regarded as a stiffening feature for the top surface of the T-shape flange. FR could also be regarded as a parent continuous fibre structure on which a stiffening ROS rib is 'grown' by compression moulding. Rib reinforcement strategy (Figure 5-2.c) involves the addition of lamina or a laminate on the ribs as a stiffening feature. It is important to note that all the reinforcements are co-moulded using compression moulding without any post moulding operations. The processing observations and the mechanical effects of the individual strategies and their combinations are quantified in the results section.

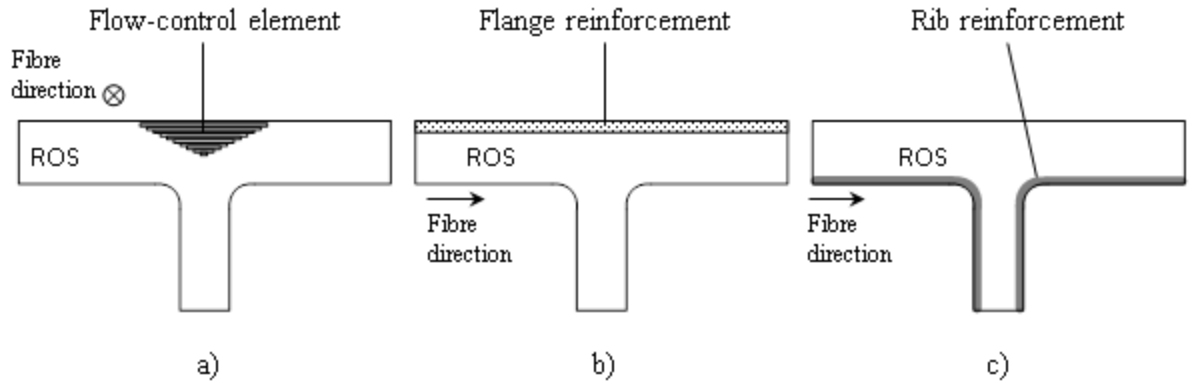

Figure 5-2: a) Flow-control element; b) Flange reinforcement; c) Rib reinforcement

5.1.3 Experimental work

Tooling and part geometry

The tool features two H-13 steel platens mounted on a 250kN MTS test frame, a picture frame and two moulding inserts that allowed forming of T-stiffeners (Figure 5-3.a). The platens are equipped with four 500W heating cartridges, controlled using two auto-tuning proportional–integral–derivative (PID) controllers. This control is achieved using two thermocouples (one for each platen), positioned between the two middle heating cartridges. The platens are air cooled by three channels each. Two 25mm thick 914 glass ceramic insulations separate platens and the loading set-up. The geometric dimensions of T-stiffeners are as shown in Figure 5-3.b.

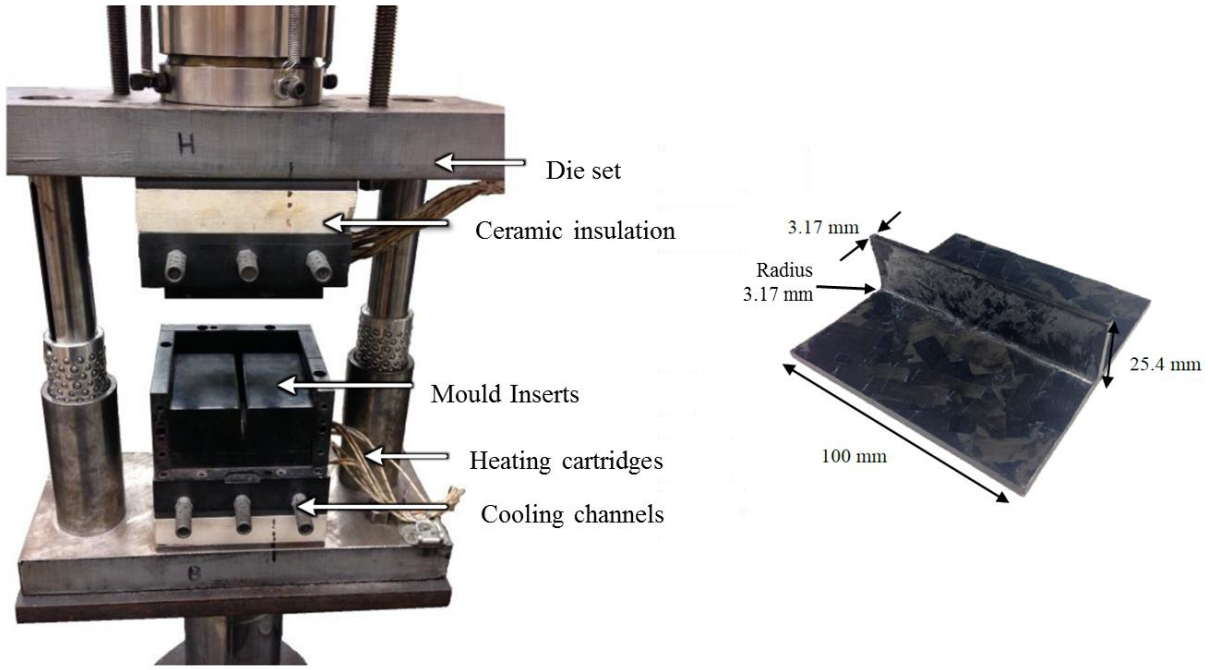

a) b)

Figure 5-3: a) Tooling set-up [51]; b) Geometry of the T-stiffener

Manufacturing

Carbon/PEEK strands of size 25.4mm x 12.7mm with a fibre volume fraction of 59% and a cured nominal thickness of 0.135mm are used. The strands are first placed in batches into the flat part (flange) of the mould such that the initial out-of-plane orientations are minimized. Before closing the mould the flow-control element is placed on top of the ROS and parallel to the span of the web (Figure 5-4.a). The flow-control element is tacked together using a heat gun and an additional strap of unidirectional ply is added for accurate positioning during the compression moulding. The processing parameters are as per Figure 5-4.b. During the low-flow compression moulding, the strands in the cavity begin to flow towards the rib cavity and consolidate under the influence of temperature and pressure. As the flow-control element is placed at the junction of two intersecting flow-fronts, the pyramidal stack of tapes channelizes the strand flow into the rib

cavity while changing its own shape to facilitate filling of the swirling prone region. Thus, a junction with no swirled strands and minimized strand out-of-plane waviness is expected. For the hybrid configurations, all the preforms are placed in the mould at the same time, consolidated and co-moulded without using any pre-consolidated panels. A major advantage of co-moulding is the time/cost reduction during the fabrication.

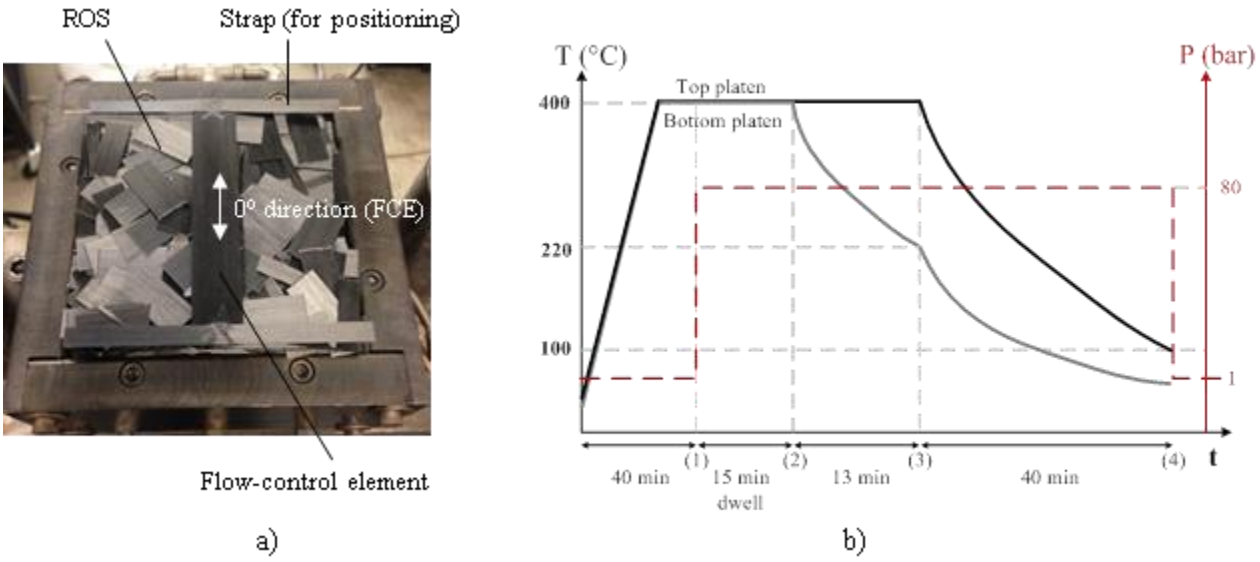

Figure 5-4: a) ROS and FCE before closing the mould; b) Process parameters: pressure (P), temperature (T) and time (t)

Test configurations - Pull-out strength testing

Five test configurations are chosen (Table 5-1) and six coupons for each configuration are tested. Configuration A comprises of pure ROS specimens for benchmarking of the results. In configuration B, a flow-control element (FCE) is added. Configuration C explores the benefits of adding a quasi-isotropic layup as flange reinforcement (FR) together with a flow-control element. This configuration also examines the extent of ply waviness in the flange induced by the strand flow. It is to be noted that the flow-control element in configuration C is smaller than

in configuration B due to the presence of the flange reinforcement laminate. In configuration D, two L-shaped 0° plies are initially placed in the mould cavity that forms the rib reinforcement (RR) after compression moulding. Configuration D also features a flow-control element. Configuration E has a combination of flow-control element, rib and flange reinforcements. The layup used in the rib and flange reinforcements is crucial to the stiffness, strength, and failure characteristics. For the flange reinforcement, a quasi-isotropic layup of $[0/90/45/-45]_s$ is considered, amounting to about 35% of the flange thickness. The plies for quasi-isotropic layup are also tacked together to make their positioning inside the mould cavity easier. Rib reinforcements are added to strengthen the rib in axial and bending applications and to reduce the overall strand waviness in the ROS phase. 0^o unidirectional tapes are selected as rib reinforcement plies and constitutes about 20% of the total rib thickness. The test matrix is thus designed to assess both the individual and combined effects of the hybridization strategies.

Configuration	FCE	FR	RR
A			
B	x		
C	x	x	
D	x		x
E	x	x	x

Table 5-1: Test configurations and hybridization strategies (‘x’ represents inclusion of the strategy)

Test method

Pull-out strength tests determine the resistance of a structure to out-of-plane loading and are mostly customized to the application. In real applications, the boundary conditions determine the

actual loading scenario and are complex to replicate. Nevertheless, test methods can be designed to represent conservative design allowables. For example, a roller loading configuration (Figure 5-5) is more severe in terms of the moment induced at the junction compared to a clamped condition. Thus, a custom pull-out test fixture with roller supports is developed and used. The geometry of the fixture is as shown in Figure 5-5. Part performance of all the test configurations is assessed by this custom pull-out test. For the mechanical testing, coupons are restricted by the rollers at the flange. The rib and the lower fixture are clamped using the gripped jaws of the tensile testing machine. The rib was pulled in displacement control until an overall displacement of 3mm; this displacement was limited by the spacer distance between the upper and lower plates. The maximum load capacity of the structure and the load-displacement curves are measured. The characteristics of these curves signify the onset of delamination and other damage behaviour.

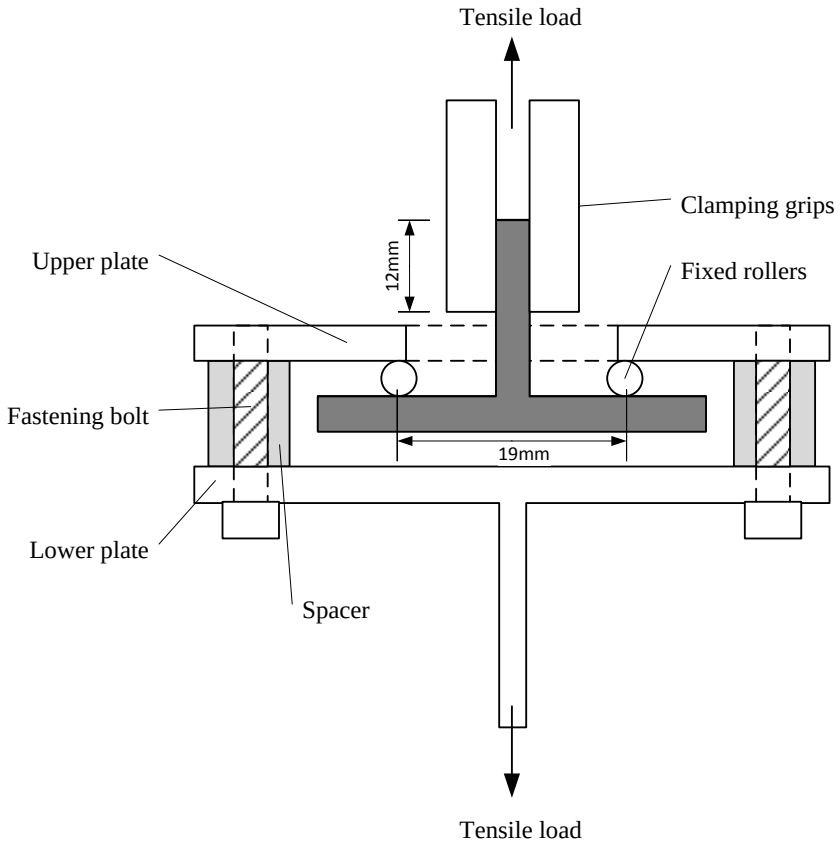

Figure 5-5: Pull-out test fixture

5.1.4 Tooling - Thermal distribution analysis

Thermal behaviour of the tooling – Simulation

The thermal behaviour of the tooling set-up involves complex interactions between the composite part, the mould and its cooling system. Controlling the thermal distribution through the tooling determines defect formation specifically at the surface and part porosities. The surface defects are the white surface porosities that typically appear due to the non-uniform shrinkage of the material at inadequate consolidation pressures [137]. To study the physical phenomena, a transient heat transfer analysis of the tooling set-up is performed using finite elements in ABAQUS/Standard on two tooling set-ups: flat plate and T-stiffener tooling. The objectives of the simulation are to obtain adequate dwell time, a steady-state temperature field in

the part and a preferential cooling strategy to minimize the formation of surface and part porosity. Thermal conduction in the tooling materials is characterized by material conductivity, density and specific heat. Manufacturer data and simple experiments are utilized to obtain the physical and thermal properties of the materials at various temperatures for use in the simulation (Table 5-2). Three physical interactions are modelled: contact conductance, convection and radiation.

Contact conductance between the parts was modelled to quantify the quality of each contact interface. A single value of conductance for all the steel-steel contacts is chosen, for simplicity and validated through experiments. For the composite material, which is anisotropic, different conductivity values in the through-thickness and in-plane directions were used. A high value of contact conductance for steel-composite contacts is assumed as the melted state of the composite facilitates efficient conductance at the interfaces. A non-uniform convection coefficient is implemented to consider the heating of the air throughout the channels, thus the non-uniform cooling of the platens. Heating cartridges are modelled as a uniform surface heat flux on the platen surfaces in contact with the cartridges. This heating flux is calculated to match a total heating power of 500W per cartridge during heating. Air flowing through the cooling channels is modelled as a fluid-structure thermal convection interaction. The average convection coefficient (h_o) varied linearly along the channels so that initial coefficient of $1.4h_o$ to a final coefficient of $0.6h_o$. This variation is calculated using an ABAQUS/CFD simulation of the cooling channel. As the conductivity of the composite is low compared to that of steel and the mould temperatures at the interface are of primary interest, constant thermal properties for PEEK/composites are assumed despite their phase changes during the process. Forced convection coefficient and the heating power are determined to match the temperature decrease during the experiment.

Surface radiation is the predominant heat loss when the tool is hot. It is given by:

$$R = AEk\,(T_{surface}^4 - T_{ambient}^4) \quad \text{Equation 5-1}$$

Where *A* is the area of the tool outer surface or the tool surface in contact with ambient air, *E* is the Emissivity, k is Stefan-Boltzmann constant, $T_{surface}$ is the tool surface temperature, $T_{ambient}$ is the ambient temperature. If we assume the whole tool surface is at 400°C, ambient temperature is 25°C and emissivity is 0.9, the radiated power to the ambient environment is approximately 500W. It is 1/8 of the maximum heating power. Surface convection with ambient air is a secondary heat loss, and becomes predominant when the mould cools down and is given by:

$$C = Ah(T_{surface} - T_{ambient}) \quad \text{Equation 5-2}$$

Where *C* is the Convection power, *h* is the convection coefficient. If we assume the whole tool surface is at 400°C, ambient temperature is 25°C and convection coefficient *h* is 10 W/(m^2-°C), we obtain a convection power of approximately 200W, a secondary heat loss.

Materials	Density (kg/m^3)	Thermal conductivity (W/(m-°C))	Specific Heat (J/(kg-°C))
H13 steel (At 25°C) [141]	7810	24	460
PEEK [142]	1320	0.25	1340
Carbon/PEEK, ROS in-plane [142]	1600	3.5	1340
Carbon/PEEK, ROS out-of-plane [142]	1600	0.95	1340
914 glass ceramic [143]	5600	2.8	460

Table 5-2: Thermal properties and constants used in finite element simulation

Contact conductance	W/(m^2-°C)
Contact between solid parts	1.50E+03
Steel – melted composite	1.50E+05

Convection coefficients	W/(m^2-°C)
Natural convection (external surface) [144]	10
Average Forced convection (cooling channels)	200

Radiation	
Stefan-Boltzmann constant (kW.mm^{-2}.˚C^{-4})	6.67E-17
Emissivity [144]	0.9

Heating power load (Surface heat flux)	kW/m^2
500 W/cartridge (heating phase)	136
165 W/cartridge (dwell phase)	45

The parts of the tooling set-up are discretized using 20-node quadratic heat transfer bricks (Figure 5-6.a). The cylindrical regions around the heating cartridges and the cooling channels are meshed using 10-node quadratic heat transfer tetrahedrons. For simplification, tight radii, small holes and screws are neglected. Stresses inside the mould are not considered, and the elements are non-deformable. Transient heat transfer analysis is used with time steps: 1s for the initial step, then automatic increments, with a maximum time step of 3 to 5 minutes. Two separate simulations are carried out for the heating and cooling phases. The cooling simulation uses results from the heating simulation as an input for initial temperature fields.

Thermal behaviour of the flat plate tooling set-up - Validation

In the simulation, the heating phase consisted of 500W power input in each cartridge until 400°C is reached at the control thermocouple locations. A constant power is induced to ensure temperature stabilization in the tool. This allowed validating the 15 minute dwell time used by Landry et al.[52]; this dwell period is sufficient for a steady-state temperature field (Figure 5-6.b) to be established in the tool. The cooling phase at a cooling rate of 10^{o}C/min was simulated to reproduce the experimental conditions used in [121]. The authors studied the flat plate tooling set-up and measured the temperature at 18 thermocouples positioned at the part surface during the cooling phase (Figure 5-6.c). By a simple trial and error approach, the proper heating power that would maintain the right cooling rate was determined to simulate the plate temperatures during the cooling phase. It was noticed that temperature gradients inside the composite part are significant, especially during the cooling phase. This is attributed to the composite material, which is a thermal insulator compared to H13 steel. Thus, large temperature variations in the through-the-thickness direction of the flange can be observed. Further, the part temperature decreases very abruptly at the flange corners. The main reason for this gradient is that although the plate was heated uniformly, the tool was cooled down from the sides, because of radiation and natural convection on the external surfaces. Possible ways of avoiding this would have been to insulate the sides of the mould. Figure 5-6.d compares the simulated temperatures at the thermocouples' positions with actual thermocouple data from [137]. The comparisons of the temperature gradient between simulation and experiment were within reasonable accuracy and could be greatly improved by simulating the PID controllers more accurately, by considering the change in the thermal conductivity of the composite throughout crystallization of the resin, by retrieving data at the exact coordinates of the thermocouples and by modelling phenomenon such

as material shrinkage. The finite element simulation for the flat plate tooling set-up thus was extended to simulate the tooling set-up for fabricating T-stiffeners.

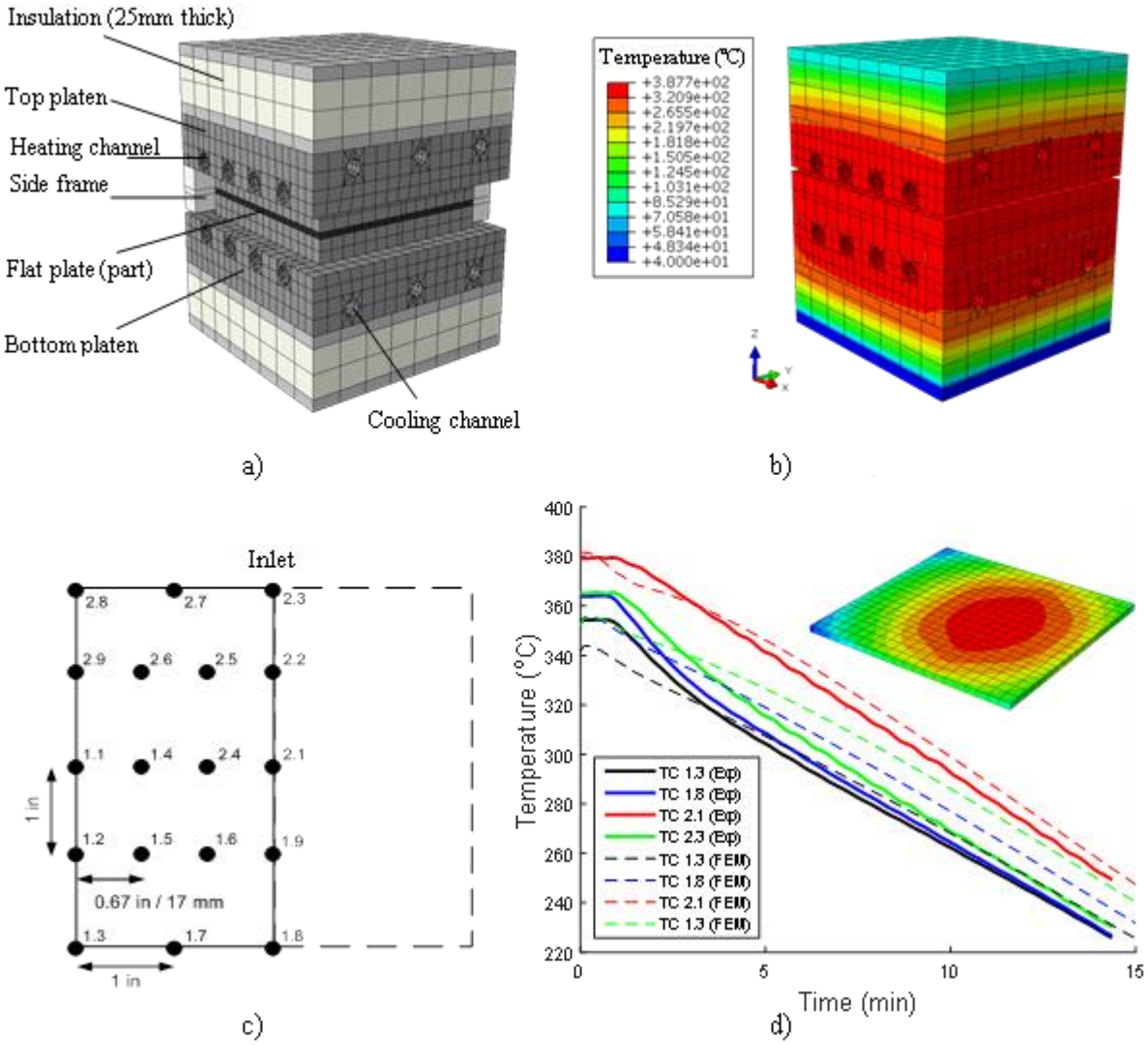

Figure 5-6: a) Finite element model of the flat plate tooling set-up (For clarity, forward side frames are not displayed); b) Steady state temperature distribution in the tooling; c) Flat plate thermocouple locations [137]; d) Experimentally measured thermocouple temperatures (Exp) vs. simulation (FEM) of controlled cooling of flat plate with an illustration of the temperature gradient in the flat plate

Thermal behaviour of the tooling set-up for fabricating T-stiffeners

The heating phase was simulated using the finite element model for the T-shape tooling set-up (Figure 5-7.a). The dwell phase of 15 minutes was verified to establish a steady-state temperature field in the tool (Figure 5-7.b). For the cooling phase, the objective was to determine a strategy that resulted in horizontally uniform temperatures, while allowing preferential cooling of the rib before the flange. Landry [52] identified this as the crucial criterion to avoid surface defect formation. If the flanges were too cool and crystallized before the rib, the latter would be relieved of the pressure from the mould by the crystallized flange and defects would occur in the rib. The mould design makes it difficult to separate flange and rib crystallization, because of the large thermal mass of the inserts. A preferential cooling strategy for the tooling set-up is devised and validated through experiments. To maximize the thermal gradient between the rib and the flange: bottom air cooling was switched on while the top of the mould was maintained at 400°C. When the bottom temperature reached 220°C, the heating was switched off, and the part was cooled down to 100°C for de-moulding (Figure 5-4.b). The finite element simulation showed that even if the thermal gradient between the control thermocouples is large, temperatures on rib surface and on the bottom of the flange remain close because of the large thermal mass of the inserts. However, since there is a strong temperature gradient through the thickness of the flange, it is difficult to define a ‘flange temperature’. Figure 5-7.c depicts the temperature gradient between the top surface of the flange and the tip of the rib. It is about 20°C as per the cooling strategy, ensuring that the rib cools prior to the flange.

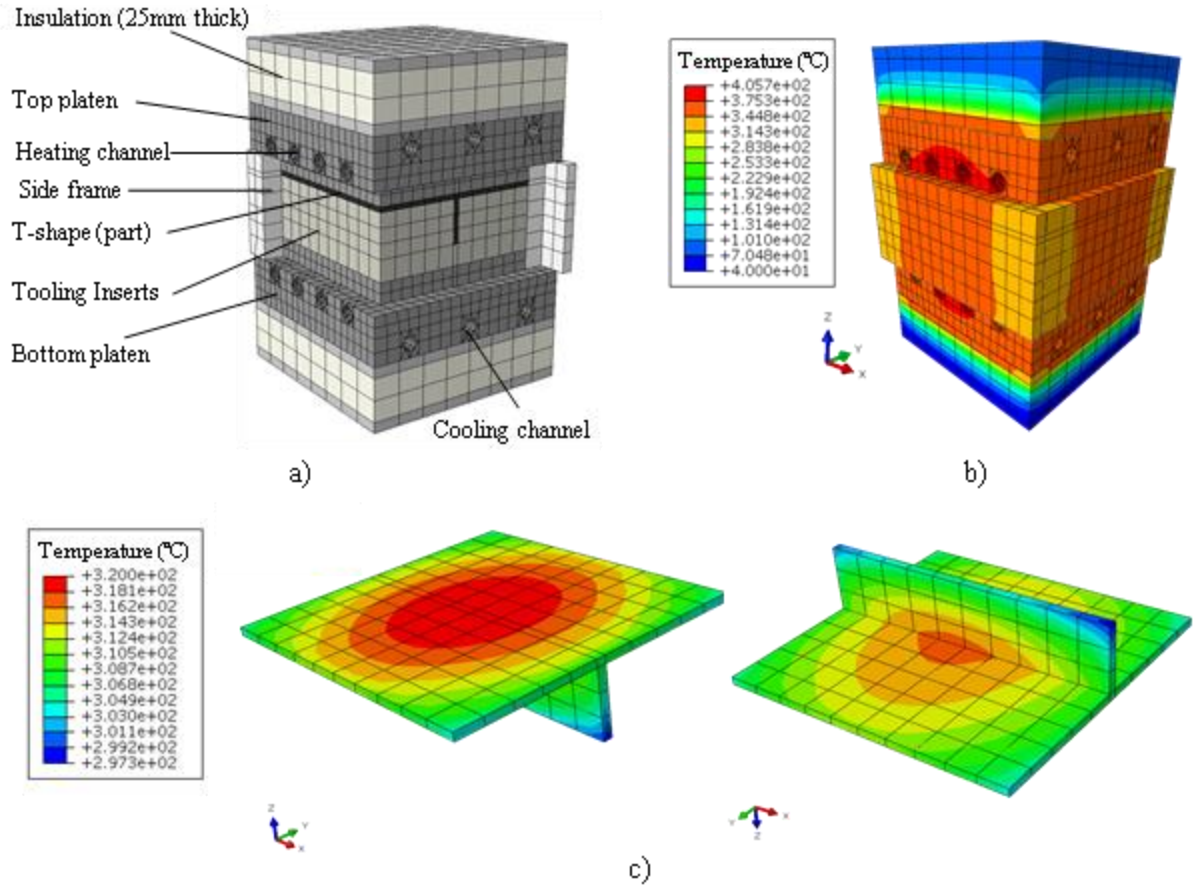

Figure 5-7: a) Finite element model of the tooling set-up (For clarity**,** forward side frames are not displayed); b) Steady state temperature distribution in the tooling with preferential cooling strategy; c) Temperature distribution across the T-shape during the cooling phase indicating a temperature gradient of 20°C between flange and the rib corners

5.1.5 Results and discussion

Processing observations

Micrographs of the junctions of T-stiffeners reveal swirling-free regions and minimized strand waviness (Figure 5-8). The 90° fibres of the flow-control element accommodated its shape to the strand flow with consistency regardless of the chosen configuration, FCE size and strand size thus proving the robustness of the flow-control strategy. Figure 5-8 also shows an additional layer of 0^{o} ply added on the flange proving that the flow-control element eliminates ply waviness

when added as flange reinforcements despite the number of plies. The flow-control element forces a directed flow of strands through the rib cavity thus eliminating knit lines at the junction. The flow-control element conforms to the shape of the cavity as per the design calculations of Appendix B. The flow-control element does not seem to have induced preferential orientation of the strands, as a close analysis of the micrograph reveals strands of various angles at and around the junction. The flow-control element was accurately implemented into one-shot compression moulding with minimal preparation. The mechanical benefits of the flow-control element are discussed in the subsequent sections.

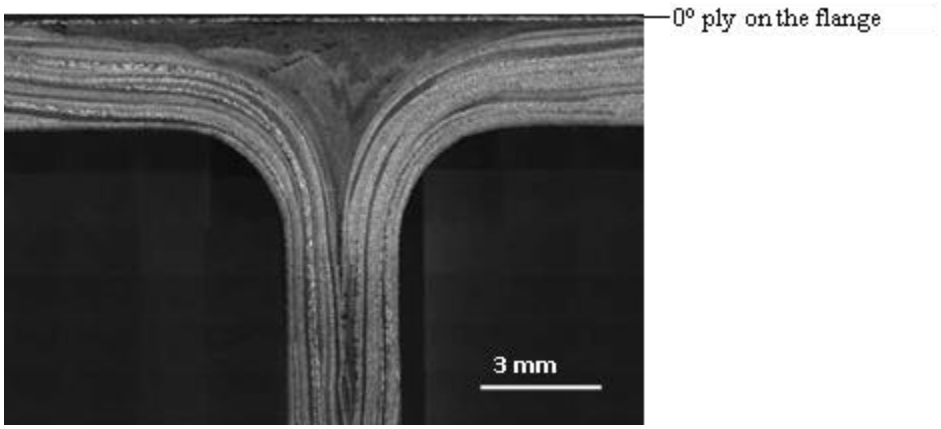

Figure 5-8: Micrograph of a flow-control element with a 0° ply on the flange

Pressures of about 80 bars ensure complete rib filling. The choice of the pressure value is based on the studies that determined the minimal processing pressure needed to obtain the filling of the rib for several strand sizes and processing temperatures [52]. The cooling strategy based on the thermal analysis of the tooling set-up (Figure 5-4.b) resulted in significant reduction of surface porosity (Figure 5-9). Some surface defects of minor scale were still observed at the end of the rib and away from the region of interest. These defects of minor influences could be eliminated by a rigorous control of the thermal distribution in the tool by reducing the radiation heat losses from the side frames of the tool. The micrographs were analyzed using ImageJ image processing

software to measure void content and resin rich areas. No noticeable resin rich areas were observed, and the void content was in the order of 0.2% in the junction region. ROS parts feature some warpage since the fibre layup is unsymmetrical and unbalanced. This warpage is greater for thin parts, and reduces with increasing thickness and with hybridization [13, 98]. On the T-stiffeners, no noticeable warpage of the flanges was observed although no objective measurements were made. However, the inclusion of a flow-control element and hybrid laminates appears to reduce the overall flange warpage.

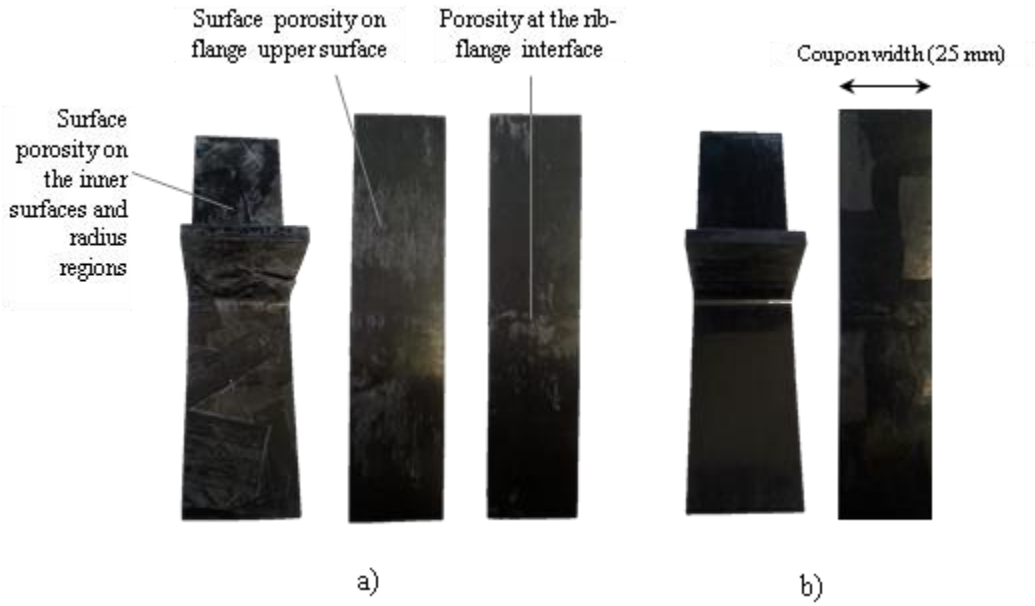

Figure 5-9: a) Surface porosity on the inner surfaces, radius regions and on the upper surfaces of the flange without preferential cooling strategy; b) Preferential cooling strategy minimizes the surface defects on radius region, the lower and upper surfaces of the flanges

Mechanical behaviour

The mechanical behaviour, specifically the load vs. displacement curves, failure characteristics and a comparison of the stiffness and pull-out loads of all the test configurations are discussed.

Load vs. displacement curves

Typical load vs. displacement curves of the test configurations are shown in Figure 5-10. The curve for pure ROS or configuration A is characterized by several delaminations in the T-junction accompanied by subsequent load drops. After the maximum load capacity has been attained, the load drops drastically. The load-displacement curve demonstrates more delaminations and load drops until the maximum restricted displacement of the fixture is reached. Configuration B has a higher stiffness and load capacity compared to configuration A. The most interesting result of this configuration is the reduced variability, which could be attributed to the improved flow of strands in the T-junction using the flow-control element. Box-plots in subsequent sections will quantify the variability of the results. Configuration C exhibits the highest stiffness and load capacity among all the configurations while large load drops of 40-50% are observed in all specimens after the maximum load is attained. This sudden drop results after the compression failure of the flange laminate as shown in Table 5-3. Configuration D has rib reinforcements in addition to a flow-control element. The stiffness behaviour is similar or slightly higher than that of configuration B until a certain point at which the RR plies delaminate from the central junction. This delamination is accompanied by a noticeable load drop. The load-displacement curve is less stiff owing to the reduced load carrying area in the junction. The final strengths of this configuration are lower than configuration B, indicating that an addition of rib reinforcements would decrease the load carrying capacity of the T-stiffeners. The stiffness of configuration E is like that of Configuration C, but the load capacity is lower. A drop of load is observed that could be the result of the delamination of the rib reinforcement plies. Similar large load drops in configuration C and E are observed, which are the result of compression failure of the flange reinforcement.

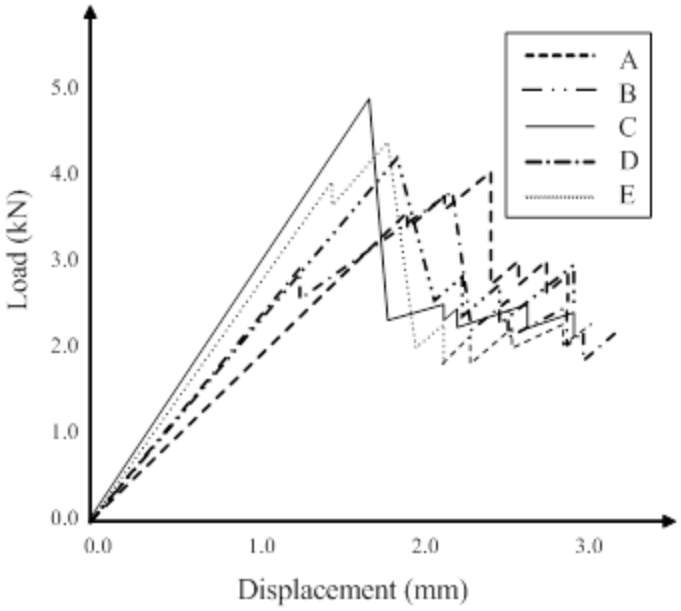

Figure 5-10: Typical load vs. displacement curves of the test configurations

Failure characteristics

The failure description and the sequence of failure appearances for all the test configurations are listed in Table 5-3. The macroscopic failure sequence is listed as observed during interrupted testing.

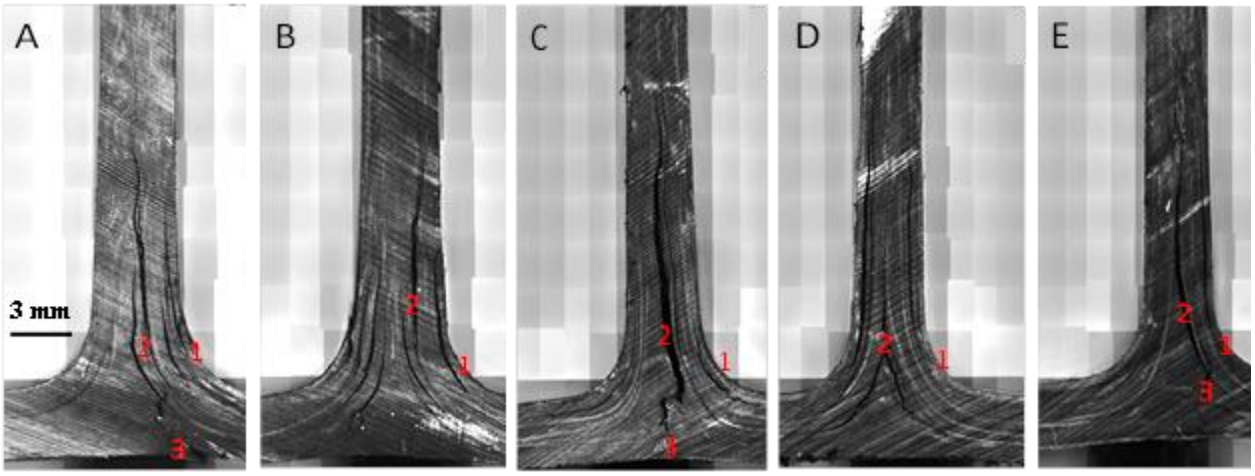

Figure 5-11: Typical failure images for the configurations (with failure sequence as appeared)

Configuration	Failure description (numbers refer to points indicated in Figure 5-11)
A	Progressive delamination occurred in the radii (1), in the direction of the strands. Then a large vertical crack opened in the rib (2), and propagated downwards. When it reached the surface of the flange (3), compression failure occurred.
B	Failure also begins with delamination near the radii (1). However, here, the cracks follow the direction of the strands (2) and tend not to cross the FCE. At one point, one of the cracks reaches the surface of a radius or the rib.
C	Progressive delamination occurred in the radii (1), in the direction of the strands. Then a large vertical crack opened in the rib (2) and propagated downwards leading to compression failure in the flange (3). No significant delaminations are present in the radius, but there is a big crack in the middle. There is consistency of failure modes across all the specimens tested.
D	Similar to B, except that rib reinforcement plies prevented the cracks from reaching the surface. The rib reinforcement plies de-bond completely from the radius region (1) and contain all the other cracks. The part completely opens up and extends to the rib with a greater magnitude (2). Failure of fibres on the RR tapes observed in some cases.
E	The rib reinforcement plies de-bond completely from the radius region (1) and contain all the other cracks. The part completely opens up and extends to the rib with a greater magnitude (2). On some parts, the FCE gets pulled off from the laminate group due to the delamination of the laminate group from the rest of the structure.

Table 5-3: Failure description of the configurations

Discussion

Figure 5-12 quantifies the pull-out load and stiffness behaviour of all the test configurations through box-plot representations. Pull-out load comparisons of configurations A and B indicate the effect of the flow-control element. A significant improvement of 24% on the B-basis load allowable is observed in configuration B that incorporates an FCE. Configuration B coupons have the lowest scatter in loads and stiffness values, and a higher median of the results compared to A indicating that the orientation of strands has a small impact on the pull-out stiffness of the part. While the flow-control method revealed excellent consistencies and repeatability on configurations B, C, D and E, it should be noted that limited studies on the size and shape of FCE has been performed in this work.

A comparison of configurations B and C allows us to assess the effect of adding flange reinforcement. Adding 8-layers of a quasi-isotropic laminate on the flange (about 37% of flange thickness) significantly increases the load capacity by 8% compared to configuration B, and 12.5% compared to configuration A, when considering the median of the results. Configuration C exhibits a stiffness increase of 18% compared to B and 25% compared to A. The laminate group is loaded in compression before failure, and exhibits higher compression strength, which explains the higher global strength of T-stiffeners in configuration C. The B-basis allowables of configuration B are higher than configuration C due to the variability of results caused due to a change in the failure mode. This change in the failure characteristics is caused due to the addition of the laminate group and a smaller flow-control element. Configurations B and D, which did not feature any flange reinforcements are mainly subjected to delamination near the radii that propagated along the interface of the flow-control element. Further, the flow-control element should be accompanied with the flange reinforcement to avoid any ply waviness in the flange.

Comparing configurations B and D allows us to assess the effect of adding two 0° plies as rib reinforcement. Normally, a higher pull-out strength and stiffness is expected with the addition of rib reinforcements as they increase the bending stiffness and strength of the rib. However, the effect of RR was a reduction of stiffness and pull-out strength as observed in

Figure 5-12. This can be explained by the failure sequence in specimens of configuration D. As the loading increases, the first delamination occurs at the interface of the rib reinforcement plies and ROS. This delamination extends throughout the interface reducing the load carrying contribution of the rib reinforcement plies to the load capacity of the overall junction. In addition, a total delamination of the rib reinforcement plies reduces the effective thickness of the junction that resists the bending moment, making the junction thinner than configuration B. A thinner junction now exhibits lower bending stiffness, hence a change in the slope as seen in the load-displacement curve of configuration D. Similarly, in configuration E, while the rib reinforcements tend to reduce the stiffness and pull-out strength of the part, the presence of the laminate group takes over the global behaviour boosting the stiffness of the part. The hybridization strategies must be adapted to the design requirements and to the loading conditions. For instance, rib reinforcement tapes improve the part performance if the rib is asymmetrically pulled or if tensile strength of the rib is critical to the design.

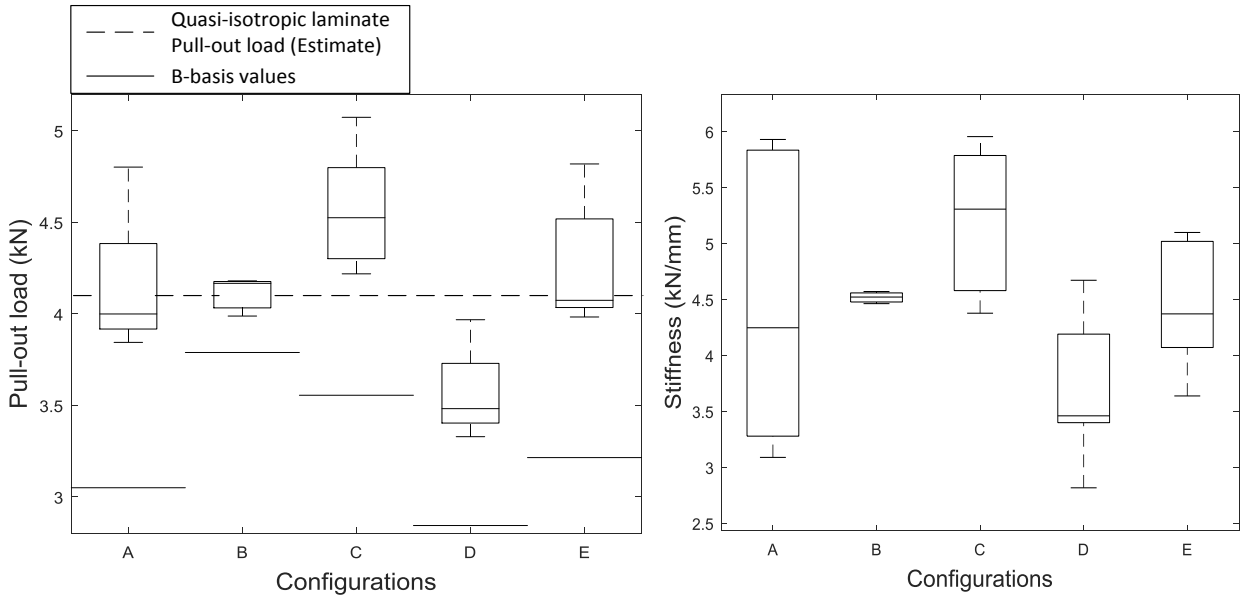

Figure 5-12: Pull-out load and Part stiffness comparisons of the test configurations

The comparisons of the pull-out loads and stiffness of the test configurations also represent the load-to-weight ratio and stiffness-to-weight ratios respectively, as the weights for all the configurations are identical.

Figure 5-12 also compares the pull-out load results of the test configurations with the conservative estimate of pull-out strength of a geometrically equivalent quasi-isotropic T-stiffener assumed to be comprised of two symmetric L-angles fabricated with quasi-isotropic layup and a noodle. Using the equations from ASTM D6415 [145] and the experimental results obtained by Fortin [39], the ILTS was obtained for a quasi-isotropic L-angle. Using the relations from [146] and an interaction of interlaminar tensile and shear stresses, the pull-out load that

produces a zero margin of safety is calculated. The effect of the noodle is ignored, the thickness of the L-angle is considered constant, interlaminar tensile stress is assumed to be the highest at the mid portion of the radius and the minor effect of interlaminar shear stress is considered. In practice, the actual coupons of quasi-isotropic T-stiffeners would fail at higher pull-out loads than the conservative estimates calculated in this work. The comparisons of pull-out strengths of T-stiffeners of ROS with the pull-out load estimate of quasi-isotropic T-stiffeners are to be regarded as rather qualitative as the conservative calculations are based on experiments on L-stiffeners placed back-to-back and not on actual T-stiffeners.

5.1.6 Conclusions

Two major flow induced defects that cause variability issues in random strand-based materials are recognized as strand waviness and swirling of strands at junctions of geometric features. Three hybridization strategies are proposed, implemented and validated experimentally on T-stiffeners. The mechanical behaviour (specifically the pull-out load capacities) of four test configurations of T-stiffeners incorporating hybridization strategies has been studied. Pull-out strength tests with roller support conditions were performed and the respective load-displacement behaviour, failure modes and variability have been quantified and compared with a pure ROS based part. Transient heat analysis using finite elements is performed to obtain preferential temperature gradients within the tooling set-up. The cooling strategy devised for the tooling set-up minimizes surface and part porosity.

The first hybridization strategy is a flow-control method that uses a flow-control element to mitigate strand out-of-plane waviness and swirling in complex junctions of geometric features by conforming to the shape of the cavity and assisting the flow of strands. The method demonstrates

high processing consistency, repeatability, and ease-of-manufacture. The presence of a flow-control element alone reduces the test variability and increases the pull-out strength of an ROS part by 24% when B-basis allowable values are considered. The second strategy is that of a flange reinforcement that is to be incorporated in conjunction with the flow-control element. A flow-control element prevents laminate waviness when used with flange reinforcements. Flange reinforcement (quasi-isotropic laminate) with a flow-control element produces the highest stiffness and strength (25% improvement compared to pure ROS) when median of the results is considered. The third strategy is the use of rib reinforcement. The strategy changes the failure mode and causes the delamination of the reinforcement from the ROS part causing a detrimental effect on the pull-out strength (6% lower B-basis values than pure ROS). However, rib reinforcements can be utilized in designs requiring rib strengthening or secondary loads. Lowest variation in stiffness and strength results is produced by the configuration with ROS incorporating flow-control element only while the highest pull-out loads are obtained for configuration incorporating flow-control element and flange reinforcements. The use of the proposed hybridization strategies enhances the pull-out strength capacities of ROS based stiffening features to a comparable value with the design estimates of pull-out strengths of T-stiffeners fabricated with quasi-isotropic laminates.

Chapter 6

Conclusions

6.1 Scientific contributions and Conclusions

The research work presented in this thesis is a systematic and first of its kind study on hybrid fibre architectures of randomly oriented strands and laminate groups, aimed at obtaining trade-off solutions of formability characteristics and structural performance. Through the performance and process improvements proposed in this research, hybrid fibre architectures of ROS and laminates have demonstrated strong prospects in extending the use of complex composite parts to moderately loaded structural applications from the current non-structural applications.

The following sections will highlight the specific scientific contributions and conclusions of this work under four categories: Literature review, Mechanical characterization, Modelling work, and Manufacturing feasibility.

a). Literature review: Pertinent research on the mechanical characterization of randomly oriented strand composites and systems analogous to ROS-hybrids were categorized into a framework of a formal characterization environment of composite structures that includes the coupon, part and structural levels. The review on the modelling aspects involved the identification of crucial characteristics and principles of significant analytical and numerical modelling techniques devised for the prediction of the mechanical behaviour of ROS and their hybrids. The literature categorized as a part of this work was realized into a 'general review' article that forms the first formal review on the topic.

b). Mechanical characterization: Mechanical characterisation of hybrid fibre architectures of randomly oriented strands of carbon/PEEK and continuous fibre tapes of carbon/PEEK were performed at the coupon levels under tensile and interlaminar shear loading scenarios.

Tensile behaviour. The tensile behaviour of hybrid fibre architectures of ROS and three laminate groups (Cross-ply, Angle-ply and Quasi-isotropic) were studied and compared with aluminum. Improvements of up to ~40% in stiffness, and strength improvements as high as twice are observed for Cross-ply/ROS-hybrid with Tapes-ROS-Tapes hybrid stacking and 15% thickness of laminate reinforcement in the hybrid. Tapes-ROS-Tapes hybrid configuration produces the best results in terms of stiffness, strength and variability. A positive synergy or deviation from rule of mixtures of 19-24% in stiffness and 20-27% in strength was observed across all hybrids with Tapes-ROS-Tapes hybrid stacking, with the maximum positive synergy observed when the extensional stiffness of ROS and laminate groups were equal.

Interlaminar shear behaviour. Tapes-ROS-Tapes configurations demonstrated better apparent interlaminar shear strengths than the parent materials, across all the laminate groups and thickness ratios. Synergies in Tapes-ROS-Tapes configurations of up to 25% were observed and were explained using the load sharing among the phases. It was observed that the ROS-Tapes-ROS configurations demonstrated negative synergies with losses up to 20-25% in interlaminar shear strength.

c). Modelling work: Predictive stochastics-based FE and analytical modelling techniques were proposed for ROS and hybrids while accounting for the main failure mechanisms, progressive failure, and load sharing under tensile and interlaminar shear loading scenarios.

Tensile behaviour. The 3D FE models utilized three important stages: the use of a strand placement and generation procedure and empirical parameters to replicate the processing, intralaminar progressive failure analysis using Hashin failure criteria for damage initiation and fracture energy based linear softening law for damage propagation, and the use of traction-separation cohesive element laws to model the interlaminar progressive analysis or interface behaviour. Overall, the models represent improvements compared to similar models in literature and match the trends observed during experiments and predicts the tensile stiffness and strength of the specimens.

Interlaminar shear behaviour. A semi-empirical model based on a stochastic strand placement procedure in conjunction with analytical expressions was developed for understanding and explaining the load sharing in the phases when subjected to out-of-plane shear loading. Further, the model successfully captured the relative behaviour of

the configurations and the extent of synergy in various hybrids, with reasonable accuracies. The model used the ratio of the bending to the shear stress levels in configurations relative to that of the stress levels ratios in ROS to predict the relative behaviour and synergies. The model exhibited a potential to reduce testing efforts by providing relative behaviour of ROS-hybrids with reference to a few standard tests of benchmark laminates.

d). Manufacturing feasibility: At the part level, the feasibility of manufacturing hybrid fibre architectures was assessed by fabricating T-stiffeners.

Three hybridization strategies were proposed to mitigate flow-induced defects such as strand waviness and swirling of strands at junctions of geometric features and were demonstrated on T-stiffeners. The first hybridization strategy involved the use of a flow-control element at the complex junctions and allowing it to conform to the shape of the cavity and assist the flow of strands. The presence of a flow-control element alone reduces the test variability and increases the pull-out strength of an ROS part by 24% in B-basis values. The second strategy involved the use of a flange reinforcement in conjunction with the flow-control element. Flange reinforcement (quasi-isotropic laminate) with a flow-control element produced the highest stiffness and strength (25% improvement compared to pure ROS). The third strategy involved the use of rib reinforcements. The strategy changes the failure mode and causes the delamination of the reinforcement from the ROS part causing a detrimental effect on the pull-out strength (6% lower B-basis values than pure ROS).

6.2 Future work

While integrated structures of ROS-hybrids offer attractive benefits in comparison to their metallic counterparts, several challenges concerning the mechanical characterization and modelling must be addressed for the implementation of ROS/ROS-hybrid architectures on a production scale and are discussed briefly henceforth.

6.2.1 Challenges - Mechanical characterization

Strand length effects. The strong dependence of material strength on strand size raises questions regarding the accuracy of strength measurements obtained by testing cut-to-shape specimens, since the actual ROS parts are mostly net-shape moulded including the holes. Any cutting or drilling operations would reduce the effective strand size at the edges and may lead to premature crack initiation. Work on net-shapes parts include that of Eguémann [38] and Landry [137]. Landry investigated the strand orientations in an actual stiffened bracket and showed that higher stiffness is observed in net-parts with proximity to the moulding walls. Nevertheless, it is reasonable to believe that the cut coupons represent conservative estimates of a net shaped part, but this topic warrants further study.

Test framework, Design allowables, Inspection methods. The suitability of the typical building block approach used for composites is to be studied in relevance to ROS/ROS-hybrids, as the part qualification seems part-centric rather than material centric owing to the multiplicity of failure mechanisms and design freedom. Further, the suitability of the test methods used for laminated composites must be studied in relevance to ROS material in greater detail. The variability of the experimental data calls for the use of basis values to quantify the design allowables. The use of basis design allowables is severe with smaller number of the test

population and requires extensive material qualification involving numerous tests for statistical confidence. All the research works in the literature have been tested with limited numbers of test coupons. Thus, more statistical confidence on the experimental data is needed.

Further, work is needed on reliable and low-cost quality non-destructive inspection methods for ROS/ROS-hybrid parts in a production environment. Employing vibrations based measurements for stiffness characteristics of ROS parts seem promising [55, 147], while the strength measurements as a function of defects is still a challenge. MicroCT/CT-scan techniques do show potential to quantify the orientations of small samples.

Notch sensitivity. ROS materials are notch-insensitive [148], a behaviour attributed to the inherent stress risers in the material architecture. In their preliminary work, Visweswaraiah et al [30] studied the notched behaviour of ROS-hybrids and demonstrated the notched behaviour, while improving the overall notched properties of the hybrids. Such a study facilitates the designers to anticipate failure locations, and their magnitudes in actual parts. Systematic conditions for notched sensitivity in hybrids are to be developed.

Cost analysis. While the use of ROS and ROS-hybrids seems to be a cost-effective alternative to the traditional autoclave processes, the non-recurring tooling costs associated with the manufacturing method such as compression moulding could be high. Nevertheless, the possibility of including integrated nested features such as holes minimize post-moulding operations such as drilling/trimming thus saving costs. ROS architecture also allows for the effective utilization of chips from cut scraps of continuous plies and promotes the re-use of composites. Thus, the cost-effectiveness of using ROS/ROS-hybrids vs. their benefits, needs to be verified case-by-case using a cost analysis method [149].

6.2.2 Challenges - Numerical modelling

Homogenization and RVE. Although RVE and homogenization schemes seem suitable and attractive to predict the mechanical behaviour of ROS-hybrids, challenges on the selection of a suitable RVE size, the definition of the boundary conditions, the extent of the effect of geometry and process parameters on the failure and results variability should be better understood. For example, physically modelling strand waviness might involve high computational expenses and yield inconclusive results. Processing parameters are one of the key aspects that drive the overall characteristics of ROS and their hybrids, and models should be inclusive. The applicability of the numerical models developed for ROS-hybrids are to be applied at the part-level.

More confidence is to be established by modelling the strand orientations measured through CT scans of actual specimens and be replicated in the simulation. The testing can be done by running interrupted tests to detect and to monitor damage evolution with increasing load levels and be compared with the simulation. Studies on the applicability and validity of several FE models proposed for ROS in relevance to hybrid fibre architectures are yet to be explored.

Residual stresses, Strand waviness. While residual stresses play a crucial role in determining the geometric tolerances, the strand out-of-plane waviness affects the properties. Both these aspects require more attention. A practical approach is to stochastically apply the effect of the factors such as strand waviness on the stiffness properties via empirical knockdown factors on the design allowables. While this approach could lead to conservative results, it does account for the material uncertainties. Such empirical knock down factors are to be determined as a part of future research. While the modelling methods proposed in this research certainly guide the design process, the factors listed above are to be considered for more accurate results.

References

1. Wakeman, M.D. and C.D. Rudd, *Compression molding of thermoplastic composites*, in *Comprehensive Composite Materials*, K. Anthony and Z. Carl, Editors. 2000, Pergamon: Oxford. p. 915-963.

2. Verpoest, I., *Composite Preforming Techniques*, in *Comprehensive Composite Materials*, K. Anthony and Z. Carl, Editors. 2000, Pergamon: Oxford. p. 623-669.

3. Lessard, H., et al., *Influence of process parameters on the thermostamping of a [0/90]12 carbon/polyether ether ketone laminate.* Composites Part A: Applied Science and Manufacturing, 2015. **70**: p. 59-68.

4. P. D. Soden, M.J.H., A. S. Kaddour, *A Comparision of the Predictive Capabilities of Current Failure Theories for Composite Laminates.* Composites Science and Technology, 1998. **58**.

5. Kelly, A. and W.R. Tyson, *Tensile properties of fibre-reinforced metals: Copper/tungsten and copper/molybdenum.* Journal of the Mechanics and Physics of Solids, 1965. **13**(6): p. 329-350.

6. Chang, I.Y. and J.F. Pratte, *LDF thermoplastic composite technology.* Journal of Thermoplastic Composite Materials, 1991. **4**: p. 227-252.

7. Schuster, J. and K. Friedrich, *Fatigue testing of thermoformed bidirectional LDF™-composites.* Applied Composite Materials, 1994. **1**(1): p. 55-68.

8. A. Ionita, Y.J.W., *On the mechanical response of randomly reinforced chopped-fibers composites: Data and model.* Composites Science and Technology, 2006. **66**(14).

9. Fu, S.-y., B. Lauke, and Y.-W. Mai, *Science and Engineering of Short Fibre Reinforced Polymer Composites*. 1st Edition ed. 2009: Woodhead Publishing.

10. Such, M., C. Ward, and K. Potter, *Aligned Discontinuous Fibre Composites: A Short History.* Journal of Multifunctional Composites, 2014. **3**: p. 155–168.

11. Feraboli, P., et al., *Characterization of prepreg-based discontinuous carbon fiber/epoxy systems.* Journal of Reinforced Plastics and Composites, 2009. **28**(10): p. 1191-1214.

12. Selezneva, M. and L. Lessard, *Characterization of mechanical properties of randomly oriented strand thermoplastic composites.* Journal of Composite Materials, 2015.

13. S.B.Visweswaraiah, L.L., P.Hubert, *Tensile Behaviour of Hybrid Fibre Architectures of Randomly Oriented Strands combined with Laminate groups.* Journal of Composite Materials, 2016. **(Under review)**.

14. Wakeman, M.D., et al., *Compression moulding of glass and polypropylene composites for optimised macro- and micro-mechanical properties. 4: Technology demonstrator - a door cassette structure.* Composites Science and Technology, 2000. **60**: p. 1901-1918.

15. Wakeman, M., et al., *Stamp forming of carbon fibre/PA12 composites – A comparison of a reactive impregnation process and a commingled yarn system.* Composites Science and Technology, 2006. **66**(1): p. 19-35.

16. Bourban, P.E., et al., *Integrated processing of thermoplastic composites.* Composite Science and Technology, 1998. **58**(5): p. 633-637.

17. Bourban, P.-E., et al., *Material phenomena controlling rapid processing of thermoplastic composites.* Composites Part A, 2001. **32**(8): p. 1045-1057.

18. Bernet, N., et al., *Commingled yarn composites for rapid processing of complex shapes.* Composites Part A: Applied Science and Manufacturing, 2001. **32**(11): p. 1613-1626.

19. Bernet, N., et al., *An integrated cost and consolidation model for commingled yarn based composites.* Composites Part A: Applied Science and Manufacturing, 2002. **33**(4): p. 495-506.

20. Jansson, N., et al., *Finite element modelling and testing of an injection moulded generic tow reinforced structure.* Composites Part B: Engineering, 2005. **36**(6–7): p. 487-495.

21. Jansson, N., M.D. Wakeman, and J.A.E. Månson, *Optimization of hybrid thermoplastic composite structures using surrogate models and genetic algorithms.* Composite Structures, 2007. **80**(1): p. 21-31.

22. Swolfs, Y., L. Gorbatikh, and I. Verpoest, *Fibre hybridisation in polymer composites: A review.* Composites Part A: Applied Science and Manufacturing, 2014. **67**: p. 181-200.

23. Marom, G., et al., *Hybrid effects in composites: conditions for positive or negative effects versus rule-of-mixtures behaviour.* J Mater Sci, 1978. **13**(7): p. 1419-1426.

24. Kilic, M.H. *Multi-scale modeling of discontinuous long-fibre composites* in *SAMPE Conference Proceedings*. 2014. Seattle, WA.

25. Greene, Tweed *XYCOMP® DLF high-performance thermoplastic composite* 2014.

26. Thomas, G.P., *Compression Molded Composites: Processes, Benefits and Applications – An Interview With TenCate*, in *AZoM*.

27. Roy, S., et al., *Compression Molding of Composite Tailboom Frames*, in *AHS 70th Annual Forum*. 2014, American Helicopter Society International, Inc: Montreal.

28. Visweswaraiah, S.B., L. Lessard, and P. Hubert, *Interlaminar Shear Behaviour of Hybrid Fibre Architectures of Randomly Oriented Strands Combined with Laminate Groups.* Composite Structures, 2017.

29. Visweswaraiah, S.B., et al., *Flow-control and hybridization strategies for thermoplastic stiffened panels of long discontinuous fibers.* Journal of Reinforced Plastics and Composites, 2017. **0**(0): p. 0731684417707585.

30. Visweswaraiah, S., et al. *Conditions for Notch Sensitivity in Hybrid Fibre Architectures of Randomly Oriented Strands combined with Laminate groups*. in *COMPTEST 2017*. 2017. S.L. Lomov, L. Gorbatikh, Y. Swolfs.

31. Visweswaraiah, S., et al. *Effects of Hybridization of Laminates with Randomly Oriented Strands at Coupon and Part levels*. in *CANCOM 2017*. 2017. Ottawa.

32. Corbridge, D.M., et al., *Compression moulding of composites with hybrid fibre architectures.* Composites Part A: Applied Science and Manufacturing, 2017. **95**(Supplement C): p. 87-99.

33. Han, J.H., et al. *Effect of fabric reinforcement on failure response of discontinuous long fiber composite bolted joints*. in *SAMPE* 2011. Long Beach, CA.

34. Evans, A.D., et al., *Joint Design of Continuous/Discontinuous Hybrid Carbon Fibre Composites*, in *21st International Conference on Composite Materials*. 2017.

35. USA, D.o.D.-. *Composite Materials Handbook : Polymer Matric Composites Guidelines for Characterization of Structural Materials*. 2002.

36. Feraboli, P., et al., *Characterization of Prepreg-Based Discontinuous Carbon Fiber/Epoxy Systems.* Journal of Reinforced Plastics and Composites, 2008. **28**(10): p. 1191-1214.

37. Yamashita, S., et al., *Experimental characterization of the tensile failure mode of ultra-thin chopped carbon fiber tape-reinforced thermoplastics.* Journal of Reinforced Plastics and Composites, 2016. **35**(18): p. 1342-1352.

38. Eguémann, N., *Study on the mechanical behaviour of carbon fibre reinforced PEEK polymer with a layered discontinuous architecture*. 2013, L'U.F.R. des sciences et techniques de l'Université de Franche-Comté.

39. Fortin, G.Y., *Process-induced shape distortions in aerospace thermoplastic composites*, in *Materials Engineering*. 2016, University of British Columbia.

40. Harper, L.T., et al. *Automated spray deposition for net-shape carbon/epoxy compression moulding* in *ICCM-17*. 2009. Edinburgh, UK.

41. Qian, C., et al., *Notched behaviour of discontinuous carbon fibre composites: Comparison with quasi-isotropic non-crimp fabric.* Composites Part A: Applied Science and Manufacturing, 2011. **42**(3): p. 293-302.

42. Johanson, K., et al., *Studying the heterogeneity of discontinuous fiber composites using a new full-field strain measurement system*, in *The 19th international conference on composite materials*. 2013: Montreal, Canada.

43. *HexMC® User Guide*. 2013, Hexcel Corporation.

44. Wan, Y. and J. Takahashi, *Tensile properties and aspect ratio simulation of transversely isotropic discontinuous carbon fiber reinforced thermoplastics.* Composites Science and Technology, 2016. **137**(Supplement C): p. 167-176.

45. Jin, B.C., et al., *Optimization of microstructures and mechanical properties of composite oriented strand board from reused prepreg.* Composite Structures, 2017. **174**: p. 389-398.

46. Lessard, H., et al., *Influence of process parameters on the thermostamping of a [0/90]12 carbon/polyether ether ketone laminate.* Composites: Part A, 2015. **70**(1): p. 59-68.

47. Feraboli, P., et al., *Modulus measurement for prepreg-based discontinuous carbon fiber/epoxy systems.* Journal of Composite Materials, 2009. **43**(19): p. 1947-1965.

48. Johanson, K., et al., *Heterogeneity of discontinuous carbon fibre composites: Damage initiation captured by Digital Image Correlation.* Composites Part A: Applied Science and Manufacturing, 2015. **68**(Supplement C): p. 304-312.

49. Kilic, M.H. *A nonlinear 3D micromechanical and structural framework for analysis of discontinuous long-fiber thermoplastic composites*. in *CAMX – The Composites and Advanced Materials Expo*. 2014. Orlando, FL.

50. Landry, B. and P. Hubert, *Experimental study of defect formation during processing of randomly-oriented strand carbon/PEEK composites.* Composites Part A: Applied Science and Manufacturing, 2015. **77**(Supplement C): p. 301-309.

51. LeBlanc, D., *Compression moulding of complex parts with randomly-oriented strand thermoplastic composites*, in *Department of Mechanical Engineering*. 2014, McGill University: Montreal.

52. LeBlanc, D., et al., *Study of Processing Conditions on the Forming of Ribbed Features Using Randomly Oriented Strands Thermoplastic Composites.* Journal of the American Helicopter Society, 2015. **60**(1): p. 1-9.

53. Yamashita, S., et al., *Volume resistivity of ultra-thin chopped carbon fiber tape reinforced thermoplastics.* Composites Part A: Applied Science and Manufacturing, 2016. **90**(Supplement C): p. 598-605.

54. Wan, Y. and J. Takahashi, *Tensile and compressive properties of chopped carbon fiber tapes reinforced thermoplastics with different fiber lengths and molding pressures.* Composites Part A: Applied Science and Manufacturing, 2016. **87**(Supplement C): p. 271-281.

55. Lyu, X., et al., *Determination of transverse flexural and shear moduli of chopped carbon fiber tape-reinforced thermoplastic by vibration.* Journal of Composite Materials. **0**(0): p. 0021998317707815.

56. Guo, Q., et al., *Numerical and Experimental study of the Mode I Interlaminar Failure of Chopped Carbon Fiber Tape Reinforced Thermoplastics*, in *21st International Conference on Composite Materials*. 2016, ICCM: Xi'an.

57. Meng, L., et al., *Failure Analysis of Ultra-Thin Chopped Carbon Fiber Tape Reinforced Thermoplastic in Mechanical Joints*, in *ECCM17 - 17th European Conference on Composite Materials*. 2016, ECCM: Munich.

58. Yamashita, S., et al., *Residual mechanical properties of carbon fibre reinforced thermoplastics with thin-ply prepreg after simulated lightning strike.* Composites Part A: Applied Science and Manufacturing, 2017. **101**(Supplement C): p. 185-194.

59. Fujita, M., Y. Nakashima, and J. Takahashi, *Influence of Strand Dispersion Method on Mechanical properties of Hollow-S-shaped member made of Randomly-Oriented CFRTP Strands*, in *21st International Conference on Composite Materials*. 2017: Xi'an.

60. Toyoda, H., et al., *Influence of Strand Dimension and Dispersion Method on Rigidity and its Scatter of Hat Shaped specimens made of Randomly-Oriented CFRTP Strands*, in *21st International Conference on Composite Materials*. 2017: Xi'an.

61. Han, J.H., W.B. Alexander, and A. Godwin. *Characterization of milled carbon fiber added random discontinuous long fiber composites*. in *SAMPE*. 2010. Baltimore. WA.

62. Boursier, B. and A. Lopez, *Failure initiation and effect of defects in structural discontinuous fibre composites*, in *Fall Technical Conference*. 2010, SAMPE.

63. Jacob, G.C., et al., *Crashworthiness of various random chopped carbon fiber reinforced epoxy composite materials and their strain rate dependence.* Journal of Applied Polymer Science, 2006. **101**(3): p. 1477-1486.

64. Rasheed, M.I.A., *Compression molding of chopped woven thermoplastic composite flakes - A study on processing and performance, PhD Thesis*. 2016, University of Twente: Netherlands.

65. TenCate Advanced Composites, *Datasheet: TenCate Cetex(R) MC1200 PEEK Thermoplastic BMC*. 2012.

66. Kravchenko, S.G., *Failure Analysis in Platelet Molded Composite Systems*, in *Department of Aeronautics and Astronautics*. 2017, Purdue University: West Lafayette, Indiana. p. 341.

67. Luo, Y. and I. Verpoest, *Compressibility and relaxation of a new sandwich textile preform for liquid composite molding*. Polymer Composites, 1999. **20**(2): p. 179-191.

68. Wakeman, M.D., et al., *Compression moulding of glass and polypropylene composites for optimised macro- and micro- mechanical properties 3. Sandwich structures of GMTs and commingled fabrics.* Composites Science and Technology, 1999. **59**(8): p. 1153-1167.

69. Wakeman, M.D., et al., *Robotic tow placement for local reinforcement of glass mat thermoplastics (GMTs).* Composites Part A: Applied Science and Manufacturing, 2002. **33**(9): p. 1199-1208.

70. Lee, S.-H., et al., *A toughening and strengthening technique of hybrid composites with non-woven tissue.* Journal of Materials Processing Technology, 2008. **207**(1–3): p. 21-29.

71. Selmy, A.I., et al., *Monotonic properties of unidirectional glass fiber (U)/random glass fiber (R)/epoxy hybrid composites.* Materials & Design, 2011. **32**(2): p. 743-749.

72. Selmy, A.I., et al., *Interlaminar shear behavior of unidirectional glass fiber (U)/random glass fiber (R)/epoxy hybrid and non-hybrid composite laminates.* Composites Part B: Engineering, 2012. **43**(4): p. 1714-1719.

73. Selmy, A.I., et al., *In-plane shear properties of unidirectional glass fiber (U)/random glass fiber (R)/epoxy hybrid and non-hybrid composites.* Composites Part B: Engineering, 2012. **43**(2): p. 431-438.

74. Cabrera-Ríos, M. and J.M. Castro, *An economical way of using carbon fibers in sheet molding compound compression molding for automotive applications.* Polymer Composites, 2006. **27**(6): p. 718-722.

75. Wulfsberg, J., et al., *Combination of Carbon Fibre Sheet Moulding Compound and Prepreg Compression Moulding in Aerospace Industry.* Procedia Engineering, 2014. **81**(Supplement C): p. 1601-1607.

76. Mallick, P.K., *Effect of fiber misorientation on the tensile strength of compression molded continuous fiber composites.* Polymer Composites, 1986. **7**(1): p. 14-18.

77. Duane Emerson & Daniel Grauer, B.H., Manfred Reif & Frank Henning, Andreas Martsman, Simon Tage Jespersen, *Using Unidirectional Glass Tapes to improve Impact performance of Thermoplastic Composites in Automotive Applications.* 2012.

78. Thattaiparthasarthy, K.B., et al. *Continuous fibers tailored long fiber reinforced thermoplastics* in *ICCM-17*. 2009. Edinburgh, UK.

79. Ghasemnejad, H., H. Hadavinia, and A. Aboutorabi, *Effect of delamination failure in crashworthiness analysis of hybrid composite box structures.* Materials & Design, 2010. **31**(3): p. 1105-1116.

80. Leblanc, D., et al. *Compression moulding of stiffened brackets using randomly-oriented strands thermoplastic composites*. in *CAMX 2014 - Composites and Advanced Materials Expo: Combined Strength. Unsurpassed Innovation*. 2014.

81. Fette, M., et al., *Automated and Cost-efficient Production of Hybrid Sheet Moulding Compound Aircraft Components.* Procedia Manufacturing, 2016. **6**: p. 132-139.

82. Fette, M., et al., *New Methods for Computing and Developing Hybrid Sheet Molding Compound Structures for Aviation Industry.* Procedia CIRP, 2017. **66**: p. 45-50.

83. Tuttle, M., T. Shifman, and B. Boursier. *Simplifying certification of discontinuous composite material forms for primary aircraft structures* in *SAMPE*. 2010. Seattle, US.

84. Harban, K. and M. Tuttle, *Certification of Discontinuous Fiber Composites via Stochastic Modeling*. 2017, FAA: New Jersey, USA.

85. Jin, B.C., et al., *Nondestructive Testing and Evaluation of Conventional and Reused Carbon Fiber Epoxy Composites using Ultrasonic and Stitched MicroCT*, in *SAMPE*. 2016: Long Beach.

86. Caba, A.C., *Characterization of carbon mat thermoplastic composites: flow and mechanical properties.*, in *Engineering Mechanics*. 2005, Virginia Polytechnic Institute and State University: Blacksburg.

87. Yi Pan, L.I., Assimina A. Pelegri, *Numerical generation of a random chopped fiber composite RVE and its elastic properties.* Composites Science and Technology, 2008. **68**: p. 2792–2798.

88. Tucker Iii, C.L. and E. Liang, *Stiffness predictions for unidirectional short-fiber composites: Review and evaluation.* Composites Science and Technology, 1999. **59**(5): p. 655-671.

89. Kirupanantham, G., *Characterisation of discontinuous carbon fibre preforms for automotive applications*. 2013, University of Nottingham.

90. Krenchel, H., *Fibre reinforcement*. 1964, Copenhagen: Akademisk Forlag.

91. Mori, T. and K. Tanaka, *Average stress in matrix and average elastic energy of materials with misfitting inclusions.* Acta Metallurgica, 1973. **21**(5): p. 571-574.

92. Jain, A., B.C. Jin, and S. Nutt, *Mean field homogenization methods for strand composites.* Composites Part B: Engineering, 2017. **124**: p. 31-39.

93. Jain, A., et al., *Non-symmetric stiffness tensor prediction by the Mori–Tanaka scheme – Comments on the article "Effective anisotropic stiffness of inclusions with debonded interface for Eshelby-based models" [Composite Structures 131 (2015) 692–706].* Composite Structures, 2015. **134**(Supplement C): p. 1118-1119.

94. Lielens, G., et al., *Prediction of thermo-mechanical properties for compression moulded composites.* Composites Part A: Applied Science and Manufacturing, 1998. **29**(1-2): p. 63-70.

95. Benveniste, Y., *A new approach to the application of Mori-Tanaka's theory in composite materials.* Mechanics of Materials, 1987. **6**(2): p. 147-157.

96. Sato, Y., et al., *Elastic modulus estimation of chopped carbon fiber taper reinforced thermoplastics using the monte carlo simulation*, in *The 19th international conference on composite materials*. 2013: Montreal, Canada.

97. Nakashima, Y., et al., *Analytical modelling of the behaviour and scatter of the flexural modulus of randomly oriented carbon fibre strand thermoplastic composites.* Composite Structures, 2017. **178**(Supplement C): p. 217-224.

98. Selezneva, M., et al., *Analytical model for prediction of strength and fracture paths characteristic to randomly oriented strand (ROS) composites.* Composites Part B: Engineering, 2016. **96**: p. 103-111.

99. Bekah, S., R. Rabiei, and F. Barthelat, *The Micromechanics of Biological and Biomimetic Staggered Composites.* Journal of Bionic Engineering, 2012. **9**(4): p. 446-456.

100. Pimenta, S. and P. Robinson, *An analytical shear-lag model for composites with 'brick-and-mortar' architecture considering non-linear matrix response and failure.* Composites Science and Technology, 2014. **104**: p. 111-124.

101. Harper, L.T., et al., *Representative volume elements for discontinuous carbon fibre composites – Part 1: Boundary conditions.* Composites Science and Technology, 2012. **72**(2): p. 225-234.

102. Harper, L.T., et al., *Representative volume elements for discontinuous carbon fibre composites – Part 2: Determining the critical size.* Composites Science and Technology, 2012. **72**(2): p. 204-210.

103. Qian, C., et al. *Determination of the size of representative volume elements for discontinuous fibre composites*. in *18th International Conference on Composite Materials*. 2011. Jeju, Korea.

104. Harper, L.T., et al., *Fiber Alignment in Directed Carbon Fiber Preforms - Mechanical Property Prediction.* Journal of Composite Materials, 2009. **44**(8): p. 931-951.

105. Feraboli, P., et al., *Stochastic laminate analogy for simulating the variability in modulus of discontinuous composite materials.* Composites Part A: Applied Science and Manufacturing, 2010. **41**(4): p. 557-570.

106. Head, B.H., *Analysis methods for discontinuous fiber composites*. 2013, University of Washington: Washington.

107. Selezneva, M., et al., *Modelling of mechanical properties of randomly oriented strand thermoplastic composites.* Journal of Composite Materials, 2017. **51**(6): p. 831-845.

108. Li, Y., et al., *Experimental investigation of randomly-oriented tow-based discontinuous composites and their equivalent laminates.* Composites Part A: Applied Science and Manufacturing, 2017. **102**(Supplement C): p. 64-75.

109. Dai, C. and P.R. Steiner, *Spatial structure of wood composites in relation to processing and performance characteristics. Part 2. Modelling and simulation of randomly-formed flake layer network.* Wood Science and Technology, 1994. **28**: p. 135-146.

110. Painter, G., H. Budman, and M. Pritzker, *Prediction of oriented strand board properties from mat formation and compression operating conditions. Part 1. Horizontal density distribution and vertical density profile.* Wood Science and Technology, 2005. **40**(2): p. 139-158.

111. Lu, C., P.R. Steiner, and F. Lam, *Simulation study of wood-flake composite mat structures.* Forest Products Journal, 1998. **48**(5): p. 89-93.

112. Harper, L.T., et al., *3D geometric modelling of discontinuous fibre composites using a force-directed algorithm.* Journal of Composite Materials, 2016. **51**(17): p. 2389-2406.

113. Jin, B.C., et al., *Prediction of the Stiffness of Reused Carbon Fiber/Epoxy Composite Oriented Strand Board using Finite Element Methods*, in *SAMPE* 2016: Long Beach.

114. Shah, S.Z.H., et al., *Three Dimensional Modeling & Progressive Damage Analysis of Discontinuous Fibers Composites (DFC) Material*, in *21st International Conference on Composite Materials*. 2017: Xi'an.

115. Qian, C.C., et al., *Structural optimisation of random discontinuous fibre composites: Part 1 – Methodology.* Composites Part A: Applied Science and Manufacturing, 2015. **68**(Supplement C): p. 406-416.

116. Qian, C.C., et al., *Structural optimisation of random discontinuous fibre composites: Part 2 – Case study.* Composites Part A: Applied Science and Manufacturing, 2015. **68**(Supplement C): p. 417-424.

117. Salmi, M., *Stiffness and Failure Modeling of Discontinuous Long Fiber Composites*. 2014, Exstream Engineering.

118. Brooks, R., M.S. Johnson, and X.B. Liu. *Rediction and video tracking of damage accumulation in hybrid thermoplastic composite structures*. in *ICCM-17*. 2009. Edinburgh, UK.

119. Taketa, I., et al., *Interply hybrid composites with carbon fiber reinforced polypropylene and self-reinforced polypropylene.* Composites Part A: Applied Science and Manufacturing, 2010. **41**(8): p. 927-932.

120. Longana, M.L., et al., *Aligned discontinuous intermingled reclaimed/virgin carbon fibre composites for high performance and pseudo-ductile behaviour in interlaminated carbon-glass hybrids.* Composites Science and Technology, 2017. **143**(Supplement C): p. 13-21.

121. Landry, B. and P. Hubert. *Processing effect on the damage tolerance of randomly-oriented strands thermoplastic composites*. in *The 19th International Conference on Composite Materials*. 2013. Montreal, QC, Canada.

122. International, A., *ASTM D3039 / D3039M-14: Standard Test Method for Tensile Properties of Polymer Matrix Composite Materials*. 2014, ASTM International: West Conshohocken, PA.

123. Bogetti, T.A., J.W. Gillespie, and M.A. Lamontia, *Influence of Ply Waviness on the Stiffness and Strength Reduction on Composite Laminates.* Journal of Thermoplastic Composite Materials, 1992. **5**(4): p. 344-369.

124. Kretsis, G., *A review of the tensile, compressive, flexural and shear properties of hybrid fibre-reinforced plastics.* Composites, 1987. **18**(1): p. 13-23.

125. Feraboli, P., et al., *Defect and damage analysis of advanced discontinuous carbon/epoxy composite materials.* Composites Part A: Applied Science and Manufacturing, 2010. **41**(7): p. 888-901.

126. Lapczyk, I. and J.A. Hurtado, *Progressive damage modeling in fiber-reinforced materials.* Composites Part A: Applied Science and Manufacturing, 2007. **38**(11): p. 2333-2341.

127. Naderi, M., *Stochastic analysis of inter- and intra-laminar damage in notched PEEK laminates.* eXPRESS Polymer Letters, 2013. **7**(4): p. 383-395.

128. *21.3.2 Damage initiation for fiber-reinforced composites*, in *Abaqus/Standard v. 6.10. Abaqus Analysis User's Manual*

129. *21.3.3 Damage evolution and element removal for fiber-reinforced composites*, in *Abaqus/Standard v. 6.10. Abaqus Analysis User's Manual*

130. Halpin, J.C. and J.L. Karoos, *Strength of discontinuous reinforced composites: I. Fiber reinforced composites.* Polym. Eng. Sci., 1978. **18**(6): p. 496-504.

131. International, A., *ASTM D2344 / D2344M-16: Standard Test Method for Short-Beam Strength of Polymer Matrix Composite Materials and Their Laminates*. 2016: West Conshohocken, PA.

132. International, A., *ASTM D3846-08(2015): Standard Test Method for In-Plane Shear Strength of Reinforced Plastics*. 2015, ASTM International: West Conshohocken, PA.

133. Kant, T. and K. Swaminathan, *Estimation of transverse/interlaminar stresses in laminated composites – a selective review and survey of current developments.* Composite Structures, 2000. **49**(1): p. 65-75.

134. Mehdi Hajianmaleki, M.S.Q., in *Advances in Composite Materials - Analysis of Natural and Man-Made Materials*, D.P. Tesinova, Editor. 2011.

135. *The Behavior Of Structures Composed Of Composite Materials*, ed. R.L.S. Jack R. Vinson. Vol. 105. 2008.

136. Martiny, P., *Case Study : Effect of Residual Stresses Induced by Manufacturing Process in Discontinuous Fiber Composites (DFC) Made Part*. 2015, e-Xstream engineering.

137. Landry, B., *Experimental study and numerical simulation of defect formation during compression moulding of discontinuous long fibre carbon/PEEK composites*, in *Mechanical Engineering*. 2016, McGill University: Montreal.

138. Eguemann, N., et al. *Manufacturing and recycling of complex composite thermoplastic parts for aerospace applications*. in *SAMPE Europe 7th SETEC 12*. 2012. Lucerne, Switzerland.

139. George, P.E., K.B. Kajita, and W.B.P. Van, *Laminated composite radius filler*. 2002, Google Patents.

140. Bremmer, J., et al., *Conformal deltoid noodle for a composite structure*. 2013, Google Patents.

141. *Type H13 Hot Work Tool Steel, www.matweb.com*. Matweb LLC.

142. Victrex, *https://www.victrex.com/en/datasheets*. Victrex Plc.

143. Cotronics, *914 Glass Ceramic, http://www.cotronics.com/vo/cotr/cm_machinable.htm*. Cotronics Corp.

144. Abdalrahman, R., *Design and Analysis of Integrally-heated Tooling for Polymer Composites*. 2015, Plymouth University.

145. International, A., *ASTM D6415 / D6415M - 06a(2013) : Standard Test Method for Measuring the Curved Beam Strength of a Fiber-Reinforced Polymer-Matrix Composite*. 2013, ASTM International: West Conshohocken, PA.

146. Niu., M.C.Y., *Composite airframe structures*. 2010: Aviation Industry Press

147. Cutting, R.A., *Considerations for nondestructive evaluation of discontinuous fiber composites using dynamic analysis - Thesis*, in *Aeronautics and Astronautics*. 2015, Purdue University: West Lafayette, Indiana.

148. Feraboli, P., et al., *Notched behavior of prepreg-based discontinuous carbon fiber/epoxy systems*. Composites Part A: Applied Science and Manufacturing, 2009. **40**(3): p. 289-299.

149. Wazziki, E., N. M, A.D, and D. Leblanc, *Modelling of Compression Moulding Process Cycle Time and Application of DFMA Concept to Evaluate the Tooling Costs for Carbon Fiber Reinforced Thermoplastic Composites T-Shape Parts*, in *20th International Conference on Composite Materials*. 2015, ICCM: Copenhagen.

Appendix A

Three-point bending of a laminated beam with arbitrary layup

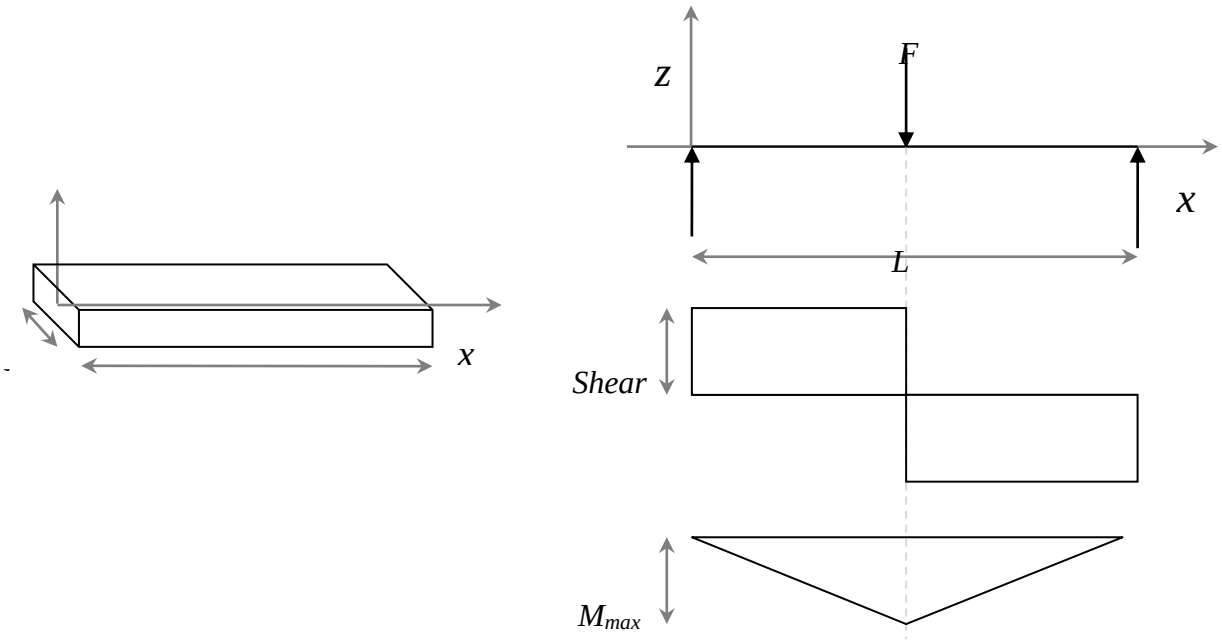

Figure A-1: Three-point bending specimen

Nomenclature:

b = width of the beam

L = span of the beam

h = height of a point within the beam in the z direction

u = displacement component in the x direction

w = displacement component in the z direction

$p_x(x)$ = axial force in the beam at a distance x from the origin

$p_z(x)$ = transverse force in the beam at a distance x from the origin

M = bending moment applied

A_{11} = extensional stiffness term of the beam laminate

B_{11} = extension-bending coupling term of the beam laminate

D_{11} = bending stiffness term of the beam laminate

Q_{11} = off-axis modulus of the lamina

σ_x = axial stress in the lamina due to the bending moment

τ_{xz} = interlaminar shear stresses in the laminate

Theoretical derivations:

Inserting displacement relations into equations of motion will result in

$$A_{11}\frac{\partial^2 u}{\partial x^2} - B_{11}\frac{\partial^3 w}{\partial x^3} + p_x(x) = 0 \qquad \text{Equation A-1}$$

$$B_{11}\frac{\partial^3 u}{\partial x^3} - D_{11}\frac{\partial^4 w}{\partial x^4} + p_z(x) = 0 \qquad \text{Equation A-2}$$

Solving these two equations for u and w will result in the following differential equations

$$\left[\frac{A_{11}D_{11}-B_{11}^2}{A_{11}}\right]\frac{\partial^4 w}{\partial x^4} = p_z(x) - \frac{B_{11}}{A_{11}}\frac{\partial p_x(x)}{\partial x} \qquad \text{Equation A-3}$$

$$\left[\frac{A_{11}D_{11}-B_{11}^2}{B_{11}}\right]\frac{\partial^3 u_0}{\partial x^3} = p_z(x) - \frac{D_{11}}{A_{11}}\frac{\partial p_x(x)}{\partial x} \qquad \text{Equation A-4}$$

Stress in the axial direction in any lamina can be found by the following

Three-point bending of a laminated beam with arbitrary layup

$$\sigma_x = Q_{11}\left(\frac{\partial u_0}{\partial x} - z\frac{\partial^2 w}{\partial x^2}\right)$$ Equation A-5

Further, the interlaminar shear stresses are given by

$$\tau_{xz} = \frac{1}{b}\int_h^z \frac{\partial \sigma_x}{\partial x}\, dz$$ Equation A-6

For a simply supported beam with a centrally placed load as shown in Figure A-1

$$\left[\frac{A_{11}D_{11} - B_{11}^2}{A_{11}}\right]\frac{\partial^2 w}{\partial x^2} = \frac{F}{2}x = M$$ Equation A-7

Using boundary conditions, $\frac{\partial w}{\partial x} = 0$ or slope = 0 at the mid point of the beam, i.e., at $x = \frac{L}{2}$

$$\left[\frac{A_{11}D_{11} - B_{11}^2}{A_{11}}\right]\frac{\partial w}{\partial x} = \frac{F}{4}x^2 - \frac{FL^2}{16}$$ Equation A-8

Similarly, using boundary conditions, $u_0 = 0$ at $x = 0$

$$\left[\frac{A_{11}D_{11} - B_{11}^2}{B_{11}}\right]\frac{\partial u_0}{\partial x} = \frac{F}{2}x$$ Equation A-9

Substituting all the above expressions into the stress equations

$$\sigma_x = \frac{Q_{11}Fx}{2(A_{11}D_{11} - B_{11}^2)}(B_{11} - zA_{11})$$ Equation A-10

$$\tau_{xz} = \frac{F}{2b(A_{11}D_{11} - B_{11}^2)}\int_h^z Q_{11}(B_{11} - zA_{11})\, dz$$ Equation A-11

Three-point bending of a laminated beam with arbitrary layup

Appendix B

Design calculations for a Flow-Control Element

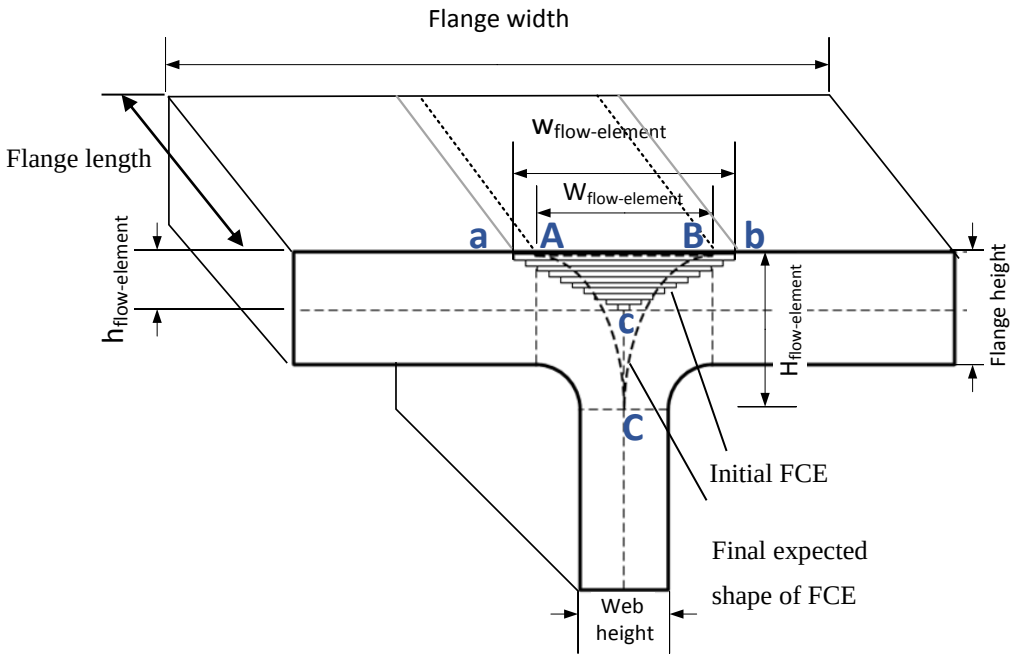

Figure B-1: Flow-control element and the calculation of the width of plies

Nomenclature

A_{FCE}	=	Final area of the flow-control element
L_{FCE}	=	Final length of flow-control element
H_{FCE}	=	Final height of the flow-control element
W_{FCE}	=	Final base width of the flow-control element
a_{FCE}	=	Initial area of the flow-control element
l_{FCE}	=	Initial length of flow-control element
h_{FCE}	=	Initial height of the flow-control element
w_{FCE}	=	Initial base width of the flow-control element
$w_{i\ ply}$	=	individual ply width of i^{th} ply in the FCE
N_{ply}	=	number of plies in the initial flow-control element
t_{ply}	=	thickness of a ply

Procedure:

- The final expected base width (W_{FCE}) of the flow-control element in the T-section is to be chosen (points A-B in Figure B-1)
- Flow-control element must promote the strand flow at least until the end of the radius on the web (point C in Figure B-1). Hence a suitable height (H_{FCE}) is chosen
- Ellipse arcs that mark out the expected final shape of the flow-control element are connected between the chosen points (arc between points A and C, arc between points B and C)
- Area of the expected final shape of the flow-control element (A_{FCE} enclosed area of points A-B-C) is calculated

- A suitable length for the flow-control element can be chosen. We recommend the length of the flow-control element (L_{FCE}) be equal to the depth of the T-section
- As length is a parameter that has been decided, we can now work with a 2D representation
- The initial triangular shape of the flow-control element is a triangular stack of plies as shown in Figure B-1
- The height of the initial flow-control element (h_{FCE}) is first determined. We recommend half the flange height for good results
- A_{FCE} obtained in step 4 is to be equal to the area of the triangle (a_{FCE}) (represented by the enclosed area of points a-b-c)
- The base width (points a-b) of the triangle is calculated from the known parameters. This is the base width (w_{FCE}) of the bottom most ply in the flow-control element
- $N_{ply} = h_{FCE}/t_{ply}$ determines the number of plies in the flow-control element, and their widths are determined such that they fit into the triangular area. The orientation of all the plies are parallel to that of the depth of the T-section
- The stack arrangement can be held together by tacking them in case of a thermoset prepreg or by manually tacking them using a heat gun at few places along the length of the element in case of thermoplastic prepregs
- An additional ply might be added to retain the flow-control element in place during compression moulding

- This flow-control element must be placed over the strands before closing the mould platens. The element controls the flow of the strands providing it a smooth transition of thicknesses and finally consolidates into the final shape of the flow-control element
- For symmetric sections, a symmetric flow-control element should be designed while for unsymmetrical sections; un-symmetric flow-control elements can be used. As the configuration shown in Figure B-1 is symmetric, this procedure is illustrated for a symmetric flow-control element design. For unsymmetrical sections, instead of considering the full area of the triangle, half the area should be considered, and corresponding ply stacks must be designed
- FCE dimensions were variable from one test configuration to another, due to the differences in the available space in the flange cavity. Nonetheless, total FCE mass was roughly constant, ranging from 1.6g to 2.0g (approximately 3% of total part mass). The FCEs were made by tacking together small UD plies with a soldering iron. A small wing was added to accurately position the FCE within the mould cavity.